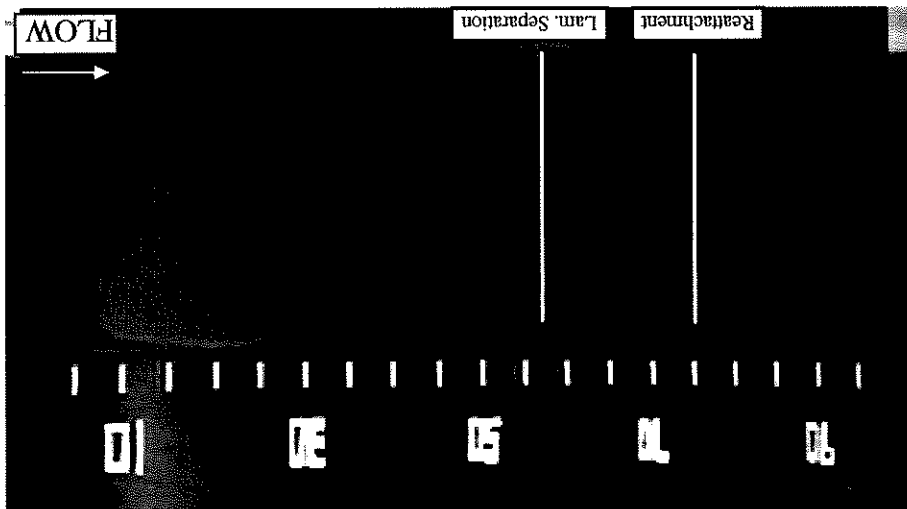


A second side topic is now explored. Computer codes often use cylinder-in-crossflow heat transfer values for the leading edge region of airfoils and turbine blades (Pointsafe and Van Rossen, 1990). An equivalent diameter for the airfoil's leading edge is first calculated and then used to calculate the heat transfer coefficient.

Figure 4.49: Evidence of Longitudinal Vortices at Reattachment

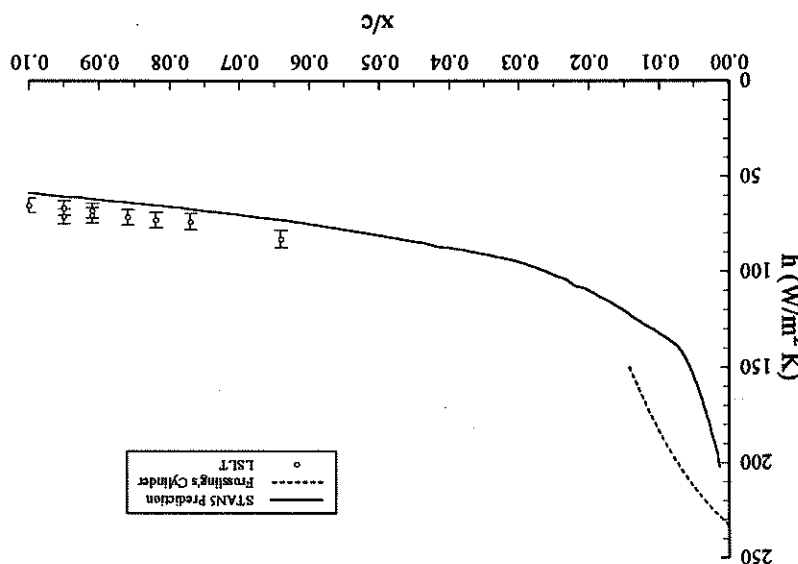


The liquid crystal color patterns created by the flow. The image shows a liquid crystal image taken during experimentation at  $\alpha = 0^\circ$  and  $Re = 750,000$ . The indications of laminar separation and flow reattachment are taken from oil flow visualization results. Notice the diamond spanwise pattern on the heater strip at the flow reattachment location. A row of spanwise vortices would produce such a pattern of alternating hot and cold spots. Note that the color pattern from 90% to 100% chord is being affected by the trailing edge aluminum spar. However, the hot and cold spots are near 75% to 85%, locations where the internal features of the model do not interfere with the liquid crystal color patterns created by the flow.

At a lower speed more relevant to the current experiments that were conducted, Jørgensen et al. detected small parallel vortices in the transition region on an A310 swept wing model with a constant chord (Jørgensen et al., 1992). Malikel and Mayle describe counterrotating streamwise vortices forming in a laminar free shear layer (Malikel and Mayle, 1996). These examples have been given because it is believed that the same phenomenon was observed during the present heat transfer experiments. Figure 4.49 shows a liquid crystal image taken during experimentation at  $\alpha = 0^\circ$  and  $Re = 750,000$ .

As can be seen, experimental values are not available at the location where the analytical cylinder solution gives results. The STAN5 prediction, however, does provide stagnation point. Poinsatte and Van Fossen found a similar over-prediction to occur for solution would over-predict experimentally determined  $h$  values as well very near the experimental values where they are available, it is assumed that the cylinder-in-crossflow prediction the STAN5 results. Since the STAN5 prediction agrees fairly well with the comparison to the cylinder solution. In general, the cylinder-in-crossflow results over-analytical cylinder solution gives results.

Figure 4.50: Comparison of Heat Transfer Results to Cylinder-in-Crossflow Predictions

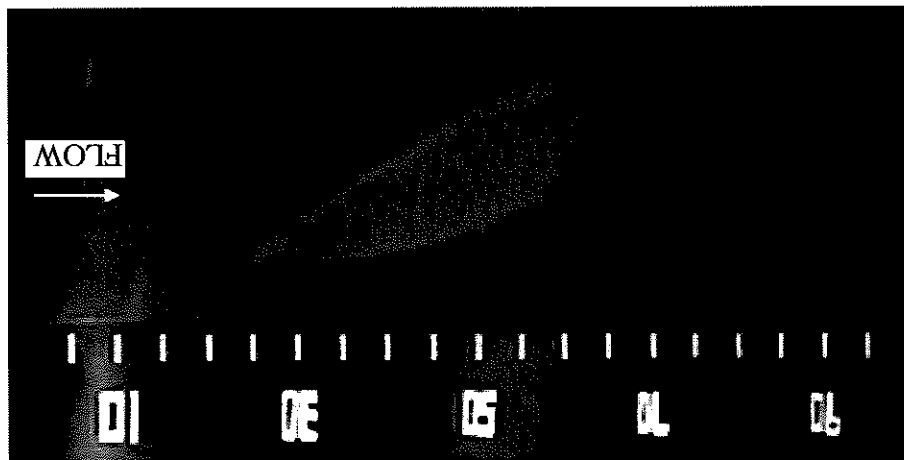


characteristics to the results of Figure 4.50.

4.50. The higher Reynolds number results are not shown because they exhibit similar chord SM701 airfoil. Results for the lower Reynolds number case are shown in Figure diameter of 0.45 inches was found by inscribing a circle in the leading edge of the 12 inch 315,000 and 750,000, such analytical calculations were made. An equivalent leading edge 1958) is used to compute the heat transfer coefficients. For the cases of  $\alpha = 0^\circ$  at  $Re =$  determined, and then Frossling's analytical cylinder-in-crossflow solution (Frossling,

A triangular color pattern has replaced the expected two-dimensional color pattern on the heater strip. The strip upper edge near the leading edge of the wing at about 5-10% chord seems to be causing a strong vertical structure that is greatly cooling the strip at a skewed angle. Referring back to Figure 4.5b of Section 4.1.3, the oil flow visualization picture hinted at this negative strip effect.

Figure 4.51: Heater Strip Negative Effect on Flow



A word of caution is now offered regarding the steady state heat transfer experiments performed. The experimenter must take great care in attaching the heater strip to the model being tested. Edges of the strip should "blend into" the model so as not to disturb the flow. Tests were conducted for the present study that included angles of attack of 15, 18, and 20° for  $Re = 315,000$ . However, no meaningful results could be obtained because the heater strip had a noticeable effect on the flow over it for those experimental conditions. This effect is seen in Figure 4.51 for  $\alpha = 18^\circ$ .

Only gives somewhat reasonable values very near the stagnation point. The cylinder-in-crossflow analytical method is in question, and the analytical method the importance of experimentally determined heat transfer data is seen. The accuracy of

## 4.2.17 Conclusions from LSLT Heat Transfer Measurements

Several conclusions may now be drawn regarding the success of the heat transfer method in revealing the various viscous flow regions on the SMT01 airfoil. It was found that the heat transfer method predicts regions of laminar and turbulent flow fairly well as a decaying trend in the  $h$  distribution. The location of the laminar separation bubble as marked by the heat transfer method was consistent with the laminar separation bubble separation (laminar separation) was not clearly marked by the heat transfer method as a distinct line. In addition, the turbulent separation location was also ambiguous when examining the heat transfer method to occur with the initially reattached boundary layer in a redeveloping state. It appears that after reattachment, the newly formed boundary layer requires a distance on the order of 5% chord to adjust to the presence of the wall and to take on the characteristics of a typical turbulent boundary layer. In this redeveloping region, the visualized heat transfer method marks the various viscous flow regions on the airfoil surface better than the heat transfer approach. The heat transfer method was of value, however, in that it verified the results of the oil flow visualization method and was shown, by comparison to numerical predictions, to provide accurate experimental airfoil heat transfer data. These data can serve as a benchmark solution for the development of better viscous flow and heat transfer prediction codes. The heat transfer method also gave insight into detailed flow structures that the oil flow visualization could not provide. These details include flow structures that the oil flow visualization could not provide. These details include flow structures that the oil flow visualization could not provide. These details include flow structures that the oil flow visualization could not provide.

The conventional oil flow visualization method is much simpler to implement than the heat transfer method and requires much less time to execute. In addition, the oil flow heat transfer method requires much less time to execute. In addition, the oil flow visualization method is much simpler to implement than the heat transfer method.

$R_{\text{heater strip}}$	heater strip resistance	0.001 $\Omega$
$L$	heater strip length	1/32 inch
$W$	heater strip width	1/32 inch
$t_{\text{wall}}$	wing wall thickness	0.015 inch
$k_{\text{wall}}$	thermal conductivity of model material	0.02 $W/mK$
$T_{\text{wall}}$	emissivity of black paint	0.02
$T_{\infty}$	free stream temperature	0.2°C
$T_2$	model internal temperature	0.2°C
$V_{\text{heater strip}}$	heater strip voltage	0.001 V ( $V < 3.25$ ) 0.010 V ( $V \geq 3.25$ )

Table 4.3: Estimates of Uncertainties in Measured Quantities

The uncertainty analysis method, estimates must be made of the uncertainties in the fundamental measurements such as length, voltage, and resistance. Table 4.3 contains the estimates used for this study.

Using this uncertainty analysis method, estimates must be made of the uncertainties in differentiating equation 4.3 of the same section.

The uncertainty terms under the radical are found in an analogous manner by examining equations 4.4 to 4.6 of Section 4.2.3.2. The partial derivative terms come from equations 4.4 to 4.6 of Section 4.2.3.2. The partial derivative terms come from the uncertainty terms under the radical are found in an analogous manner by examining

$$\frac{\partial q''}{\partial h} = \pm \left( \frac{\partial q''_{\text{TOTAL}}}{\partial h} + \frac{\partial q''_{\text{COND}}}{\partial h} + \left( \frac{\partial q''_{\text{RAD}}}{\partial h} \right)^2 + \left( \frac{\partial q''_{\text{GEN}}}{\partial h} \right)^2 + \left( \frac{\partial q''_{\text{CONV}}}{\partial h} \right)^2 \right)^{1/2} \quad (4.9)$$

An estimate of the error in the heat transfer calculations was made using the Klime and McClintock method (Klime and McClintock, 1953). Using their approach, the uncertainty in the experimental values of  $h$  can be expressed as

4.2.18 LSLT Heat Transfer Error Analysis

Uncertainty in the convective heat transfer coefficient was calculated for every  $h$ ,  $x/c$

experimental point during the execution of the data reduction program appwing, for listed

in Appendix C. The uncertainty bars are seen in Figures 4.36 to 4.44 of Section 4.2.16. It

should be mentioned that the uncertainty in the  $h$  measurements for chord locations of 82-

100% was determined differently than for the rest of the chord locations. This was

necessary since the internal array of eight thermocouples could not be positioned aft of

82% chord because of the internal geometry of the model. Specifically, the trailing edge

spur and the aft bus bar occupied that internal region of the model. Since no internal

temperature information was available in the 82-100% chord range, it was not possible to

accurately determine the conduction losses in that region.

Conduction losses in the 82-100% region were estimated as an average percent of the

total heat flux generated in that region based on the average percent conduction losses for

chord locations 0-82%. Because of this additional uncertainty in the conduction losses for

the 82-100% region, the total percent uncertainty in  $h$  in that region of the airfoil was

estimated as twice the average percent uncertainty in  $h$  values for the region 0-82%.

Therefore the error bars are larger for that region of the airfoil as seen in Figures 4.36 to

4.44 of Section 4.2.16.

Due to the large amount of data taken, it was not possible to examine all of the

uncertainty results in detail. However, the case of  $\alpha = 0^\circ$  at  $Re = 31,000$  will be briefly

mentioned.

The uncertainty in  $h$  for points located inside the laminar separation bubble (57-76%

chord) is caused mainly by the uncertainty in the conduction loss term. In this region, the

total heat flux is distributed as follows: ~65% conduction loss, ~20% radiation loss, and

~15% convection. The uncertainty in the conduction loss term is ~10%, while the

uncertainties in the radiation loss term and the total heat flux generated term are ~4% and

~1%, respectively. This large uncertainty in the conduction loss term coupled with the

fact that most of the heat generated is lost through conduction leads to large uncertainties

in  $h$  values on the order of 30%.

In regions of high convective heat transfer, however, the story is different. Examining,

for instance, the laminar flow region near the 15% chord location, the following values

Location of Error Analysis	Laminar Separation Region at 15% Chord	Wiedner Endwall Bubble	Bubble Duct	Conduction Loss	Radiation Loss	Convection Loss	Conduction %	Radiation %	Convection %	Total %	$\% u_h$
Laminar Separation Region at 15% Chord	Wiedner Endwall Bubble	Bubble Duct	Conduction Loss	Radiation Loss	Convection Loss	Conduction %	Radiation %	Convection %	Total %	$\% u_h$	
Wiedner Endwall Bubble	Bubble Duct	Conduction Loss	Radiation Loss	Convection Loss	Conduction %	Radiation %	Convection %	Total %	$\% u_h$		
Bubble Duct	Conduction Loss	Radiation Loss	Convection Loss	Conduction %	Radiation %	Convection %	Total %	$\% u_h$			
Conduction Loss	Radiation Loss	Convection Loss	Conduction %	Radiation %	Convection %	Total %	$\% u_h$				
Radiation Loss	Convection Loss	Conduction %	Radiation %	Convection %	Total %	$\% u_h$					
Convection Loss	Conduction %	Radiation %	Convection %	Total %	$\% u_h$						
Conduction %	Radiation %	Convection %	Total %	$\% u_h$							
Radiation %	Convection %	Total %	$\% u_h$								
Convection %	Total %	$\% u_h$									
Total %	$\% u_h$										

Table 4.4: Summary of Heat Transfer Uncertainty Analysis

These calculated uncertainty values are summarized in Table 4.4. Wiedner's results for endwall heat transfer in a 90° turning duct are presented for comparison (Wiedner, 1994). He also performed steady state heat transfer measurements using liquid crystal thermography.

The total heat flux generated is the sum of the laminar separation bubble, the conduction losses, the radiation loss term, and the total heat flux generated term is ~10%, ~5%, and ~1%, respectively. The percent uncertainty in the conduction loss term is of the same order of magnitude as in the region of the laminar separation bubble, but since the conduction losses are now a much smaller percent of the total heat flux generated, the uncertainty in  $h$  falls to approximately 6%.

Wiedner's results for endwall heat transfer in a 90° turning duct are presented for comparison (Wiedner, 1994). The calculated uncertainty values are summarized in Table 4.4. The uncertainty in the total heat flux generated is the sum of the laminar separation bubble, the conduction losses, the radiation loss term, and the total heat flux generated term is ~10%, ~5%, and ~1%, respectively. The percent uncertainty in the conduction loss term is of the same order of magnitude as in the region of the laminar separation bubble, but since the conduction losses are now a much smaller percent of the total heat flux generated, the uncertainty in  $h$  falls to approximately 6%.

The area of fluid dynamics involving flow instability has evolved in a different manner than other branches of the field. In particular, it has evolved "backwards" to what has been the norm. As early as 1895, Osborne Reynolds supposed that laminar velocity profiles, being solutions to the fluid dynamic equations of motion, always represent a possible type of flow but become unstable above a definite limit and change into a turbulent pattern (Schlichting, 1968). In the early years of the twentieth century, the Orr-Sommerfeld equation governing the growth of linear disturbances in a laminar boundary layer was derived. The Orr-Sommerfeld equation was simplified by examining its high-Reynolds-number (inviscid) form, known as the Rayleigh equation. In 1929, examining laminar flow over a flat plate (the Blasius profile), Tollmien adequately accounted for viscosity effects by first solving the Rayleigh equation and then using its solutions to help solve the Orr-Sommerfeld equation. Tollmien was able to calculate a neutral stability curve and from it a critical Reynolds number value for the Blasius profile at which small disturbances would first begin to grow. In 1933, Schlichting first studied the interior of the Blasius profile neutral stability curve, revealing details on the amplification of disturbances over a range of Reynolds numbers.

### 5.0.1 Fluid Instability

Now that the flow regions on the SM701 airfoil have been well established via oil flow visualization and convective heat transfer studies, work can proceed in the direction of active control of the gross separation region on the airfoil at various high angles of attack. Before success can be possible in active control of a complex flowfield, that flowfield must be well understood. This chapter, after presenting several background sections on flow instability and separation control, will discuss experiments aimed at uncovering the flow characteristics caused by the SM701 airfoil at high angle of attack. Both qualitative shear stress tests and quantitative single sensor hot-wire anemometry tests are used in this investigation. Due to the tight schedule of the LSLT and the open schedule of the ASWT, tests were performed in the latter tunnel. Tests were conducted at a Reynolds number of 315,000 unless otherwise indicated.

## 5 EXAMINATION OF POST-STALL FLOW INSTABILITIES

Linear stability theory thus allowed the prediction of dominant disturbances in laminar boundary layers. However, even in the late 1930's the prevailing view was that stability theory had little connection with boundary layer transition (Rice and Zaman, 1987). Not until Schubauer and Skramstad in 1947 revealed growing two-dimensional waves prior to transition in a flat plate boundary layer in their landmark experiment did stability theory become accepted as accurately modeling the linear processes leading to transition. (In actuality, their work was performed in 1943 but was kept confidential due to the involvement of the United States in World War II). This evolution of theory followed by experimental verification was opposite to the normal progression of experimental observation spawning a governing theory.

Many researchers have studied the two-dimensional Tollmien-Schlichting (T-S) waves that are now known to lead to transition. Experiments have been performed in which artificial T-S waves are introduced into a laminar boundary layer and are subsequently canceled by out-of-phase forcing at a downstream location. One such experiment was performed by Liepmann, Brown, and Nosenchuck who used heater strips on a flat plate (Liepmann, Brown, and Nosenchuck, 1982). The heater strips were powered by a source at certain frequencies. Partial cancellation was achieved when the downstream heater strip was driven out of phase of the upstream heater strip which was producing the original disturbance. A separated boundary layer, there exist instabilities that will amplify leading to transition to turbulence. A turbulent mixing layer will then exist which is dominated by large-scale coherent vortical structures (Brown and Roshko, 1974). These initial instabilities (termed Kelvin-Helmholtz instabilities) can be predicted with the Rayleigh equation which is the inviscid form of the more general Orr-Sommerfeld equation governing the linear stability of parallel flows.

Flow instabilities do not only appear in attached boundary layers. For a laminar separated boundary layer, there exist instabilities that will amplify leading to transition to turbulence. A turbulent mixing layer will then exist which is dominated by large-scale coherent vortical structures (Brown and Roshko, 1974). These initial instabilities (termed Kelvin-Helmholtz instabilities) can be predicted with the Rayleigh equation which is the inviscid form of the more general Orr-Sommerfeld equation governing the linear stability of parallel flows.

disturbances of different wavelengths. These initial disturbances that appear in a laminar boundary layer have been termed Tollmien-Schlichting waves in honor of these two past

Turbulent separated boundary layers also form mixing layers that contain dominant large-scale coherent vortical structures. In 1974 Wimant and Brown showed that the growth of turbulent mixing layers is controlled by a pairing of the coherent vortical structures (Wimant and Brown, 1974). It is believed today that this pairing phenomenon holds the key to actively controlling a turbulent mixing layer. The next section presents many reasons as to why it is desired to control the turbulent mixing layer, or in other words why it is desired to control flow separation.

## 5.0.2 Importance of Separation Control

The performance of air, land, and sea vehicles is dependent on their interaction with the fluid surrounding them. Separated flow regions are not usually desired and adversely influence the efficiency of the vehicle. Separation affects the performance of turbomachinery, diffusers, inlets, and other systems involving fluid flow. It is usually enhanced, and pressure recovery is improved (Gad-el-Hak and Bushnell, 1991). Separation control will lead to more efficient propellers and windmills, more efficient inlets and diffusers, increased  $C_{\text{max}}$  of airfoils, improved axial flow compressors, reduced stall control, and lower drag on automobiles, ships, and aircraft (Gad-el-Hak and Bushnell, 1991). If flow separation control can provide a 5% increase in landing  $C_{\text{L}}$ , Buttner estimates a 25% increase in payload would be realized (Buttner, 1984). Muirhead and Saltzman estimate that 50 million barrels of oil per year could be saved if flow separation control on tractor-trailer trucks would become practical (Muirhead and Saltzman, 1979).

## 5.0.3 Approaches To Separation Control

Separation occurs when the motion of fluid particles is retarded by viscous effects and adverse pressure gradient effects such that the surface streamline can no longer follow the curvature of the surface. The main goal of separation control is thus to add momentum back to the near-wall region by transferring kinetic energy from the energy-rich free stream region. Two different approaches can be taken to provide separation control:

1) **Flow Control**: Flow control is a technique that attempts to control the separation point by applying a force to the flow field. This can be done through the use of passive devices such as leading edge flaps, trailing edge flaps, and vortex generators, or through the use of active devices such as piezoelectric actuators, electrostatic actuators, and electromagnetic actuators. The goal of flow control is to delay the onset of separation and to reduce the magnitude of the separation zone.

interaction with the attached boundary layer prior to separation or interaction with the separated shear layer. Many methods have been used to interact with the boundary layer before it separates. Gad-el-Hak and Bushnell provide many valuable references on this subject (Gad-el-Hak and Bushnell, 1991). Transpiration has been used to make the boundary layer fuller, thus prolonging the attached flow region. In addition, surface heating or cooling has been used to add momentum to the near-wall region. By cooling the wall (in gas), the viscosity of the gas in the boundary layer is lowered and its density is raised; this leads to a fuller boundary layer profile (Lepmann, Brown, and Nosenchuck, 1982).

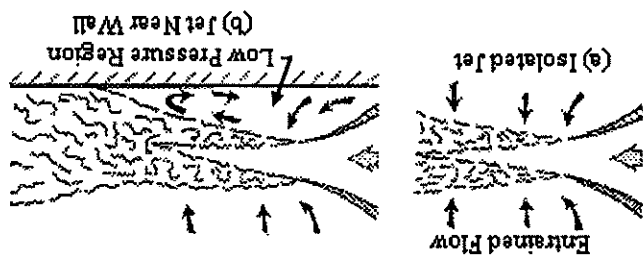
Embedded cylinders and conveyer belts have also been used to energize the boundary layer flow. Trip strips (at low  $Re$ ) and vortex generators (at high  $Re$ ) are also used to energize the boundary layer, delaying separation. A main problem with these methods of separation control is that they utilize intrusive devices that have associated drag penalties. Energy consumption, weight, volume, reliability, and cost are also factors that must be examined when looking at separation control.

The second approach that can be taken to provide separation control is enhancement of the mixing rate of the separated shear layer. Acoustic drivers, oscillating flaps and wires, dynamic blowing, and oscillatory surface heating are among the methods that have been tried to excite the instabilities of the separated shear layer. Gad-el-Hak and Bushnell emphasize that this mixing rate enhancement of the separated shear layer can provide separation control for both laminar and turbulent separating boundary layers. They report, "For initially laminar flows, the zeroth order influence of dynamic forcing is to both trip transition and enhance the eddy dynamics of the low-Reynolds-number shear layer" (Gad-el-Hak and Bushnell, 1991). They also report, "What is obvious from the initially turbulent, dynamic-input separation control research thus far is that, once again, the method works" (Gad-el-Hak and Bushnell, 1991).

Rice and Abbott offer an explanation as to why this dynamic forcing of the separated shear layer provides separation control (Rice and Abbott, 1990). They explain that by enhancing the natural instabilities of the flow through use of small aerodynamic disturbances, the growth of the large-scale coherent structures which dominate the mixing enhances the shear layer separation control (Rice and Abbott, 1990).

Figure 5.1(a) and (b): The Coanda Effect (Surface Located Near a Jet)

Source: Rice and Abbott, 1990

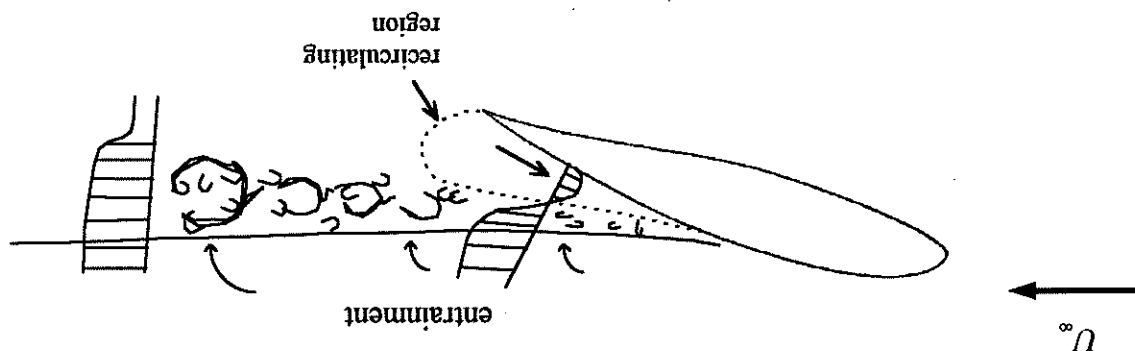


processes in the shear layer will be enhanced. This enhancement of the large-scale coherent structures can lead to flow reattachment. Rice and Abbott explain this idea using the concept of the Coanda effect. Figure 5.1a shows an isolated jet. Reattachment occurs due to the free mixing layer, and fluid is drawn in from the ambient field on both sides to replace that which has become entrained by the jet. When the jet is placed near a wall, however, the situation changes. See Figure 5.1b. When the jet is placed near a wall, static pressure develops between the wall and the jet. This resulting pressure since fluid can not be readily replaced due to the obstruction caused by the wall. A low pressure region develops between the wall and the jet. Entrainment is retarded near the wall gradient forces the jet towards the wall.

gradient forces the jet towards the wall. static pressure develops between the wall and the jet. This resulting pressure since fluid can not be readily replaced due to the obstruction caused by the wall. A low pressure region develops between the wall and the jet. Entrainment is retarded near the wall gradient forces the jet towards the wall.

Figure 5.3 summarizes the two main approaches to separation control that have just been discussed. The following section discusses past work in the active control of separated shear layers.

Figure 5.2: Airfoil Flow Separation



The idea of separation control through enhancement of the mixing rate of the separated shear layer on an airfoil can then be explained using an analogy to the jet example. Refer to Figure 5.2. By applying excitation to the separated shear layer, the natural eddy formation and pairing process can be enhanced. By creating larger and more-coherent eddies in the separated shear layer, more entrainment will occur than would be the case for the unforced separated shear layer. Due to the presence of the surface of the airfoil, low static pressure region will develop, pulling the separated shear layer towards the airfoil surface. The separated region will be reduced. It can now be seen why separation control involving dynamic forcing of the separated shear layer is viewed as a mixing enhancement problem.

Figure 5.3: Summary of the Two Main Separation Control Approaches

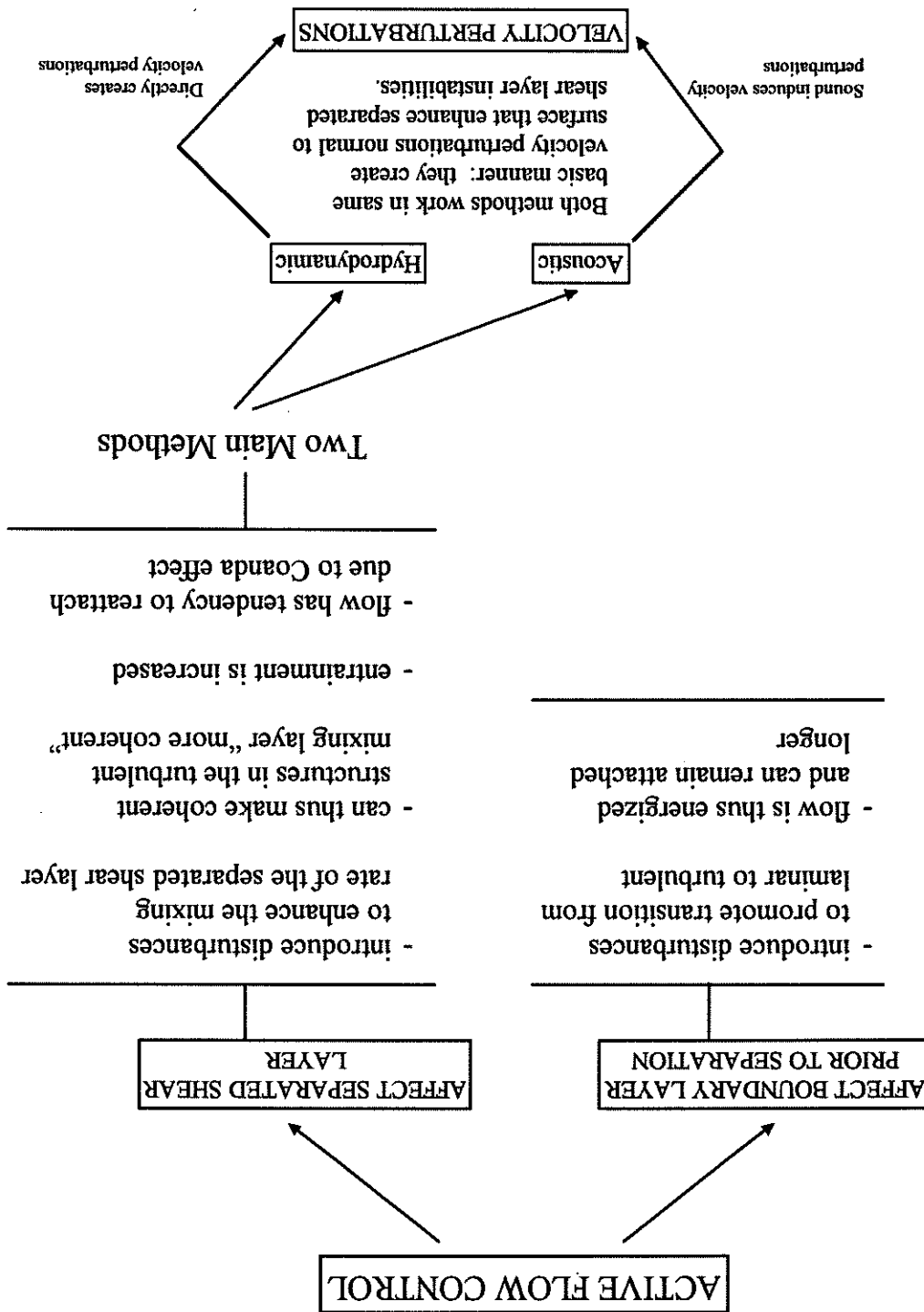
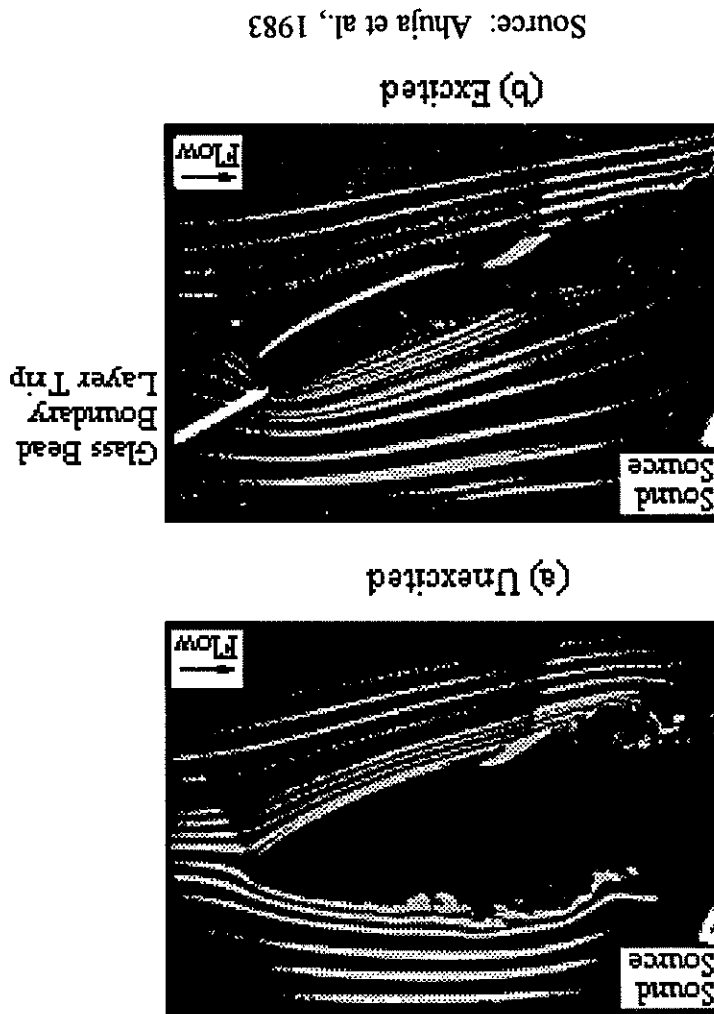


Figure 5.4: Flow Reattachment Caused by Sound



In 1983 Ahuja, Whipple, and Jones successfully demonstrated that sound at the "right" frequency and sufficient amplitude could postpone the transition to turbulence on an airfoil in both the pre-stall and post-stall regimes (Ahuja et al., 1983). An often-reproduced flow visualization photograph taken from their work is shown in Figure 5.4. Similar research was performed by Ahuja and Burtin in 1984 (Ahuja and Burtin, 1984).

This section will describe some of the past work performed in the area of active control of separated shear layers. Gad-el-Hak and Bushnell provide an extensive list of references regarding flow separation (Gad-el-Hak and Bushnell, 1991).

Similar work in control of separated shear layers has been performed in the area of active control of separated shear layers. Gad-el-Hak and Bushnell provide an extensive list of references of separated shear layers. Gad-el-Hak and Bushnell provide an extensive list of references of separated shear layers. Gad-el-Hak and Bushnell provide an extensive list of references of separated shear layers.

#### 5.0.4 Past Work in Control of Separated Shear Layers

most effective excitation frequency varied as  $U^{\frac{3}{2}}$  and was found to obey a case, tests were conducted at Reynolds numbers between 25,000 and 100,000. The McKinzie were able to reduce the laminar separation on the upper surface. For this low airfoil, while the Wortmann FX 63-137 is a leading edge stall type airfoil, Zaman and McKinzie, 1989). They studied the laminar separation at  $\alpha = 6^\circ$  for an LRN-(1)-1007 airfoil and a Wortmann FX 63-137 airfoil. The LRN-(1)-1007 is a trailing edge stall type airfoil and McKinzie, 1989). They also experimented with acoustic excitation in 1989 (Zaman and McKinzie, 1988).

Zaman and McKinzie also studied the laminar separation at  $\alpha = 6^\circ$  for an LRN-(1)-1007 caused by periodic formation and breakdown of a large separation bubble (Zaman and Zaman and McKinzie concluded that the unusually low value of 0.02 prior to stall was ( $\alpha = 18^\circ$  and  $\alpha = 20^\circ$ ), the usual "lift body" shedding value of 0.2 was measured. McKinzie in 1988 again found this low value of 0.02 prior to stall. During deep stall airfoils at high angle of attack and for lift bodies. Follow-up work by Zaman and an order of magnitude lower than most other researchers have found for tests with other wing chord,  $U_\infty$ , the free stream velocity, and  $\alpha$  the angle of attack. This value of 0.02 is with  $f_s$ , being the measured shedding frequency (dominant instability frequency),  $c$  the

$$St_{sin \alpha} = \frac{U_\infty}{f_s c} \sin \alpha \quad (5.1)$$

under the conditions at which it was tested. The modified Strohahl number is defined as precise words based on the frequency of the dominant flow instability created by the airfoil of approximately 0.02 was measured based on the airfoil "shedding frequency," or in more low Reynolds numbers tested. Just prior to stall at  $\alpha = 15^\circ$ , a modified Strohahl number test section floor. Appropriate excitation was able to eliminate laminar separation at the between 40,000 and 140,000. An acoustic driver provided sound through a hole in the (Zaman et al., 1987). They tested an LRN-(1)-1007 airfoil at Reynolds numbers varying Acoustic excitation was also used by Zaman, Bar-Sever, and Mangalam in 1987

et al., 1989). They tested a NACA 63-018 airfoil for  $6,300 < Re < 500,000$ . A sound excitation slot affected the ability of the sound to enhance a separated shear layer (Hsiao et al., 1989). Hsiao, Liu, and Shyu also examined how the location of the localized internal acoustic

effective when applied slightly before separation rather than after.

frequency equalled the shedding frequency, and it was concluded that forcing was more exciting large-scale structures in the separated shear layer. The optimum forcing though a 0.08 cm slot near the trailing edge was seen to lessen the separated region by thickness ratio was tested at a Reynolds number of 35,000 with  $\alpha = 0^\circ$ . Sound emitted on trailing edge separation (Huang et al., 1988). A symmetric airfoil with an 18% Huang, Bryant, and Maestrello also examined the effect of internal acoustic excitation airfoil and depend on the mean flow speed.

separation point. These vortices trigger large-scale circulatory motion in the wake of the surface of the airfoil is dominated by large-scale vortices shed periodically from the in stall were observed. Smoke flow visualization showed that separation over the upper Excitation was applied at 115 dB, and an increase in lift, a reduction in drag, and a delay the separated region was drastically reduced. For  $\alpha = 20^\circ$  the shedding frequency airfoil at a Reynolds number of 35,000. The angle of attack was  $20^\circ$ . At  $f_{excitation} = 2f_s$ , (dominant instability frequency) was 50 Hz, and the modified Strouhal number was 0.19. study the effect of sound on a separated shear layer (Huang et al., 1987). Sound was Maestrello, and Bryant used the technique of internal acoustic excitation to

$$\frac{U_2}{f_{excitation} V} = 10^{-5}$$
 was effective in removing laminar separation.

At NASA Lewis Research Center, Zaman and Rice studied four different airfoils at small  $\alpha$  and low Reynolds numbers. They found that acoustic excitation at about

$$St = \frac{U_2}{f_{excitation} c}$$

with

$$\frac{Re}{St} = 0.02 \text{ to } 0.03 \quad (5.2)$$

pressure level (SPL) of 95 dB was maintained, and one millimeter wide slots at 1.25%, 6.25%, and 13.75% chord were used to emit the sound. Leading edge separation for a most important control parameters. Excitation level was not as important. The best location for local acoustic excitation seemed to be slightly after the separation point. The best most effective forcing frequency corresponded to a modified Strouhal number of two, and order of magnitude higher than the shedding frequency based modified Strouhal number. Hsiao et al. reasoned that the excitation "locks-in" to the shear layer instability frequency which is approximately one order of magnitude larger than the shedding frequency. Lift number was found to agree well with Roshko's bluff body universal value of 0.17 to 0.19 (Roshko, 1954) for  $24^\circ < \alpha < 35^\circ$ . Hsiao et al. reached several conclusions regarding high  $\alpha$  post-stall separation control. They concluded that at high  $\alpha$ , the effectiveness of forcing diminishes, and flow may not become reattached when forced. However, even though the flow may not reattach, the base pressure over the upper surface would still decrease leading to an increase in lift and drag. Also, the effective range of excitation frequencies narrows for higher  $\alpha$  with the center of vortex shedding the shedding frequency. It was believed that the "enhancement of vortex shedding instability is the dominant mechanism in flow control" (Hsiao et al., 1994). Also concluded was that periodic perturbations possess the ability to synchronize the frequency of, and increase the strength of, vortices shed from the airfoil... (Hsiao et al., 1994).

Besides acoustic excitation, other methods for separation control have been examined. Bar-Sever used an oscillating 0.1 mm tungsten wire 1.5 mm upstream and parallel to an LRN-(1)-1010 airfoil to excite the laminar separation leading edge shear layer (Bar-Sever, 1989). The Reynolds number of the test was 150,000, and  $C_{l,m}$  was increased from 1.43 to 1.60 with  $\alpha_{sep}$  going from  $11^\circ$  to  $20^\circ$ .

As can be seen, much work has been done in an effort to provide separation control by dynamically forcing the separated shear layer. Both laminar and turbulent separating boundary layers have been examined. The effect of forcing location, forcing level, and forcing frequency have been studied. Among the methods of forcing that have been

### 5.0.5 Keys to Controlling the Separated Shear Layer

flow disturbances is of interest.

(as all other examples in this section are), this idea of using a piezoelectric film to create mechanism of separation control is not involved with perturbing the separated shear layer energized and remained attached longer, providing additional lift. Although this normal surface vibrations which were on average 11  $\mu\text{m}$  in amplitude. The flow was thus that this increase in  $C_{\mu}$ , was caused by the laminar flow being forced into transition by the increase in  $C_{\mu}$ , was obtained at a control frequency of 50 Hz. The researchers reported of 100,000 was studied. Leading edge stall existed under the test conditions. A 6% the upper surface covering the entire span from zero to 50% chord. A Reynolds number to provide a normal surface oscillation on a NACA 0012 airfoil. The film was attached to Kobayakawa, Kondo, and Suzuki used polyvinylidene fluoride (PVDF) piezoelectric film Cui et al. used an oscillating leading edge flap on a 2D sharp leading edge wedge (Cui become more receptive to the frequency of the forced disturbance.

27.5° and were able to increase  $C_l$  through the use of the control flap.  
et al., 1992). They tested at a Reynolds number of approximately 800,000 with a up to Cui et al. used an oscillating leading edge flap on a 2D sharp leading edge wedge (Cui seen on the instabilities in the wake. The mean velocity profile was found to adapt to airfoil's drag. For forcing frequencies outside of the receptivity range, little effect was existed for the forcing frequency in which disturbances could produce a decrease in the development of the instabilities in the wake. They found that a receptivity range on the development of the instabilities in the wake. They used linear stability analysis to examine the effect of the mean velocity profile 1989). They used linear stability analysis to examine the effect of the mean velocity profile 63A008 airfoil in a study of the flow instabilities in the wake (Gharib and Williams-Stuber, Gharib and Williams-Stuber used stainless steel heater strips on a symmetric NACA

examined include external acoustic excitation, internal acoustic excitation, vibrating wires, oscillatory flaps, and periodic blowing. Through all of this work, no clear results have yet been realized tying the enhancement of the mixing rate of separated shear layers on different bodies together. Some researchers obtain different results as to the most effective excitation frequency and forcing location. Other researchers are in agreement on those topics. It is clear that much more work must be done before active control by dynamic forcing of the separated shear layer becomes practical. The reminder of this section will describe some of the more-agreed-upon ideas involving active control of separated shear layers.

The forcing frequency is generally found to be the most important factor. Forcing at the natural shedding frequency or subharmonics of it has been found to be effective by many researchers. Ho and Huang found that the subharmonic of a vortex must amplify and not in the upstream boundary layer. This was documented by Rice and Zaman in 1987 and by Zaman and McKinzie in 1989.

Forcing location is also important. Most researchers have found the best forcing mechanism to control the separated shear layer. Zaman, Bar-Sever, and Mangalam used external acoustic excitation to affect the flow over a low Reynolds number airfoil, but they observed tunnel acoustic resonance effects. They believe that acoustic standing waves in the tunnel were inducing transverse velocity fluctuations near the airfoil. They concluded that, "alternative methods specifically inducing cross-stream velocity perturbations may be more viable in the excitation of the flows under consideration" (Zaman et al., 1987). Supporting this idea is the work of Hsiao, Liu, and Shyu. They examined the effect of the location of a slot emitting sound on the enhanced mixing rate of a separated shear layer. The location was found to be very important. They concluded that the "... nature of local excitation control is due to hydrodynamic disturbances rather than acoustics. If it were

experiments. Specifically, the flow region immediately after flow reattachment (the end of additional support for the results of the oil flow visualization and heat transfer experiments. The second objective of the qualitative shear stress measurements is to provide yet

set up a shear gauge system than it is to set up a hot-wire system.

the dominant instability frequencies (the standard practice). It is a much simpler task to simplify in that hot-wire probes would not need to be positioned in the flow to record dominant flow frequencies which exist away from the surface, future research will be discussed in Sections 5.0.3 to 5.0.5. If surface gauges can detect and measure the been believed by many researchers to be the key frequencies in active control excitation as has frequencies, associated with the coherent structures in the separated shear region, are gauges positioned downstream of separation on the airfoil's surface. These dominant dominant flow instability frequencies can be detected and measured by surface shear stress frequencies postulated during this study. The main objective is to learn whether

Two objectives exist for performing this study. The main objective is to learn whether

### 5.1.1 Objectives of Qualitative Shear Stress Experimentation

was not a goal of the current work.

gauge was used since, as will be discussed in the next section, determining flow direction gauge was used since, as will be discussed in the next section, determining flow direction Gohi (1987). Their work is described in Section 5.1.2. Only one leg of the shear stress the present experiments, a qualitative study was made following the work of Pucher and operating analogously to a conventional constant-temperature hot-wire anemometer. For only a few square millimeters and can be used to measure instantaneous wall shear stress, configuration makes the gauges directionally sensitive. Gauges typically have areas of thin metallic elements arranged in a V-configuration on a plastic film backing. This V-Mcroskey type shear stress gauges (hot film sensors). These gauges employ two similar qualitative shear stress measurements along the chord of the SMT01 airfoil using simple

### 5.1 Qualitative Shear Stress Measurements

(Hsiao et al., 1989).

length scale of the acoustic wave is much longer than the length scale of the models"

Filitte and Covert performed quantitative shear stress measurements with a gauge of their own design on a NACA 0012 airfoil (Filitte and Covert, 1992). Their gauge utilized a 10% Rhodium-90% Platinum wire instead of a film as the sensing element. The sensing wire was positioned over a 0.001 inch deep by 0.002 inch wide cavity etched into the fluctuation voltage value.

Pucher and Göhl used shear stress gauges in a qualitative manner to examine boundary layer separation on a NACA 0018 airfoil (Pucher and Göhl, 1987). Their gauges were made of 0.3  $\mu$ m nickel film vapor-deposited onto a polyimide foil. By examining the mean and rms fluctuation voltages from the gauge, Pucher and Göhl compared different flow regions on their airfoil. In their own words, "... the d-c voltage share E corresponds to the time-averaged heat transfer, whereas the a-c voltage share E describes the fluctuating part of the heat transfer" (Pucher and Göhl, 1987). In their terminology,  $e$  is the rms fluctuation voltage value.

### 5.1.2 Past Work with Shear Stress Gauges

It should be noted that the original findings regarding increasing convective heat transfer coefficient after flow reattachment was made in the LS TT; any corroborative findings here would be further substantiated since current tests are in the ASWT where the wing mounting system, free stream turbulence intensity level, and blockage effects differ from the LS TT.

Thus the qualitative shear stress method can also be interpreted as a qualitative heat transfer method.

The shear stress gauge should yield a mean voltage signal that continues to increase after flow reattachment. This increase in the mean voltage signal is predicted since the mean convective heat transfer at the surface of the wing. When the shear stress gauge is located in a region of high convective heat transfer, the electronic bridge compensates to keep the gauge at a constant temperature by increasing the voltage applied to the gauge. Thus the qualitative shear stress method can also be interpreted as a qualitative heat transfer coefficient after flow reattachment finding regarding increasing convective heat transfer method.

along with the filter and the amplifier.

channel one of the DASH-16 A/D board. Figure 5.6 shows the DISA 55M01 main unit fluctuations were amplified with a Tektronix Instrumentation amplifier and were fed into filter was then just the fluctuation component of the instantaneous signal. These removed and the signal low-pass filtered for anti-aliasing purposes. The signal out of the outputs was first sent through a Krohn-Hite model 3550 filter where the DC offset was fluctuations about the mean voltage, the instantaneous signal from one of the DISA To maximize the DASH-16 sampling resolution of the shear stress gauge voltage Metrabyte Corporation. The DASH-16 was installed in a 486 DX personal computer. were sampled with a DASH-16 A/D 12-bit data acquisition board manufactured by 15 kHz. The DISA 55M01 has two identical outputs, both of which were used. Data An overheat ratio of 1.2 was used, and the frequency response of the gauge was ten to

The fluctuating voltages can also be analyzed for frequency content.

The fluctuating voltages gives an indication of the rms value of the fluctuating shear stress. Shear stress gauge gives an indication of the mean shear stress. Likewise, the rms value of stress on the surface of the SM701 airfoil. The mean voltage value obtained from the type shear stress gauge to obtain a qualitative indication of mean and fluctuating shear Figure 5.5 is now discussed. A DISA Type 55M01 main unit was used with a McCroskey Tests were conducted in the ASWT. A schematic of the experimental setup given as

### 5.1.3 Setup for Qualitative Shear Stress Measurements

inside an artificial heart ventricle (Baldwin et al., 1987). platinum film strip covered with a 2.0  $\mu\text{m}$  thick quartz coating to study wall shear stress (Martin, 1984). Baldwin et al. used a shear stress gauge made from a 0.125 mm wide very well. Martin examined wall shear stress values in a vertical annular two-phase flow the sensor. Flittie and Covert describe the calibration procedure for shear stress gauges gauge surface to minimize conduction effects that would reduce the dynamic response of

Figure 5.6: The DISA 55M01, Krohn-Hite Filter, and Techkor Amplifier

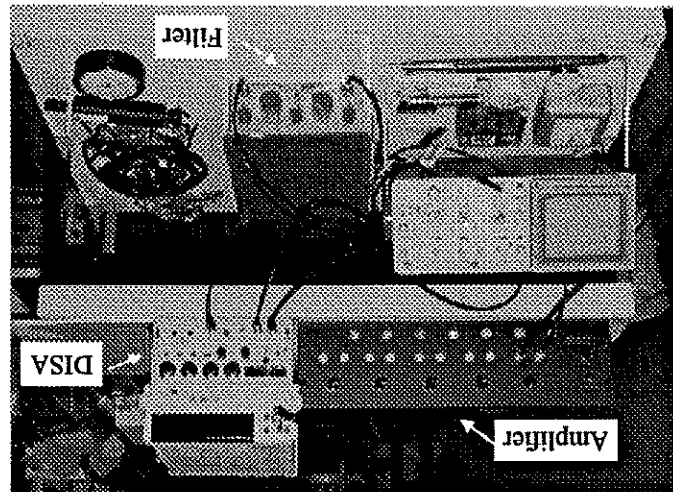
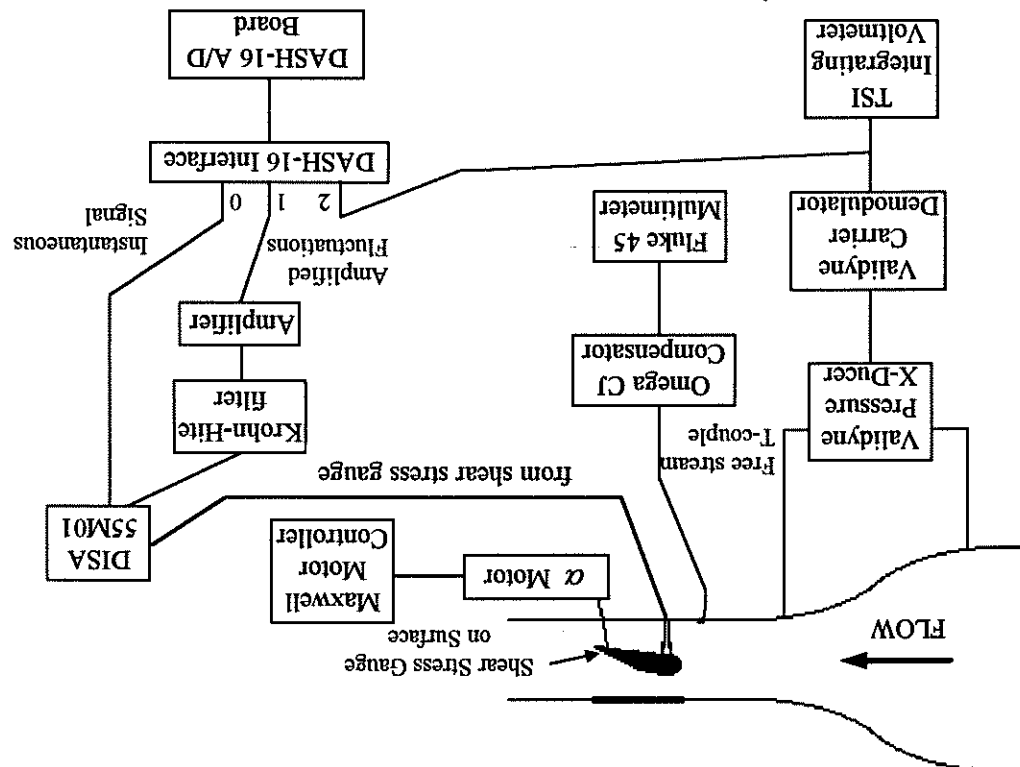


Figure 5.5: Schematic of Setup for Qualitative Shear Stress Measurements



traverse that was used in the hot-wire tests. Calibration for the qualitative shear stress tests and the omission of commands to drive the used for the quantitative hot-wire experiments in Section 5.2 by the omission of a process. The codes used for the qualitative shear stress experiments differ from those The reader is referred to that section for details on the data acquisition and data reduction codes that are described in Section 5.2.3 that were used in the hot-wire experimentation. The FORTRAN codes used for the shear stress experimentation are very similar to the

#### 5.1.4 Description of Data Acquisition and Data Reduction Codes

was described in Section 4.2.9.

A Maxwell Electronics Inc. x-y stepping motor controller was used to drive the angle of attack for a given test with the help of a Multitoyo Pro 360 digital protractor. This process of attack adjust motor. The motor controller was operated manually to set the angle of

was viewed on a Fluke 45 Dual Display multimeter.

A K-type thermocouple was attached to the tunnel wall immediately upstream of the leading edge of the model. An Omega-CJ cold junction compensation was used to electronically provide a zero °C reference point for the thermocouple. The output voltage from the thermocouple thermocouple was attached to the tunnel wall immediately upstream of the leading edge of the model. An Omega-CJ cold junction compensation was used to measure the free stream temperature. The

test section dynamic pressure could be found as described in Section 4.2.9.

The second instantaneous signal output from the DISA 55M01 was fed directly into the DASH-16 board. The instantaneous signal recorded was used to obtain a mean voltage value of the shear stress gauge output. The amplitude fluctuation voltage signal recorded through another channel at high resolution was used to obtain an rms voltage recorded in the wind tunnel contraction section. The output from the demodulator was sent to channel two of the DASH-16 board to be sampled. From this static pressure drop, the thermocouple was attached to the tunnel wall immediately upstream of the leading edge of the model CD15 Camter Demodulator was used to measure the static pressure drop across the wind tunnel contraction section. The output from the demodulator was sent to the test section dynamic pressure could be found as described in Section 4.2.9.

A Validyne differential pressure transducer (0.125 psi rating) along with a Validyne value. The second instantaneous signal output from the DISA 55M01 was fed directly into the DASH-16 board. The instantaneous signal recorded was used to obtain a mean voltage value of the shear stress gauge output. The amplitude fluctuation voltage signal recorded through another channel at high resolution was used to obtain an rms voltage recorded in the wind tunnel contraction section. The output from the demodulator was sent to channel two of the DASH-16 board to be sampled. From this static pressure drop, the

After the data acquisition was completed for a given chordwise shear stress gauge position along the chord, the tunnel was shut off, and the single gauge was moved to a new location along the chord. The procedure was then repeated for this new chordwise position, as well as subsequent chordwise locations from the leading edge to the trailing edge. Testing then progressed to the other angles of attack. The test matrix is shown in Table 5.1. Because of the moving of the gauge for each chordwise measurement location, sometimes the sensing element would crack or an attachment wire would become unsoldered. In the course of all the testing, a total of about six or eight McCroskey gauges was used due to gauge breakage.

The tunnel was brought up to achieve a Reynolds number of 315,000. The data acquisition software, described in Section 5.1.4, then directed the computer to record tests were conducted in 30 dB. Several tests were conducted with a sampling rate of 20.48 kHz, but the resulting power spectra showed no significant energy content above a few hundred Hertz; hence it was decided to reduce the sampling rate to 2048 Hz which allowed a longer sampling time and increased frequency resolution in the fluctuation spectra.

The tunnel was brought up to speed to achieve a Reynolds number of 315,000. The channel one of the DASH-16 board to be sampled as fluctuation values. Typical amplification factors were ten to 30 dB. Several tests were conducted with a sampling rate of 20.48 kHz, but the resulting power spectra showed no significant energy content above a few hundred Hertz; hence it was decided to reduce the sampling rate to 2048 Hz which allowed a longer sampling time and increased frequency resolution in the fluctuation spectra.

### 5.1.5 Procedure for Qualitative Shear Stress Measurements

voltage data continue to increase in value after the flow reattachment at the end of the qualitative shear stress results directly. In addition, both the mean and fluctuation laminar separation at the beginning of the separation bubble is not revealed by examining turbulent region than in the laminar region. As in the heat transfer study, the onset of regions very distinctly. The rms voltage value is an order of magnitude greater in the transitional region of the separation bubble. The rms voltage data also show these flow decreasing trend in the laminar flow region followed by an increasing trend in the similar trend to the convective heat transfer results presented in Section 4.2.16; a

For  $\alpha = 0^\circ$ , Figure 5.7 shows that the mean voltage parameter, as expected, follows a

Section 4.1.4.

on the graphs are the results of fluorescent oil flow visualization taken from Table 4.1 of every time the shear gauge was moved to a new chordwise location. Also presented acquired with no flow. This was done since the offset mean voltage would change slightly voltages are presented as a fractional change from the offset mean voltage,  $E_0$ , that is Both the mean and rms fluctuation voltage values are presented in the figures. The mean Figures 5.7 to 5.11 and 5.18 to 5.21 contain results of the qualitative shear stress tests.

### 5.1.6 Qualitative Shear Stress Results

$\alpha$ (deg)	Chordwise Location of Shear Stress Gauge (%)																	
5	10	15	20	25	30	35	40	45	50	55	60	65	70	75	80	85	90	95
0																		
5		X																
10	X	X	X															
15		X	X	X	X	X	X	X	X	X	X	X	X	X	X	X		
18		X	X	X	X	X	X	X	X	X	X	X	X	X	X	X		
20		X	X	X	X	X	X	X	X	X	X	X	X	X	X	X		
22		X	X	X	X	X	X	X	X	X	X	X	X	X	X	X		
25		X	X	X	X	X	X	X	X	X	X	X	X	X	X	X		

Table 5.1: Test Matrix for Qualitative Shear Stress Experimentation

Figure 5.8:  $\alpha = 5^\circ$ ,  $Re = 315,000$

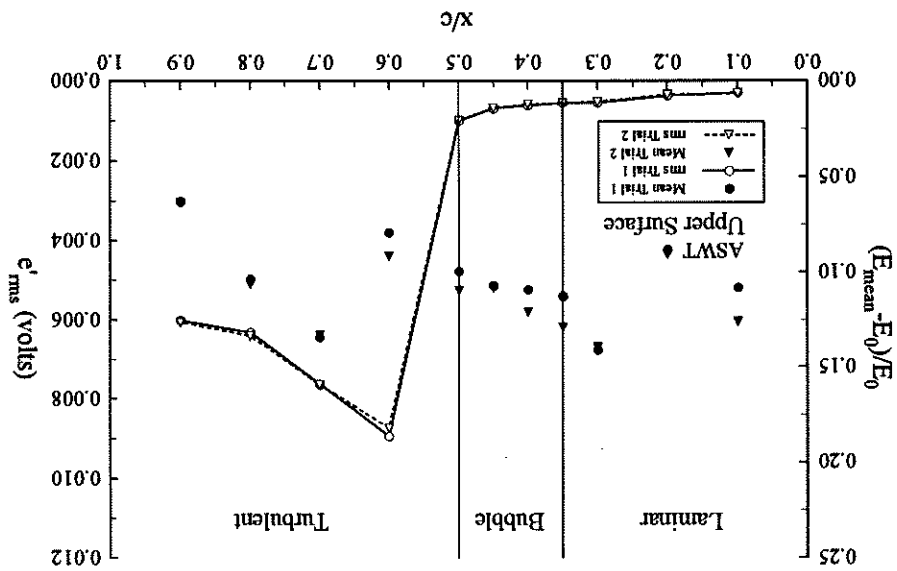
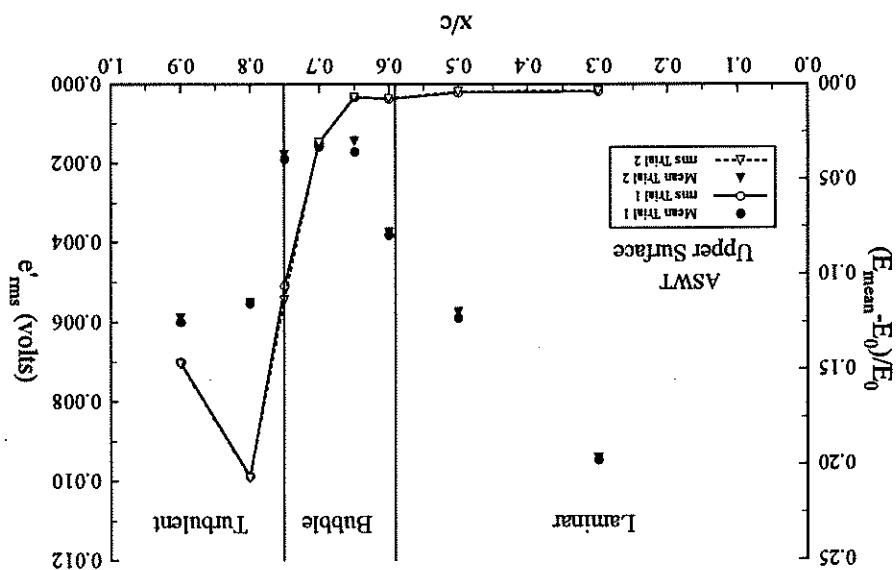


Figure 5.7:  $\alpha = 0^\circ$ ,  $Re = 315,000$



reattachment at the end of the separation bubble. Another local maximum exists very near same as for Figure 5.9. The rms data show a local maximum slightly after flow Figure 5.10 displays results for  $\alpha = 15^\circ$ . The trends in the mean voltage points are the

turbulent separation, the rms value increases slightly.

relatively constant trend throughout the turbulent region. It appears that at the location of rms data show a maximum slightly after the end of the separation bubble followed by a rms in the turbulent region with a slightly more rapid decrease in the separated region. The previously discussed for  $\alpha = 0^\circ$ . A decreasing trend is also seen in the mean voltage data

Figure 5.9 gives results for  $\alpha = 10^\circ$ . The mean voltage data follow trends as angle of attack cases.

faulty, thus yielding voltage values that do not follow the expected trends seen in the other moved forward). By the time the gauge was located at 20% chord, it may have been experiment (for this angle of attack, the gauge was first tested at 90% chord and then possible that the shear stress gauge was damaged by moving it along the chord during

The mean voltage values in the laminar region are more difficult to explain. It is thus causing poor results now during comparison to the qualitative shear stress data.

oil flow visualization photo (Figure 4.2a) was incorrectly interpreted due to its vagueness shear stress voltage patterns would make more sense. It could easily be the case that the visualization indication of the end of the bubble were shifted 5 to 10% aft, the qualitative somewhat ambiguous as to the location of the separation bubble. If the oil flow  $\alpha = 5^\circ$ . Recall that the oil flow visualization results for  $Re = 31,000$  (Figure 4.2a) were These discrepancies may be explained by reexamining the oil flow visualization results for as shown by the oil flow visualization is premature of the actual reattachment location. laminar region. When examining the rms data, it appears that the mean data in the mean voltage data in the separation bubble is greater than that of the mean data in the of the mean voltage data in the laminar region is not seen. Also, the magnitude of the For  $\alpha = 5^\circ$  the results of Figure 5.8 are rather confusing. The expected decaying trend

requires a distance to relax into a characteristic turbulent boundary layer.

transfer coefficient distributions and corroborates that the reattached boundary layer separation bubble. This is in agreement with the trend found in the convective heat

the turbulent separation location. The angle of attack for this case is very near  $\alpha_{stall}$ . The large rms maximum near turbulent separation is an indication of the eminency of stall.

Figure 5.10:  $\alpha = 15^\circ$ ,  $Re = 315,000$

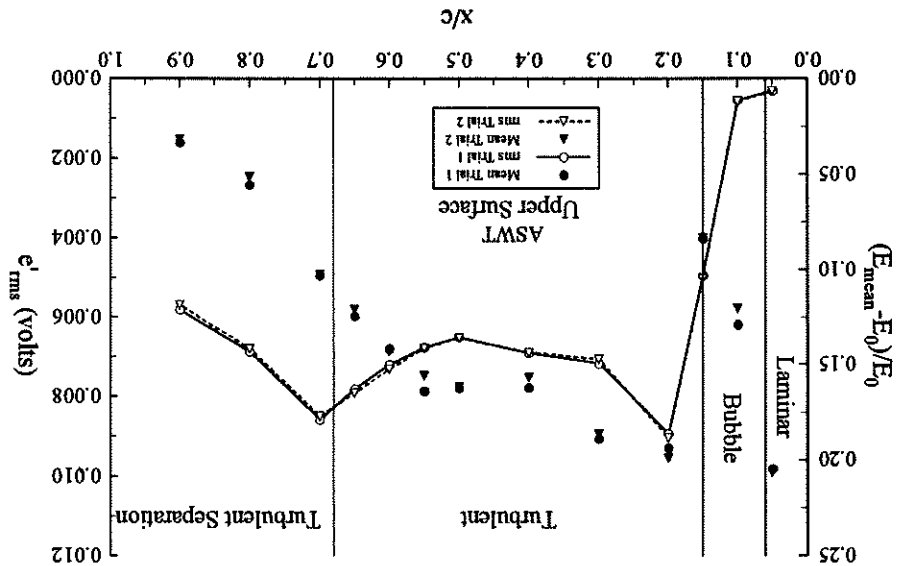
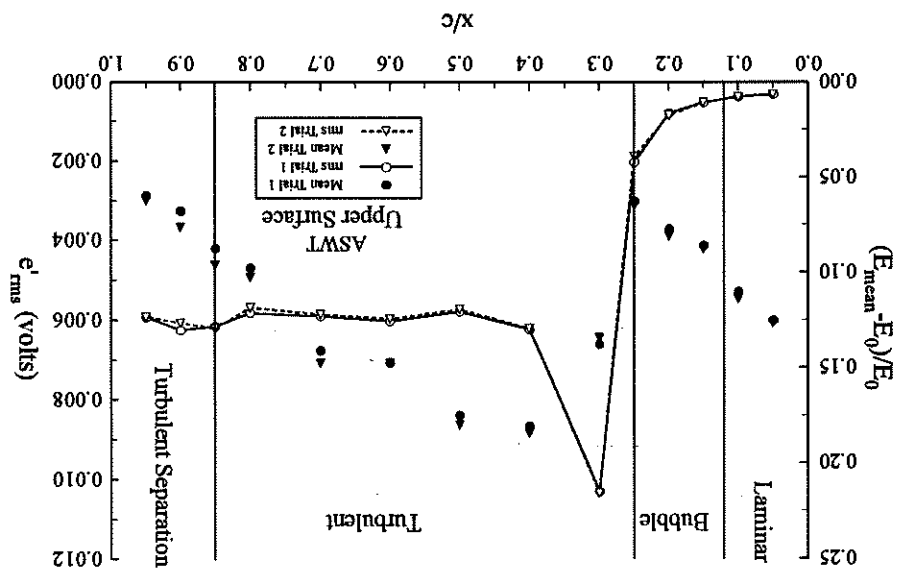


Figure 5.9:  $\alpha = 10^\circ$ ,  $Re = 315,000$



Frequency spectra were computed based on the voltage fluctuation signal for chordwise locations of 70% and 90% at  $\alpha = 15^\circ$ . No dominant spectral component surfaced. As will be seen in Section 5.2.6, hot-wire measurements for  $\alpha = 15^\circ$  also did not reveal a dominant spectral component. It appears that for  $\alpha = 15^\circ$ , which is very near the maximum of the lift curve slope of the SM701 airfoil at the Reynolds number tested, no levelling off of the mean voltage data near the turbulent separation location. This flat trend and rms voltage distributions change. See Figure 5.11. At  $\alpha = 18^\circ$ , this figure shows a rms voltage of attack is increased into the stall region of the SM701 airfoil, the mean and thus predominantly conductivity heat transfer into the wing skin material.

The rms data are also fairly constant at the turbulent separation location, increasing both upstream and downstream of separation. This rms trend differs from the rms trend at  $\alpha = 10^\circ$  and  $\alpha = 15^\circ$  (pre-stall angles) where a local maximum occurred at the turbulent separation point. As will be seen in Section 5.2.6, hot-wire measurements revealed that a distinct dominant spectral component of the flow has evolved along the airfoil at  $\alpha = 18^\circ$  and is prominent in the wake. The airfoil at  $\alpha = 18^\circ$  is creating dominant instabilities in both the upper and lower half (mean shear regions) of the wake.

The value of  $e_{rms}$  is an indication of the turbulent fluctuation level near the airfoil's surface, and the rms voltage increase near the trailing edge may be explained by examining the nature of the dominant flow instabilities being created under stalled conditions. These dominant instabilities are large coherent vortical structures that are convected downstream from the separation point on an airfoil's upper surface. Figures 5.13 and 5.14 present results of computational flowfield simulations performed on the SM701 airfoil. A fluid dynamics prediction program, FIDAP 7.50, was used to solve the time-averaged continuity and momentum equations (Uzol, 1997). A  $k - \epsilon$  turbulence model was used to grow. Figure 5.12 from Ewald et al. shows these coherent structures being shed in the turbulent free shear layers. The pairing of these structures causes the free shear layers to grow. Figure 5.12 from Ewald et al. shows these coherent structures being shed from the turbulent free shear layers. The pairing of these structures causes the free shear in the turbulent free shear layers.

The value of  $e_{rms}$  is an indication of the turbulent fluctuation level near the airfoil's

Figure 5.12: Coherent Vertical Structures in Separated Shear Layer

Source: Ewald et al., 1936

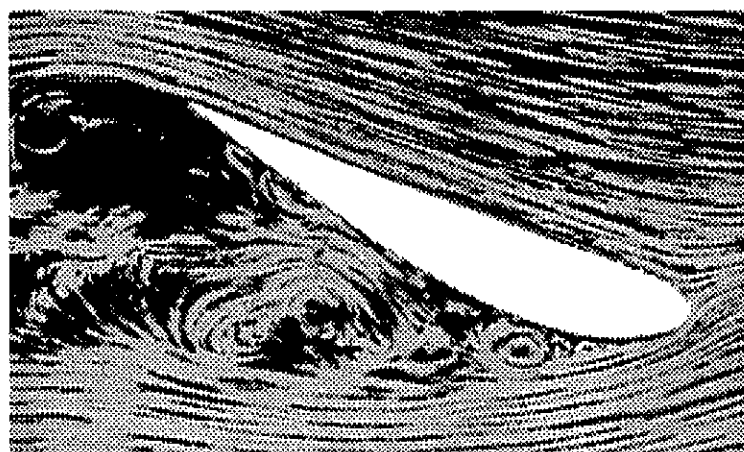


Figure 5.11:  $\alpha = 18^\circ$ ,  $Re = 315,000$

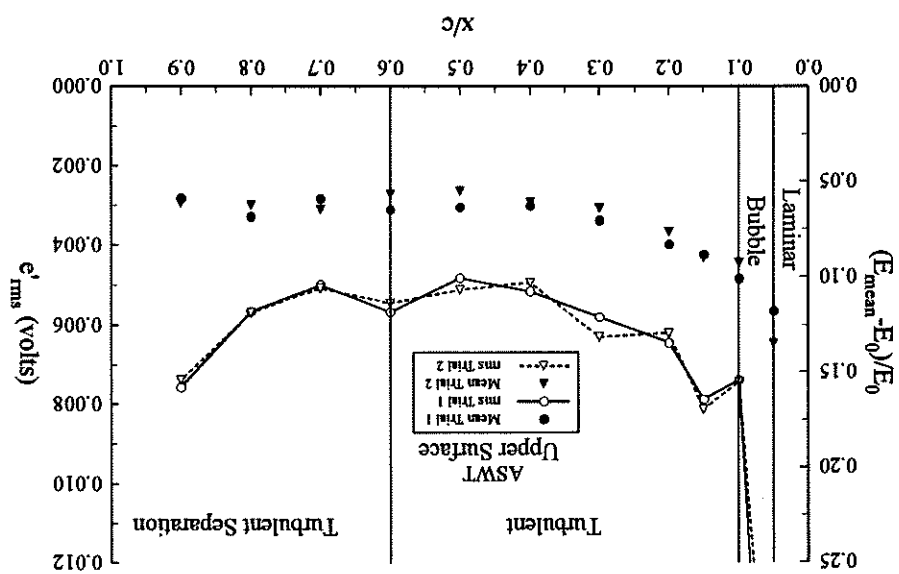


Figure 5.14: Separated Flow Region Velocity Vectors,  $\alpha = 20^\circ$ ,  $Re = 315,000$

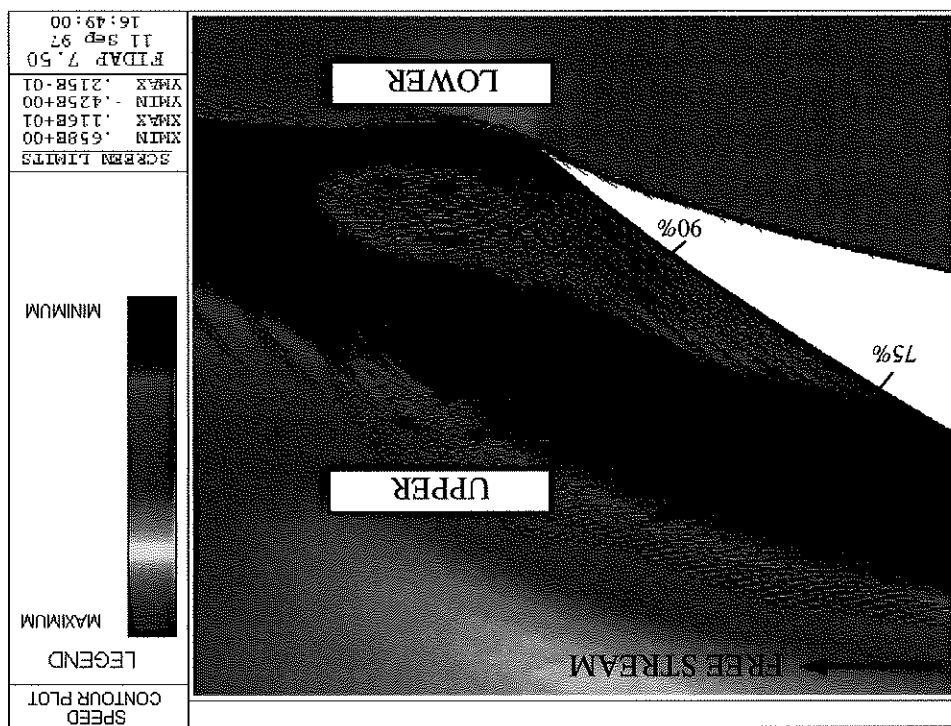
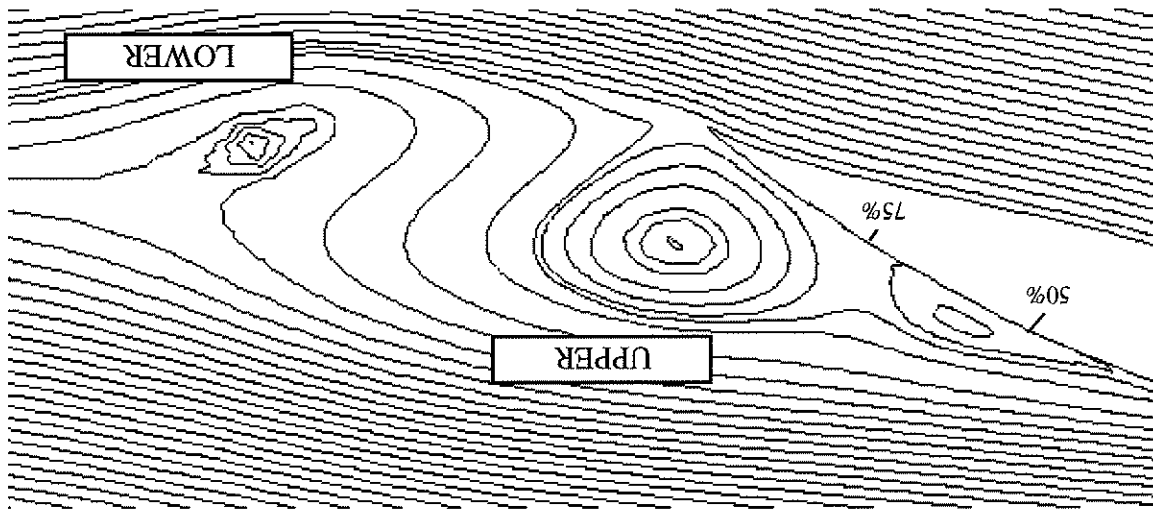


Figure 5.13: Separated Flow Region Streamlines,  $\alpha = 20^\circ$ ,  $Re = 315,000$  (from FIDAP)



utilized. A coherent structure is seen being formed near the separation point in Figure 5.13. Two other coherent vortical structures are also seen. One such flow structure is seen above the airfoil's trailing edge. The other coherent structure, which originated at the trailing edge, is seen convected downstream near the right-hand-side of the figure. In Figure 5.14, two coherent vortical structures can be seen near the trailing edge of the airfoil. The upper vortex is rotating clockwise while the lower vortex is rotating counter-clockwise. Between these two coherent vortical structures, fluid is being sent upstream towards the airfoil's trailing edge creating an "impinging jet" phenomenon on the airfoil surface. The fluid flowing upstream between these coherent vortical structures is seen by the color contours of Figure 5.14 to have a greater speed than the fluid moving to locally increased turbulence levels and heat transfer rates on the airfoil surface near the downstream side of either side of this "impinging jet" phenomenon. This greater speed leads to locally increased turbulent kinetic energy near the trailing edge is seen, an increase in turbulent kinetic energy along the airfoil's upper surface. Figure 5.15 shows the prediction of turbulent kinetic energy along the airfoil's upper trailing edge.

Figure 5.15 shows the prediction of turbulent kinetic energy along the airfoil's upper surface. As can be seen, an increase in turbulent kinetic energy near the trailing edge is predicted. Experimentation supports this prediction by revealing an increase in  $\epsilon$ , near the trailing edge when the airfoil is stalled and coherent vortical structures are being shed. Also, the convective heat transfer is enhanced at the trailing edge on the upper surface by this "impinging jet" phenomenon created by the shedding coherent vortical structures. This convective heat transfer enhancement was seen in the LSLT under stalled experimental conditions (Figures 4.42 to 4.44 of Section 4.2.16). The preliminary ASWT heat transfer conditions (Figures 4.42 to 4.44 of Section 4.2.11) also indicated this trailing edge heat transfer enhancement when the airfoil was stalled. Figure 5.16 is presented to verify this claim.

To experimentally corroborate the computational results presented in Figures 5.13 and 5.14, smoke flow visualization was performed on the SM701 airfoil at  $a = 20^\circ$ . The Reynolds number was approximately 20,000. A Lasertronics Argon ion four Watt laser was used to create a 2D light sheet by using a laser sheet fiber coupler. The laser was operated at a power level of approximately one Watt. A Rosco Omega-XT fog machine was used to provide the smoke. Figure 5.17 shows results of the smoke flow was used to provide the smoke. Figure 5.17 shows results of the smoke flow

Figure 5.16: Enhanced Trailing Edge Heat Transfer (ASWT,  $\alpha = 20^\circ$ ,  $Re = 315,000$ )

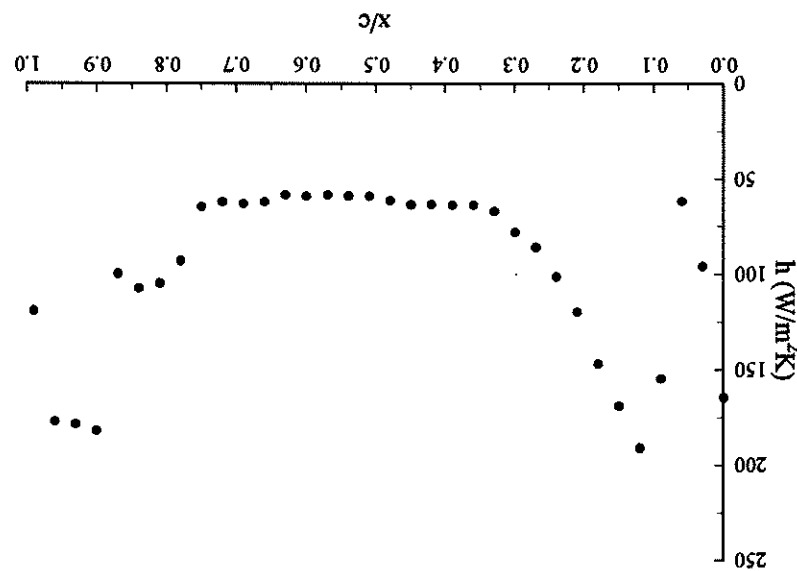


Figure 5.15: Turbulent Kinetic Energy Along Airfoil Surface,  $\alpha = 20^\circ$ ,  $Re = 315,000$

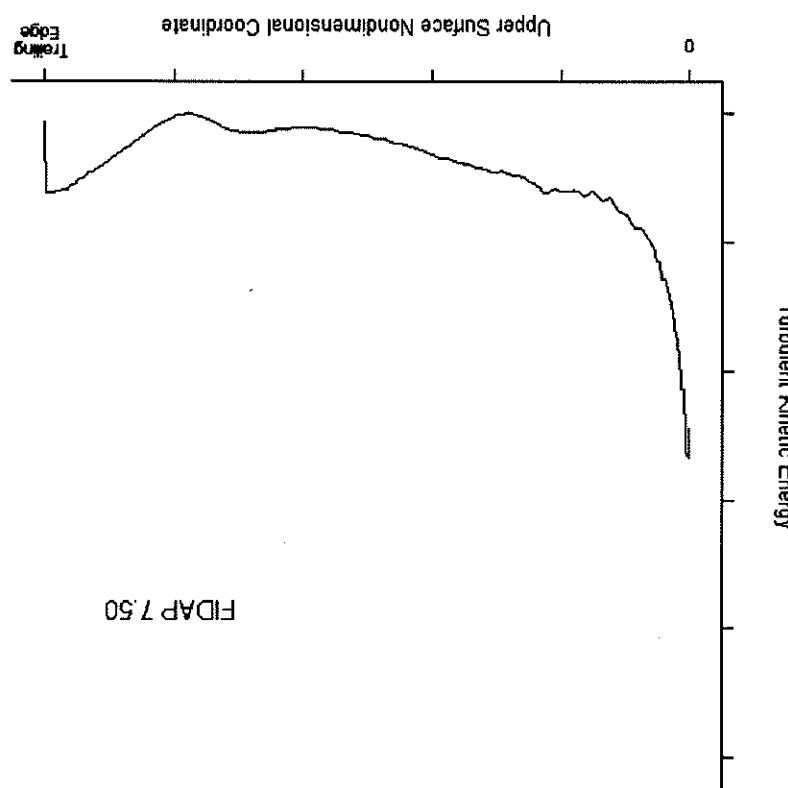
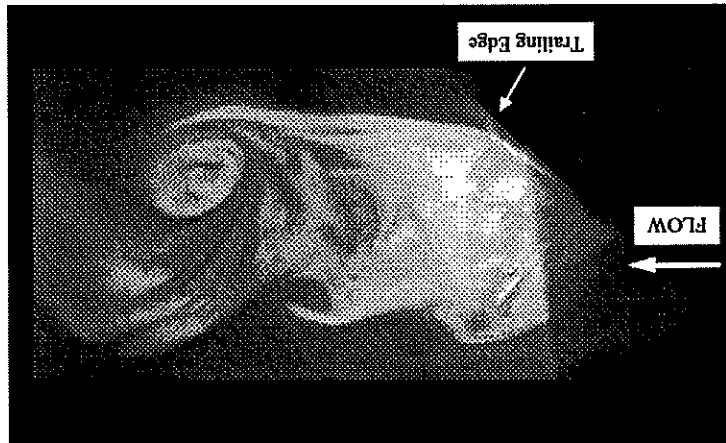
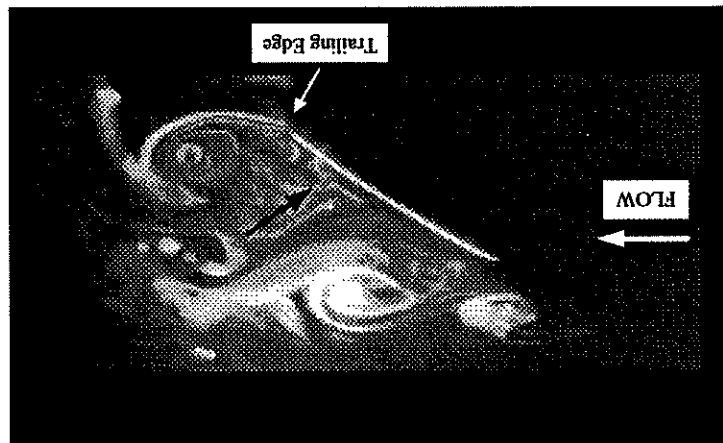


Figure 5.17: Visualization of Coherent Vortical Structures,  $\alpha = 20^\circ$ ,  $Re \equiv 20,000$

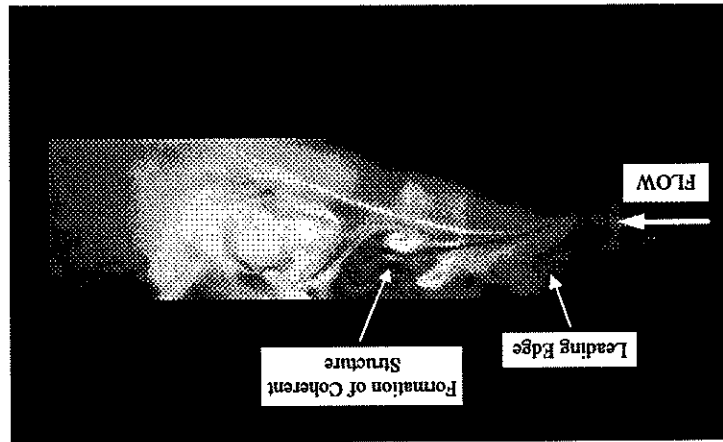
(c) Coherent Vortical Structures in Wake



(b) Coherent Vortical Structures



(a) Separation and Coherent Vortical Structure Creation



From this discussion, it is emphasized that a significant change has occurred in the flow physics from  $\alpha = 15^\circ$  to  $\alpha = 18^\circ$  and other post-stall angles of attack. Although the hot-wire experimentation reveals the existence of a dominant spectral component at  $\alpha = 18^\circ$  (as will be seen), spectra computed from the voltage fluctuation signal of the shear stress gauge at chordwise locations of 70% and 90% showed no such indication of a dominant frequency at that angle of attack.

Figures 5.18 to 5.20 were made for  $\alpha = 20^\circ$ ,  $22^\circ$ , and  $25^\circ$ , respectively. Results are similar to the  $18^\circ$  case. The mean voltage signals are fairly constant in the turbulent separated regions indicating low convective heat transfer. The rms data seem to be near a minimum at turbulent separation and increase near the trailing edge. As has been discussed, it is believed that this increase in turbulent fluctuation level near the trailing edge is caused by an "impinging jet" phenomenon created by the coherent vortical structures being shed downstream under stalled conditions.

No oil flow visualization was performed for the  $\alpha = 22^\circ$  and  $\alpha = 25^\circ$  cases since they were added to the test matrix after the oil flow visualization was performed. However, following the trends noted for  $\alpha = 18^\circ$  and  $\alpha = 20^\circ$ , the location of turbulent separation may be surmised. For Figure 5.19, at  $\alpha = 22^\circ$ , the leveling off of the mean data and minimum in the rms data occur near 20 to 25% chord; this is a good estimate of the place turbulent separation at approximately 15 to 20% chord.

Spectra of the voltage fluctuations were computed for  $\alpha = 20^\circ$ ,  $22^\circ$ , and  $25^\circ$  at various chordwise locations within the turbulent separated flow region. In no instance did the spectra reveal any dominant component corresponding to a dominant flow instability frequency. As a representative example, see Figure 5.21.

Figure 5.19:  $\alpha = 22^\circ$ ,  $Re = 315,000$

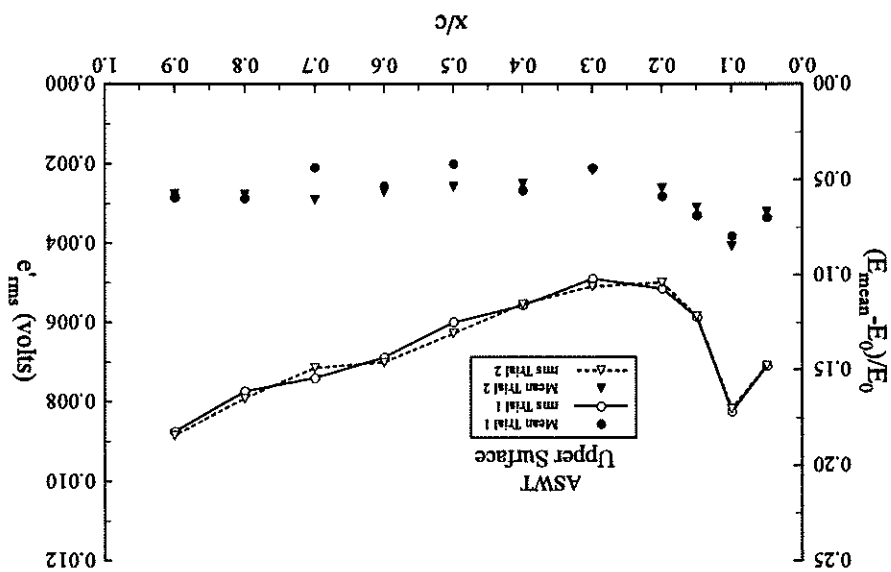


Figure 5.18:  $\alpha = 20^\circ$ ,  $Re = 315,000$

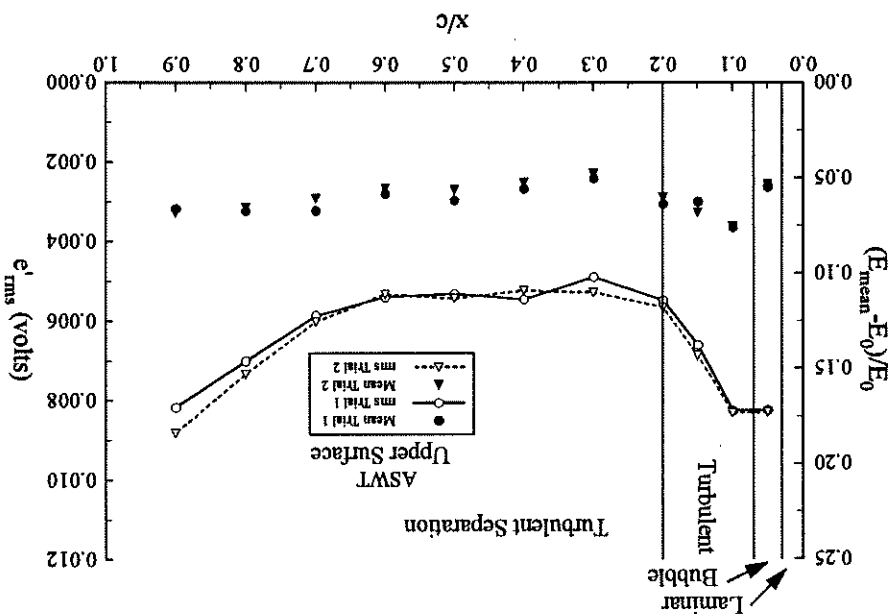


Figure 5.21:  $\alpha = 20^\circ$ ,  $x/c = 70\%$

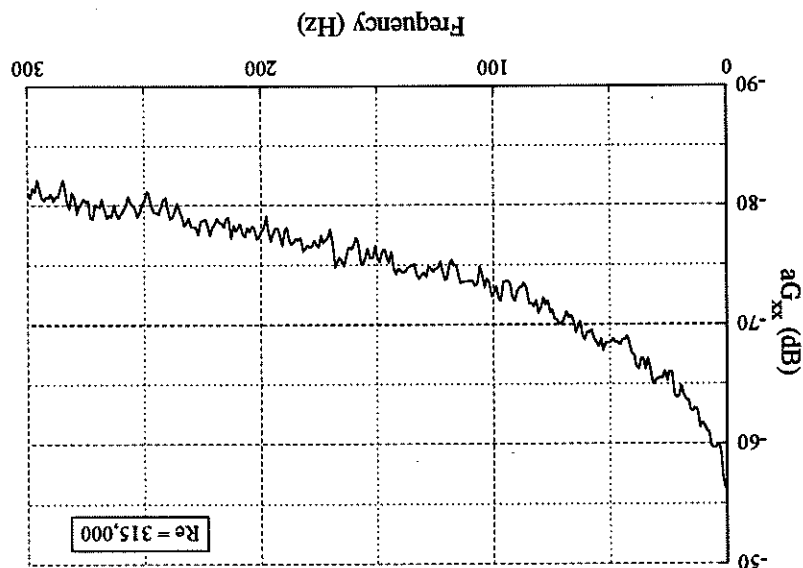
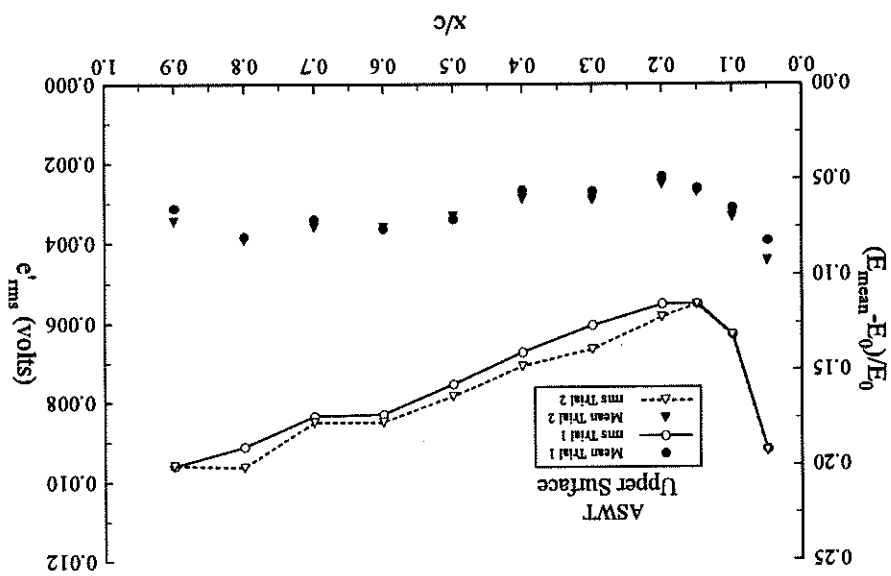


Figure 5.20:  $\alpha = 25^\circ$ ,  $Re = 315,000$



The qualitative shear stress experiments have served to verify the laminar separation bubble reattachment region trend seen with the liquid crystal thermography tests. After formed boundary layer relaxes from a mixing layer state to a turbulent boundary layer state (see Section 4.2.16 for a full explanation). The mean and rms voltage data were found to follow this same increasing trend after flow reattachment. This trend in the shear stress gauge voltage output, it should be noted, was seen in a facility (ASWT) different than that in which the heat transfer tests were conducted (LSLT). This phenomenon thus was not caused somehow by the LSLT wind tunnel. The ASWT has a higher free stream turbulence intensity, a smaller cross-section leading to increased blockage effects, and a different model mounting scheme than the LSLT in which the heat transfer tests and laminar separation regions or between turbulent and turbulent separation regions.

The rms voltage data were found to vary by an order of magnitude in the laminar and turbulent regions. However, no obvious distinction in rms voltage occurs between laminar and laminar separation regions or between turbulent and turbulent separation regions.

The chordwise trends in both the mean and the rms voltage data radically change when the airfoil angle of attack enters the stalled regime. The mean voltages are nearly constant in the turbulent separation regions indicating low convective heat transfer and predominantly conduction heat transfer into the airfoil substrate. The rms voltage data are near minimum at turbulent separation, with an increasing trend throughout the separation region. It is believed that this increasing trend in  $\text{e}^{\text{ms}}$  towards the trailing edge is tied to the generation of large scale coherent vortical structures that appear after the airfoil is stalled.

The qualitative shear stress tests proved a failure in revealing any dominant spectral components of the flow instabilities (shedding frequencies) at high angle of attack. Either no dominant flow instabilities exist at the conditions at which tests were conducted, or the dominant instabilities only exist in a confined region away from the airfoil surface.

Hot-wire tests will prove the latter case to be true.

### 5.1.7 Conclusions from Qualitative Shear Stress Measurements

angle of attack could be adjusted in the circular cross-section ASWT. Angles of attack transfer measurements. A gap of about  $\frac{1}{8}$  inch had to be left at both wing tips so that the two-dimensional. The model was mounted as described in Section 4.2.9 for the heat making foam wing tip extensions. The model tested for the hot-wire experiments was thus model that was used in the ASWT heat transfer experiments was modified slightly by Tests were conducted in the ASWT at  $Re = 315,000$ . The finite aspect ratio 2.58

### 5.2.2 Experimental Setup for Hot-Wire Flowfield Measurements

where experimentation is easier. airfoil. If both locations yield similar results, then future testing can be done in the wake perform a wake traverse than it is to perform a profile traverse normal to the chord of an found in the wake that are found in the profiles on the airfoil itself. It is much easier to wake positions are examined with the hope that similar shedding frequency results will be the development of the shedding vortices and subsequent pairing and strengthening. The longitudinal wake positions. By examining several chordwise stations, it is hoped to track subject traversing measurements are made at various chordwise stations as well as at two determine the best location at which to measure the shedding frequency; to explore this escaped the shear stress gauges discussed in Section 5.1. A second objective is to that frequency scales with the experimental conditions. This shedding frequency has (shedding) frequency created by the airfoil at high angle of attack and to determine how flowfield. The first objective is to experimentally measure the dominant instability several objectives are laid out for a hot-wire anemometry study of the SM701 airfoil 5.2.1 Objectives of Hot-Wire Flowfield Experimentation

Because of the failure of the qualitative shear stress tests to provide dominant flow wake surveys were conducted and analyzed for dominant frequency content under different sets of experimental conditions.

section describes experiments in which velocity profiles along the chord of the airfoil and instability information, efforts were turned to hot-wire anemometry experimentation. This 5.2 Hot-Wire Flowfield Measurements

studied included  $15^\circ$ ,  $18^\circ$ ,  $20^\circ$ ,  $22^\circ$ , and  $25^\circ$ . In order to seal the  $\frac{1}{2}$  inch gaps between the wing tips and the rounded tunnel walls, foam weather stripping was attached to the wing tips. A schematic of the experimental setup is given as Figure 5.22 and will now be discussed.

A DISA Type 55M01 single sensor hot-wire system was used to measure mean and fluctuating velocities in the flowfield. The DISA 55M01 has two identical outputs, both before being sampled by the DASH-16 board. The filter was a Krohn-Hite model 3550 personal computer. To maximize the resolution of the measured velocity fluctuations, the instantaneous voltage signal from one of the DISA outputs was filtered and amplified before being sampled by the DASH-16 board. The DASH-16 was installed in a 486 DX board manufactured by Metabyte Corporation. The DASH-16 12-bit data acquisition board was used. Data were sampled with a DASH-16 A/D 12-bit data acquisition card which were used. A schematic of the experimental setup is given as Figure 5.22 and will now be discussed.

#### DASH-16 A/D board.

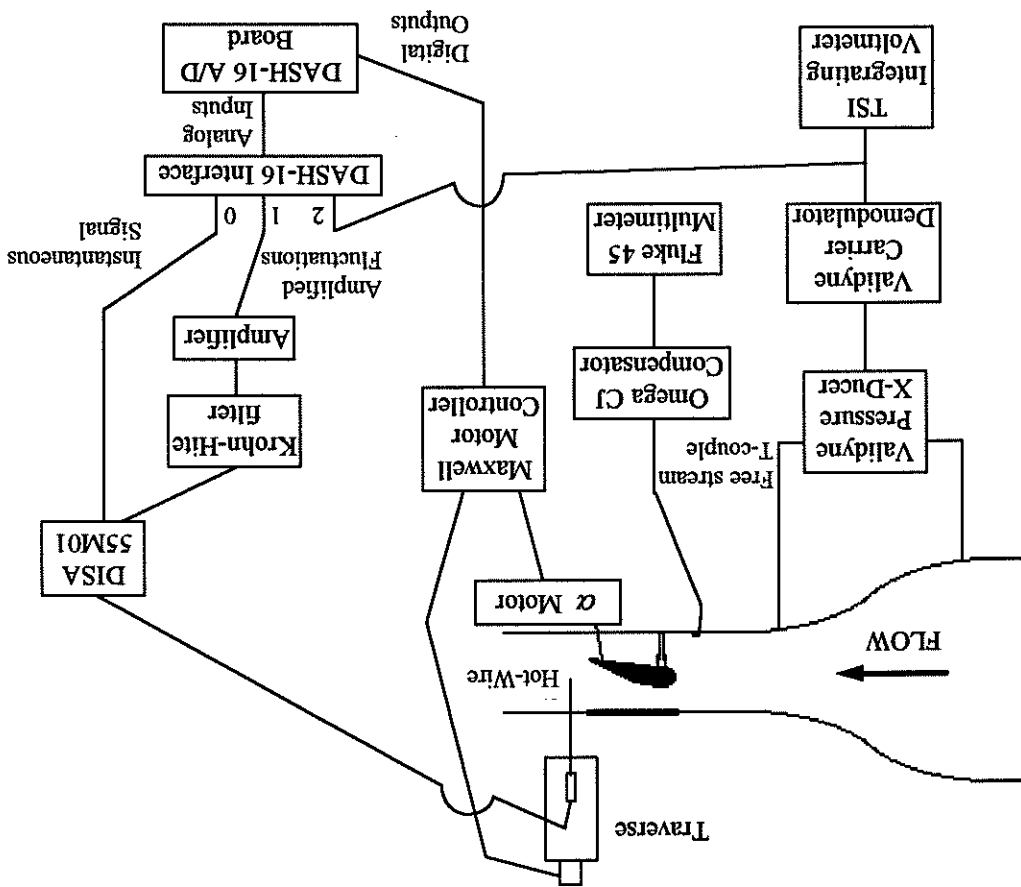
A DISA Type 55M01 single sensor hot-wire system was used to measure mean and fluctuating velocities in the flowfield. The DISA 55M01 has two identical outputs, both before being sampled by the DASH-16 board. The filter was a Krohn-Hite model 3550 personal computer. To maximize the resolution of the measured velocity fluctuations, the instantaneous voltage signal from one of the DISA outputs was filtered and amplified before being sampled by the DASH-16 board. The filter was a Krohn-Hite model 3550 that was used to remove the DC voltage offset of the instantaneous hot-wire signal and to low pass the hot-wire signal for anti-aliasing purposes. The signal out of the filter was then just the fluctuation component of the instantaneous signal. These fluctuations were amplified with a Techkor Instrumentation Amplifier and fed into channel one of the DASH-16 A/D board.

The test section dynamic pressure and free stream temperature were measured as is discussed in Section 5.1.3 for the qualitative shear stress tests. A Maxwell Electronics Inc. x-y stepping motor controller was used to drive the motor of a UniSlide Electronics well as the angle of attack adjustment motor. The unidirectional traverse has a 14 inch UniSlide traverse as well as the angle of attack adjustment motor. The UniSlide traverse is manually to set the angle of attack for a given test with the help of a Multitoyo Pro 360 range of motion and was made by Velmex, Inc. The angle of attack motor was operated well as the angle of attack adjustment motor. The UniSlide traverse has a 14 inch UniSlide traverse as well as the angle of attack adjustment motor. The UniSlide traverse is manually to set the angle of attack for a given test with the help of a Multitoyo Pro 360 range of motion and was made by Velmex, Inc.

The second instantaneous signal output from the DISA 55M01 was fed directly into channel zero of the DASH-16 board. Channel zero was then used to obtain mean voltage values from the hot-wire output while channel one was used to obtain amplitude fluctuations values at a high resolution. The instantaneous signal was found by adding the mean and fluctuation values.

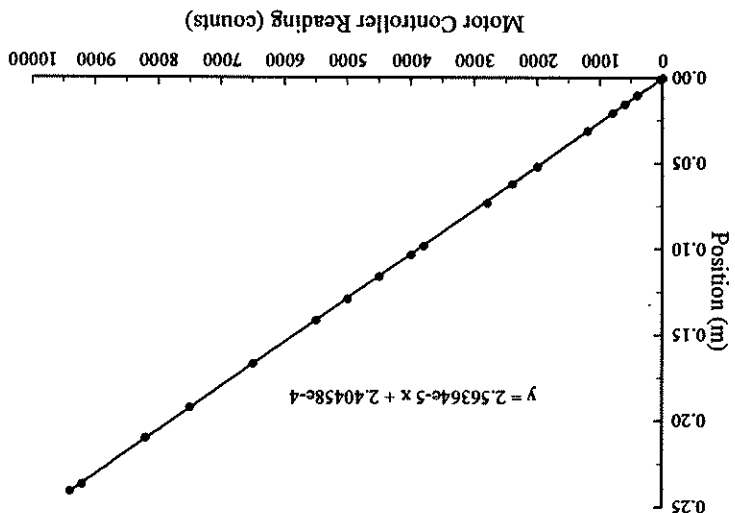
The test section dynamic pressure and free stream temperature were measured as is discussed in Section 5.1.3 for the qualitative shear stress tests. A Maxwell Electronics Inc. x-y stepping motor controller was used to drive the motor of a UniSlide Electronics well as the angle of attack adjustment motor. The UniSlide traverse has a 14 inch UniSlide traverse as well as the angle of attack adjustment motor. The UniSlide traverse is manually to set the angle of attack for a given test with the help of a Multitoyo Pro 360 range of motion and was made by Velmex, Inc.

Figure 5.22: Schematic of Setup for Flowfield Measurements



Before tests could begin, the hot-wire had to first be calibrated. An overheat ratio of 1.8 was used for the hot-wire. The frequency response of the hot-wire was typically 35 to 40 KHz. A pitot-static probe provided the reference velocity against which the hot-wire output voltage was calibrated. A Validyne Demodulator was used to record the pitot-static probe's measured pressure difference (the dynamic pressure). A small laminar air jet was used for the calibration. Figure 5.24 shows the hot-wire sensor positioned near the pitot-static probe at the jet outlet. Care was taken to keep the hot-wire sensor at least one pitot-static probe at the jet outlet. Figure 5.24 shows the hot-wire sensor positioned near the pitot-static probe at the jet outlet. Care was taken to keep the hot-wire sensor at least one pitot-static probe at the jet outlet.

Figure 5.23: Traverse Calibration

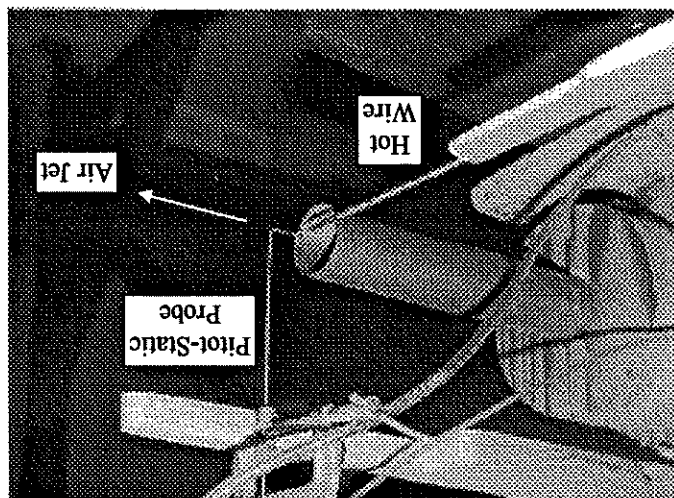


shown in Figure 5.23.

The traverse motor, on the other hand, was computer-controlled. The DASH-16 digital outputs were used to send  $\pm 5V$  pulses to the Maxwell stepping motor controller which in turn stepped the traversing motor one step for each pulse received. Using this control method, very accurate positioning of the hot-wire sensor could be achieved. The traverse was calibrated, and it was found that each step moved the hot-wire sensor  $2.56 \times 10^{-5}$  meters. The calibration is shown in Figure 5.23.

A fourth-order polynomial curve was fit through the velocity versus volts data of the hot-wire calibration. The calibration was repeated every day that tests were conducted due to ambient temperature changes. Calibration results are shown in Figure 5.25. Notice that the calibration curves agree well. Some of the calibration curves from other test days did not agree as well with the curves shown in Figure 5.25; hence, it is important to calibrate each day that tests will be performed.

Figure 5.24: Calibration of Hot-Wire Anemist Pitot-Static Probe



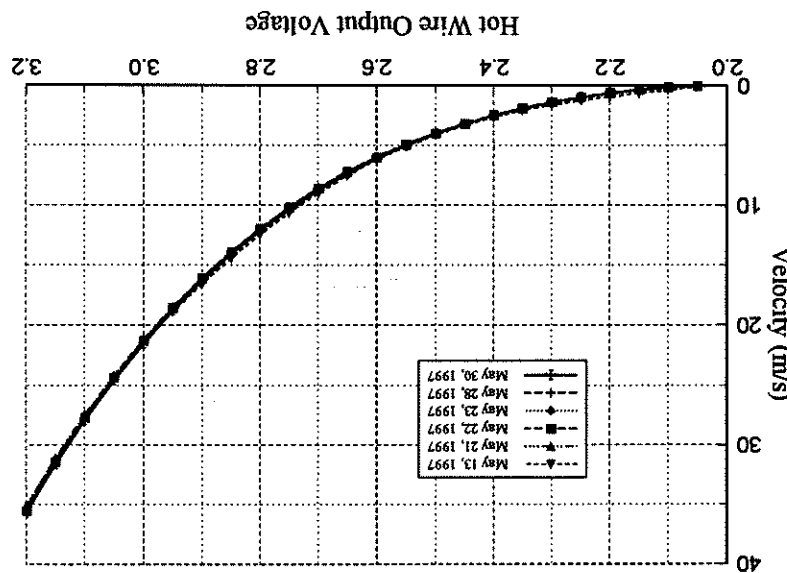
probe diameter from the pitot-static probe, thus limiting interference effects that may occur between the two velocity measuring devices.

Because of the need to run a commercially available code to stream the hot-wire data to the computer, other codes written to operate the experimental system had to be run through use of a batch file. A sample batch file (sample.bat) is given in Appendix D, followed by listings of the original codes to be discussed. This simple example batch file first executes a code named zeroes.exe. This code instructs the DASH-16 to read the initial offset voltage values from the instruments. Ambient conditions are inputted by the user.

The programs that allowed real-time data from the hot-wire to be streamed to the computer for storage. These programs, named mkfile, streamer, and unpack, were developed by Metrabyte Corporation. The only codes not written for this research were the programs that will briefly describe these codes. The only codes not written for this research were sections that allow real-time data from the hot-wire to be streamed to the computer for storage. These programs, named mkfile, streamer, and unpack, were developed by Metrabyte Corporation. The only codes not written for this research were the programs that allow real-time data from the hot-wire to be streamed to the computer for storage. These programs, named mkfile, streamer, and unpack, were developed by Metrabyte Corporation.

### 5.2.3 Description of Data Acquisition and Data Reduction Codes

Figure 5.25: Hot-Wire Calibration Polynomial and Its Repeatability



The batch file then calls another batch file named hotwire.bat, listed in Appendix D after the main batch file sample.bat. The name after the "call hotwire" command is the name which will be used for the output files when data are taken at a given traverse location. The number after this name is the desired number of traverse steps that will be taken after data are recorded for the present traverse location.

Hotwire.bat first executes a code named waitgain.exe. This very simple code merely causes a delay that allows the wind tunnel to be brought up to speed and the hot-wire fluctuation signal can be amplified to best fill the DASH-16 A/D voltage range. Next, the amplification gain to be set for the fluctuation signal. By setting the gain here, the hot-wire.bat executes mklfile, a Metrabyte Corporation code that creates a data file into which hot-wire data will be streamed. The data file is created on a virtual disk in the computer's RAM. For this example, the data file is named hwdata.bin. Next, a DOS application, speeddisk, is run to ensure that the region into which data are to be streamed is contiguous. This is a requirement of the streamer code.

Streamer.exe is then run. This causes the DASH-16 to sample channels zero and one and write the data to the virtual disk into the file hwdata.bin. Sampling rate and channel information are contained in a batch file named stream.bat.

After the hot-wire data have been collected, hotwire.bat runs a code named pithot.exe. This code directs the DASH-16 to sample the contraction pressure transducer voltage and inputs from the user the thermocouple reading and the amplifier gain setting. A code to drive the hot-wire traverse is then executed (trav100.exe), moving the probe the desired number of steps as set in the main batch file sample.bat. The binary hwdata.bin file is then converted to an ascii file through use of a Metrabyte Corporation sample.bat. The user can simply repeatedly call hotwire.bat, specifying a new output file name and number of traverse steps for each line. The final time hot-wire main batch file sample.bat. The user can simply repeatedly call hotwire.bat, specifying a sampling is desired, the line in the main batch file should be "call hotlast" instead of "call hotwire."

At this point hotwire.bat is finished executing. The program control returns to the program, unpack.exe.

a jet of air and the hot-wire sensor as shown in Figure 5.26. Separate tests were performed. The first test involved putting a simple propeller between the jet of air and the hot-wire sensor as shown in Figure 5.26. It was decided that before beginning experimentation on the SM701 airfoil, the setup should first be verified as to be working properly. To accomplish this verification, three separate tests were performed.

#### 5.2.4 Verification of Experimental Setup

.fft → contains power spectrum information

.dat → contains single column of instantaneous fluctuation velocity values

.log → contains summary information about streamer execution

frequency, hot-wire position, and mean and rms hot-wire velocities

.doc → contains hot-wire summary information such as sampling

streaming

.raw → contains raw counts for channels zero and one from hot-wire

For each traverse position at which data were recorded, these files exist.

including  $Re$ ,  $Ma$ ,  $p$ ,  $U_\infty$ ,  $T_\infty$ , and  $\mu$ .

.out → single file containing reduced data values for every traverse position

traverse position

.con → single file containing raw test condition voltage data for every

the following files exist.

raw data and generating meaningful output data. After this data reduction code executes, After taking data using the main batch file, the code hwreduce.exe is run to reduce the raw data and generate meaningful output data.

The rotation rate of the propeller was recorded with an AMETEK Model 1726 Digital Tachometer. The hot-wire signal was recorded and then analyzed for frequency content using a FORTRAN FFT subroutine. The FORTRAN subroutine was taken from a numerical recipes book (Press et al., 1992). For several speeds of air flow and several propeller rotation rates, the frequency domain results consistently showed a distinct energy content peak at a frequency corresponding to the measured propeller rotation frequency.

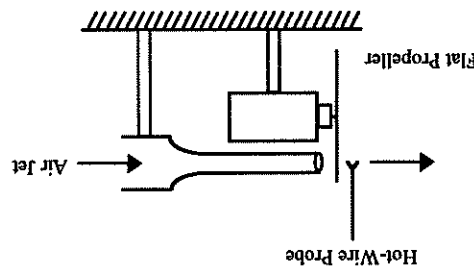
The second verification test involved a 4.5 inch diameter circular cylinder mounted in the ASWT test section with the axis of the cylinder perpendicular to the flow direction. The hot-wire system was used to record the unsteady velocity field in the wake of the cylinder. From the velocity fluctuation measurements, the shedding frequency was obtained using the FORTRAN FFT subroutine. Based on the free stream velocity, a Strouhal number was calculated that agreed with the accepted value for cylinder shedding frequency. The sine wave had a known amplitude, DC offset, and frequency. The sine wave was correctly sampled by the experimental system, and the generator into the experimental setup. The sine wave with a DC offset created by a function of  $S_f \equiv 0.2$ .

The third test involved feeding a sine wave with a DC offset created by a function of the hot-wire system, confidence was gained that the components were functioning properly. Experimentation on the SM701 airfoil could begin.

FFT power spectrum revealed the known frequency of the wave. From these three checks and frequency. The sine wave was correctly sampled by the experimental system, and the generator into the experimental setup. The sine wave had a known amplitude, DC offset, and frequency. The sine wave was correctly sampled by the experimental system, and the generator into the experimental setup. The sine wave with a DC offset created by a function of  $S_f \equiv 0.2$ .

The third test involved feeding a sine wave with a DC offset created by a function of the hot-wire system, confidence was gained that the components were functioning properly. Experimentation on the SM701 airfoil could begin.

Figure 5.26: Simple Propeller Test for Hot-Wire Measurement System



$\alpha$ (deg)	Chordwise Location of Hot-Wire Profile Sweep (%)	Wake Position of Sweep	25	30	70	80	90	0.25c	0.75c
X									
X									
X	X								
		X	X						
			X	X					
				X	X				
					X	X			
						X	X		
							X	X	
								X	X
									22
									25

Table 5.2: Test Matrix for Hot-Wire Experimentation

matrix is shown in Table 5.2. After sampling was completed at all points in the-traverse sweep, the tunnel was shut off and the traverse repositioned to allow experimentation at a new location. The test the fluctuation voltages were ten to 30 dB.

Figure 5.22 was set at 820 Hz for anti-aliasing purposes. Typical amplification factors of FFT frequency axis. The sampling time was 25.5 seconds. The low-pass filter seen in It was decided to reduce the sampling rate to 2048 Hz to increase the resolution on the resulting power spectra revealed no significant energy content above a few hundred Hertz. next traverse location. Several tests were done with sampling at 20.48 kHz, but the instantaneous hot-wire output voltage and the movement of the hot-wire sensor to the acquisition software described in Section 5.2.3 then directed the sampling of the data measurements.

The tunnel was brought up to speed to give a Reynolds number of 315,000. The data approximatively one millimeter off of the model surface for the chordwise profile free stream direction when studying the wake. The hot-wire sensor was positioned travelled normal to the chordline at the desired chordwise location or perpendicular to the 18°, 20°, 22°, and 25°. The traverse mount was then adjusted such that the hot-wire probe The angle of attack was set to the desired value. Angles of attack tested included 15°, 5.2.5 Procedure for Hot-Wire Flowfield Measurements

Results of the hot-wire anemometry experimentation are now presented. Discussion will begin for  $\alpha = 15^\circ$  and proceed through higher angles of attack. Figure 5.27 depicts the locations at which measurements were made for  $\alpha = 15^\circ$ . Two velocity profiles were recorded at 80% and 90% chord, and a wake survey 75% chord behind the airfoil's trailing edge was examined. Velocity profiles were measured starting one millimeter above the airfoil surface and proceeding upwards away from the surface in a normal direction. At the wake survey location the hot-wire probe was lowered as far as was physically possible, constrained by the length of the probe. This minimum position of the hot-wire probe was termed  $y = 0$ . The survey was taken by traversing the probe upwards through the wake.

Figures 5.28a and 5.29a give the measured streamwise mean and rms velocity profiles for 80% and 90% chord locations, respectively. The profiles are seen to be very repeatable. The mean profiles on the airfoil show no clear indication of flow separation and reversal. Thus the separation revealed in Figure 4.4a of Section 4.1.3 is confined to a region very near the airfoil surface that is no thicker than one or two millimeters. The rms profiles in Figures 5.28a and 5.29a show the typical maximum in the middle of the region very near the airfoil surface that is no thicker than one or two millimeters. The rms airfoil is 0.1 when nondimensionalized by  $U_\infty$ . The numbers at various data points on the airfoil are simply point numbers with the numbering system beginning with the data rms profiles are simply point numbers with the numbering system beginning with the data maximum  $u_{rms}/U_\infty$ . Above that peak  $u_{rms}/U_\infty$  location, the skewness becomes very negative due to the drastic decrease of  $u_{rms}$  in the free stream to values near 0.008 when until locations very near the free stream are reached. There, the skewness becomes very large due to the drastic decrease of  $u_{rms}$  in the free stream to values near 0.008 when

## 5.2.6 Hot-Wire Flowfield Measurements Results

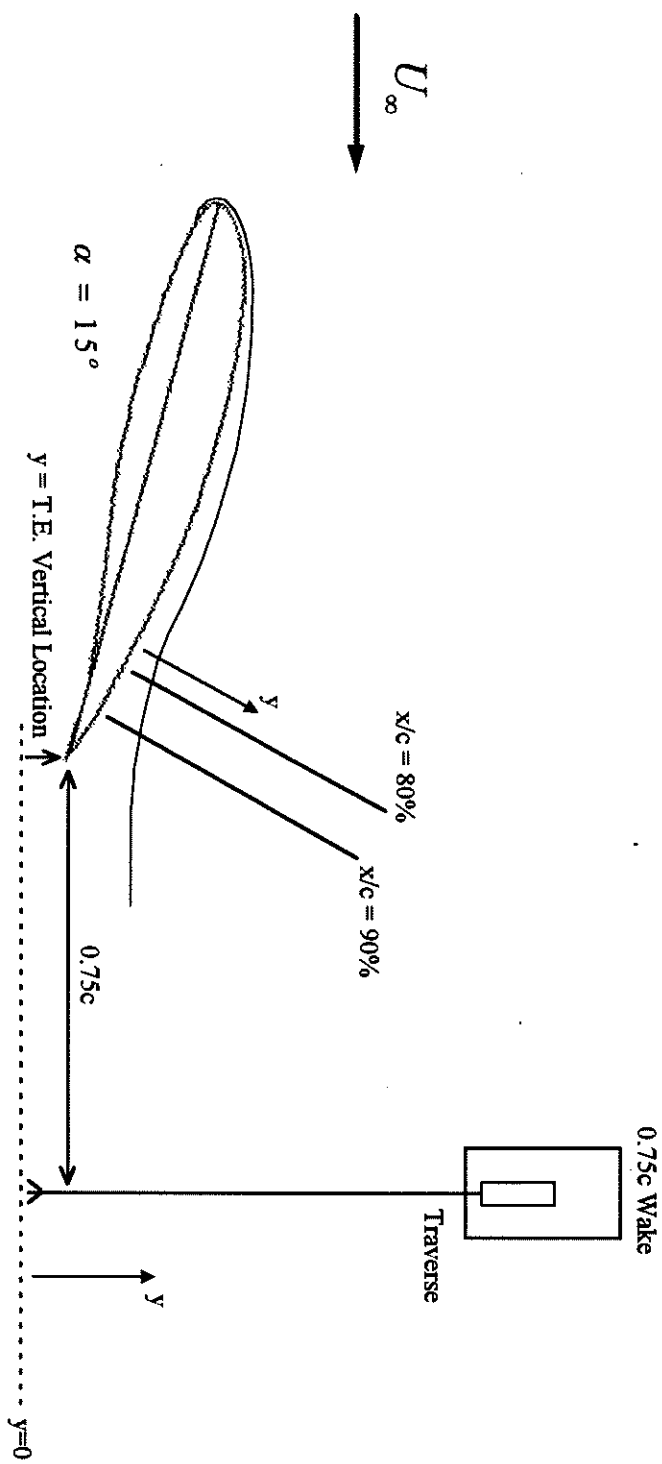


Figure 5.27: Velocity Profile and Wake Survey Locations for  $\alpha = 15^\circ$

Figure 5.28(a) and (b):  $\alpha = 15^\circ$ ;  $Re = 315,000$ ;  $X/c = 80\%$

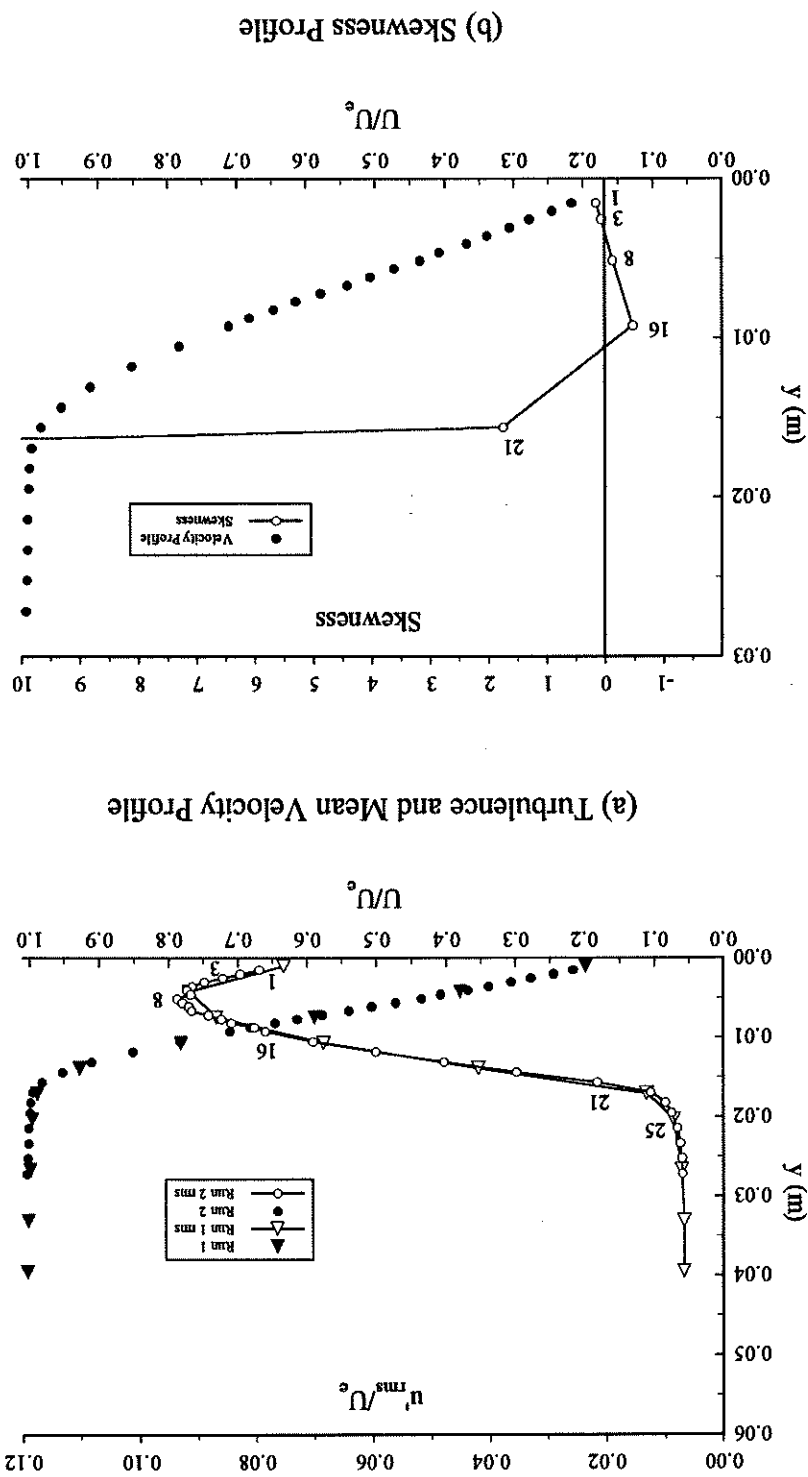
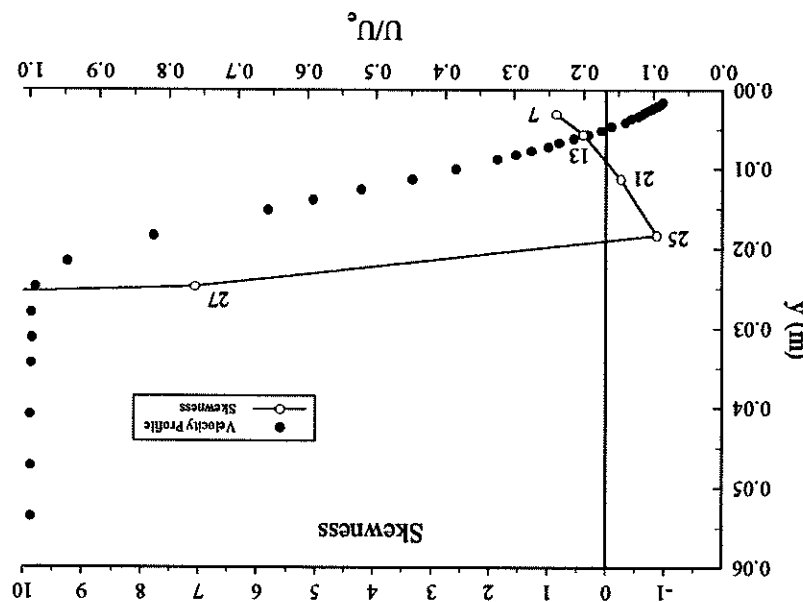
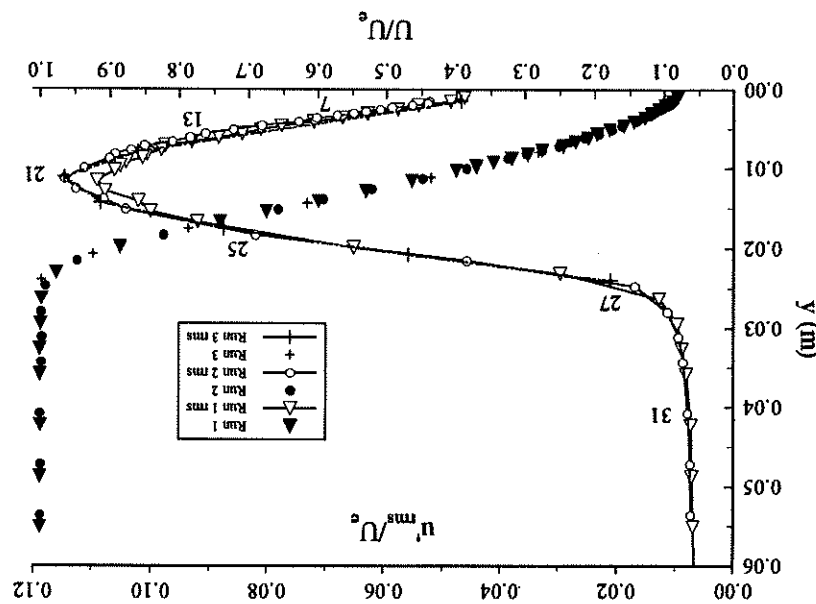


Figure 5.29(a) and (b):  $\alpha = 15^\circ$ ;  $Re = 315,000$ ;  $x/c = 90\%$

(b) Skewness Profile



(a) Turbulence and Mean Velocity Profile



The wake survey for  $\alpha = 15^\circ$  is given in Figure 5.30a. The wake is approximately six centimetres wide with only a 20% to 25% maximum wake velocity deficit. The rms profile shows two slight peaks, one for each region of high mean shear on either side of the wake. Rms fluctuation levels range from near 0.08 at the maximum to 0.01 at the minimum when nondimensionalized by  $U_\infty$ . The maximum rms fluctuation level has thus decayed slightly from the value seen in the velocity profiles on the airfoil (Figures 5.28a and 5.29a). Skewness in the wake is seen to be negative, Figure 5.30b. The trailing edge vertical location is marked on the graph. Refer back to Figure 5.27 which depicts this location.

The spectra calculated for the various numbered locations in the velocity profiles on the airfoil and in the wake survey profile did not reveal any dominant instabilities. Only broadband turbulence was seen (these graphs are not shown). The thinness of the separated flow region on the airfoil along with the thin wake, small wake velocity deficit, and broadband frequency spectra indicate that the airfoil at  $\alpha = 15^\circ$  and  $Re = 315,000$  is not severely stalled. In fact, the SM701 lift curve reaches a maximum very near  $\alpha = 15^\circ$  and compared to the  $\alpha = 15^\circ$  case at the 0.75c wake location ( $\equiv 25$  cm compared to  $\equiv 6$  cm). Also the maximum velocity deficit is much larger ( $\equiv 65\%$  compared to  $\equiv 25\%$ ). The rms maximum of about 0.25 to a minimum of about 0.04 (compared to 0.10 and 0.01 for  $\alpha = 15^\circ$ ). The rms maximum in the lower portion of the wake occurs at the same vertical location as the airfoil's trailing edge. The skewness in Figure 5.32b is seen to be positive between the two rms maxima locations in the middle of the two high mean shear regions. The skewness is negative outside of this rms peak-to-peak region. Note that the skewness does not obtain extremely large values in the upper free stream as had occurred for  $\alpha = 15^\circ$ , this may be attributed to higher  $U_\infty$  values in the free stream at  $\alpha = 18^\circ$ .

Figure 5.31 shows the location of the wake survey that was performed for  $\alpha = 18^\circ$ . The mean and rms velocity profiles are given in Figure 5.32a. The wake is much wider than for  $\alpha = 15^\circ$  case at the 0.75c wake location ( $\equiv 25$  cm compared to  $\equiv 6$  cm). The mean fluctuation level nondimensionalized by  $U_\infty$  has also increased greatly, ranging from a maximum of about 0.25 to a minimum of about 0.04 (compared to 0.10 and 0.01 for  $\alpha = 15^\circ$ ). The rms maximum in the lower portion of the wake occurs at the same vertical location as the airfoil's trailing edge. The skewness in Figure 5.32b is seen to be positive between the two rms maxima locations in the middle of the two high mean shear regions. The skewness is negative outside of this rms peak-to-peak region. Note that the skewness does not obtain extremely large values in the upper free stream as had occurred for  $\alpha = 18^\circ$ .

Figure 5.31 shows the location of the wake survey that was performed for  $\alpha = 18^\circ$ .

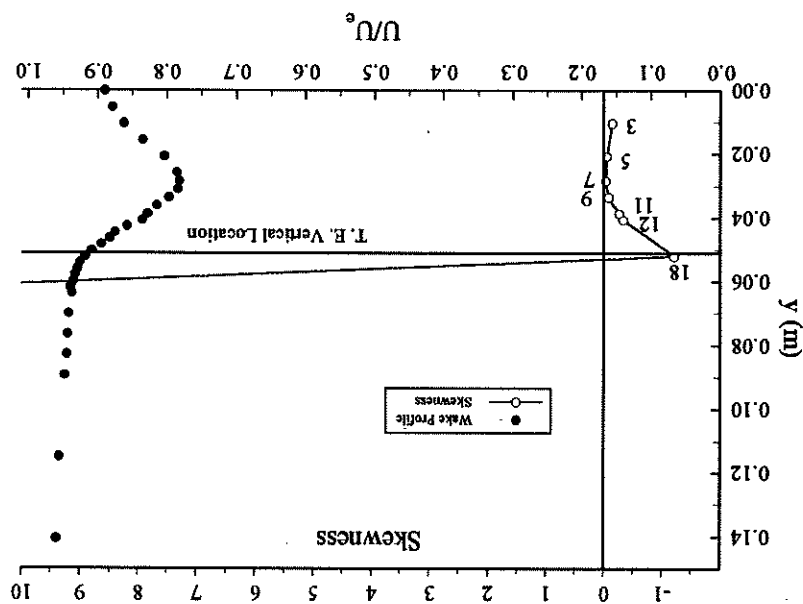
beginning to enter the stalled regime.

for  $Re = 315,000$ . Thus it is clear that for this test configuration, the airfoil is just not severely stalled. In fact, the SM701 lift curve reaches a maximum very near  $\alpha = 15^\circ$  and broadband frequency spectra indicate that the airfoil at  $\alpha = 15^\circ$  and  $Re = 315,000$  is separated flow region on the airfoil along with the thin wake, small wake velocity deficit, broadband turbulence was seen (these graphs are not shown). The thinness of the separated flow region on the airfoil along with the thin wake, small wake velocity deficit, and broadband frequency spectra indicate that the airfoil at  $\alpha = 15^\circ$  and  $Re = 315,000$  is not severely stalled. In fact, the SM701 lift curve reaches a maximum very near  $\alpha = 15^\circ$  and compared to the  $\alpha = 15^\circ$  case at the 0.75c wake location ( $\equiv 25$  cm compared to  $\equiv 6$  cm). The mean fluctuation level nondimensionalized by  $U_\infty$  has also increased greatly, ranging from a maximum of about 0.25 to a minimum of about 0.04 (compared to 0.10 and 0.01 for  $\alpha = 15^\circ$ ). The rms maximum in the lower portion of the wake occurs at the same vertical location as the airfoil's trailing edge. The skewness in Figure 5.32b is seen to be positive between the two rms maxima locations in the middle of the two high mean shear regions. The skewness is negative outside of this rms peak-to-peak region. Note that the skewness does not obtain extremely large values in the upper free stream as had occurred for  $\alpha = 18^\circ$ .

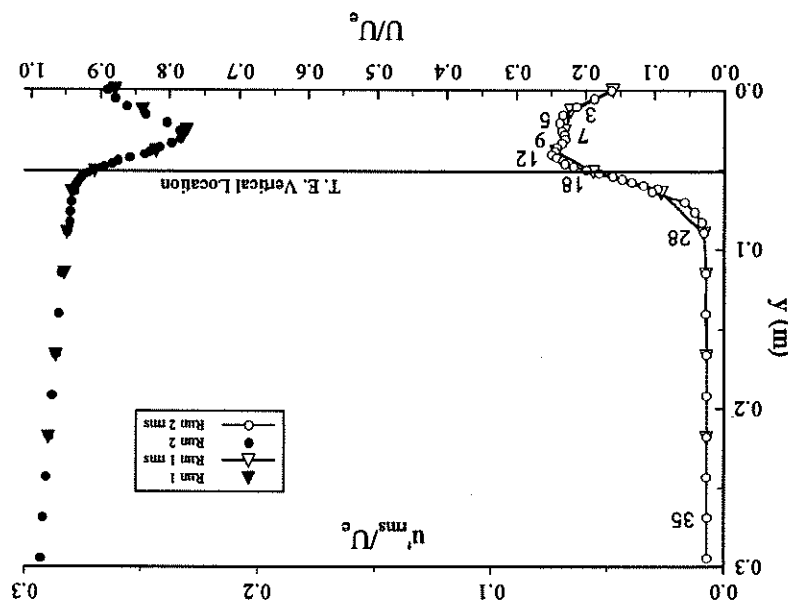
The spectra calculated for the various numbered locations in the velocity profiles on the airfoil and in the wake survey profile did not reveal any dominant instabilities. Only broadband turbulence was seen (these graphs are not shown). The thinness of the separated flow region on the airfoil along with the thin wake, small wake velocity deficit, and broadband frequency spectra indicate that the airfoil at  $\alpha = 15^\circ$  and  $Re = 315,000$  is not severely stalled. In fact, the SM701 lift curve reaches a maximum very near 0.08 at the 0.75c wake location ( $\equiv 25$  cm compared to  $\equiv 6$  cm). The mean fluctuation level nondimensionalized by  $U_\infty$  has thus decayed slightly from the value seen in the velocity profiles on the airfoil (Figures 5.28a and 5.29a). Skewness in the wake is seen to be negative, Figure 5.30b. The trailing edge vertical location is marked on the graph. Refer back to Figure 5.27 which depicts this location.

Figure 5.30(a) and (b):  $\alpha = 15^\circ$ ;  $Re = 315,000$ ; 0.75c Wake

(b) Skewness Profile



(a) Turbulence and Mean Velocity Profile



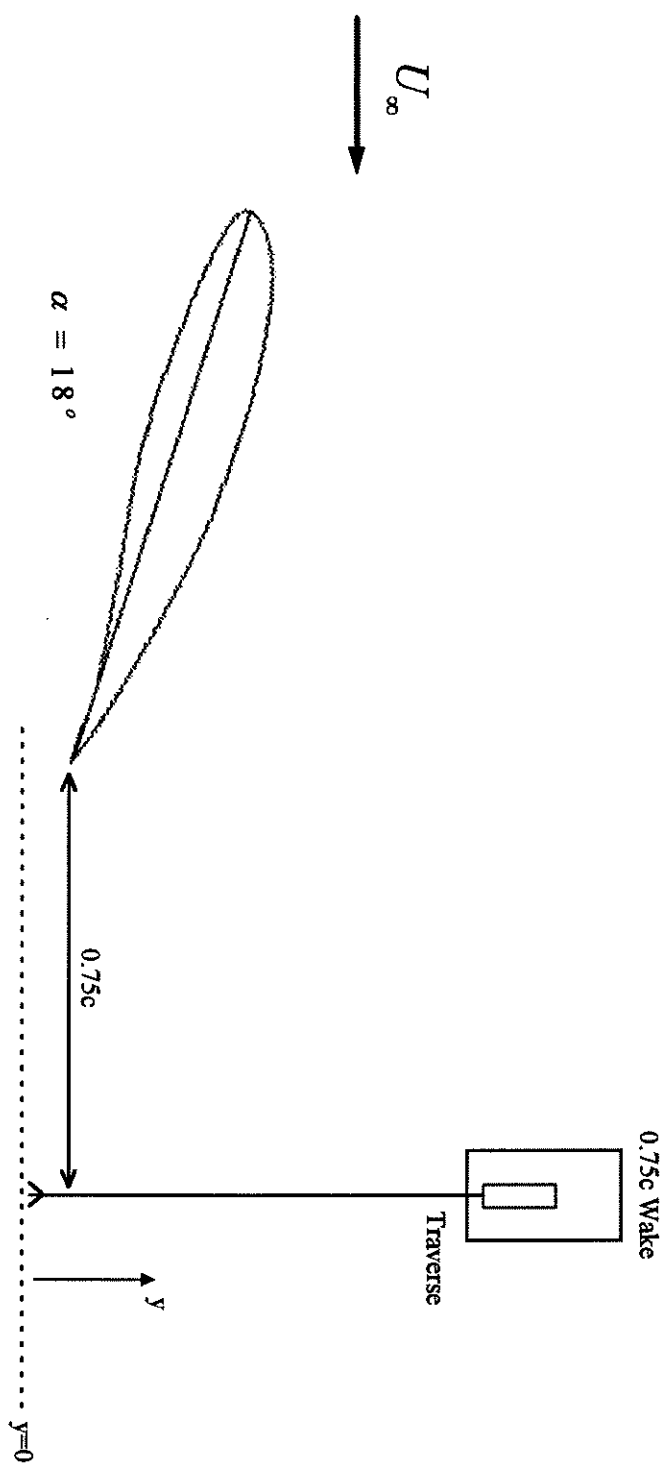


Figure 5.31: Wake Survey Location for  $\alpha = 18^\circ$

Figure 5.32(a) and (b):  $\alpha = 18^\circ$ ;  $Re = 315,000$ ; 0.75C Wake

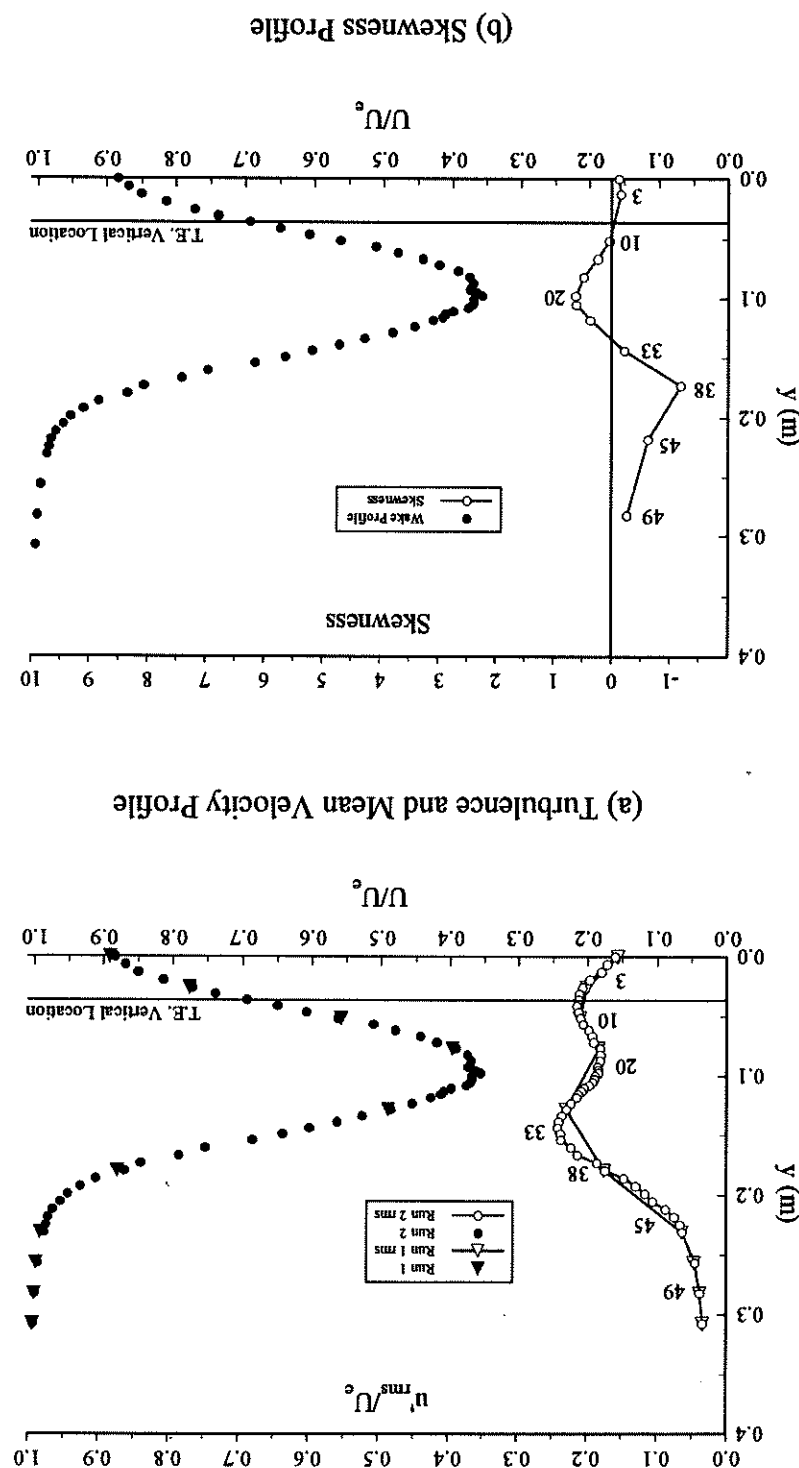
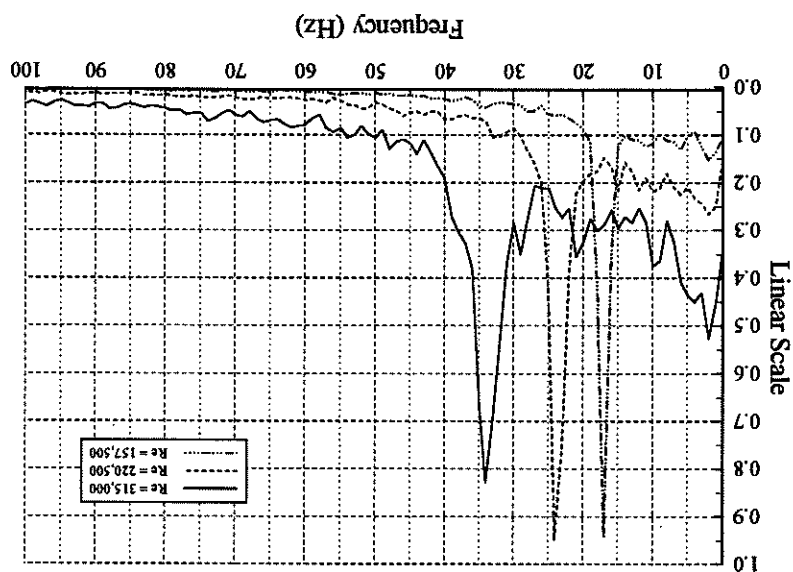


Figure 5.33a shows the spectra at the numbered locations in Figure 5.32a. It is obvious that a dominant flow structure exists at the 0.75c wake position for  $\alpha = 18^\circ$ . The frequency of this flow structure is approximately 34 Hz. From Figure 5.33a, the best hot-wire locations for measuring this dominant flow instability seem to be positions 3, 10, 33, and 38 which are located in the regions of high mean shear near the maximum  $u_{ms}$  point and 38 which are located in the regions of high mean shear near the maximum  $u_{ms}$  point on both sides of the wake. The instability is not seen well at positions 20, 45, or 49. Position 20 is at the maximum velocity defect location. Positions 45 and 49 are at the outer edge of the upper high mean shear region and in the free stream, respectively. This dominant flow instability is seen to vary with  $U_\infty$  in Figure 5.33b. When the modified Strouhal number is calculated for each Reynolds number given in Figure 5.33b, a constant value of  $\approx 0.20$  is obtained.

Skewness has been discussed now for  $\alpha = 15^\circ$  and  $\alpha = 18^\circ$ . Figure 5.34a shows typical velocity fluctuation signals for  $\alpha = 18^\circ$ . The upper signal is positively skewed, the middle signal has a skewness near zero, and the bottom signal is negatively skewed. (For example, positive skewness means that most of the time the signal is at relatively small negative values, but relatively large positive fluctuations do occur. No relatively large negative fluctuations exist). The fluctuation levels in Figure 5.34a are seen to be very large when compared to the mean velocity levels upon which they are imposed. For position 20 the mean velocity is near 7 m/s. For position 33 the mean velocity is near 12 m/s, and for position 38 the mean velocity is near 15 m/s. From the velocity fluctuation signals in Figure 5.34a, the flow is seen to fluctuate from its mean value to very near zero. Positive fluctuations are on the order of the mean velocity. It is thus seen that the flow is extremely unsteady, and the airfoil at  $\alpha = 18^\circ$  is in the stalled regime. Figure 5.34b shows the probability density function computed for various wake points. The lines on this graph give a visual indication of the velocity fluctuation skewness at points in the wake survey. For instance, by examining the area under the curve for position 20, it is seen that at that position the velocity fluctuations are most likely to be in a negative velocity range. However, the curve for position 20 also shows that relatively large positive velocity fluctuations can occur but at a reduced probability.

Figure 5.33(a) and (b):  $\alpha = 18^\circ$ ; 0.75c Wake

(b) Free Stream Velocity Effects; Pos. 33



(a) Power Spectrum ( $Re = 315,000$ )

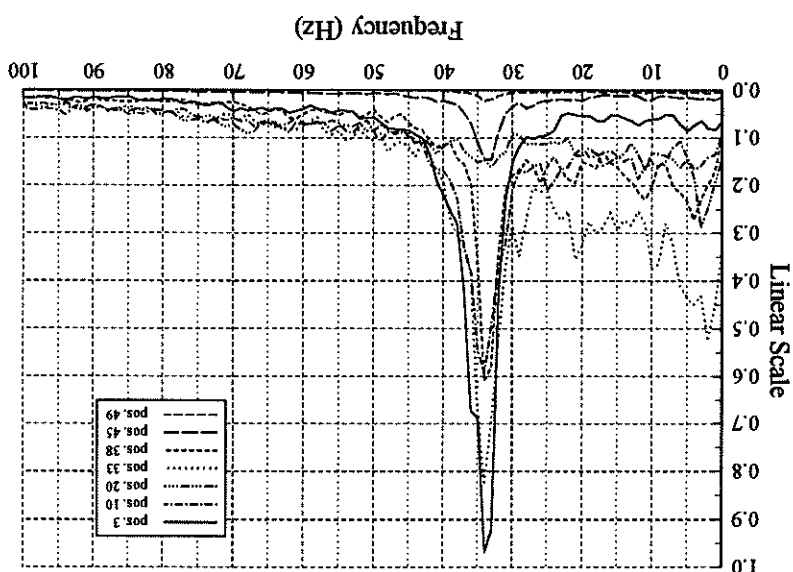
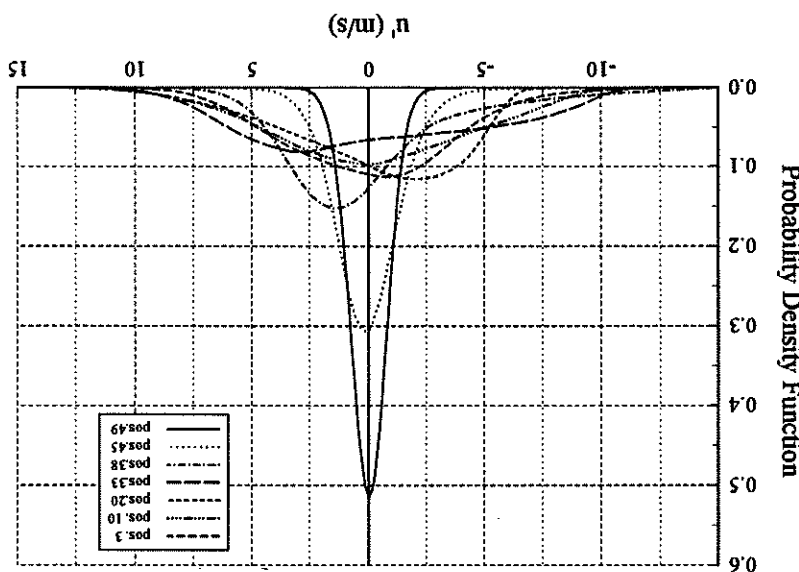
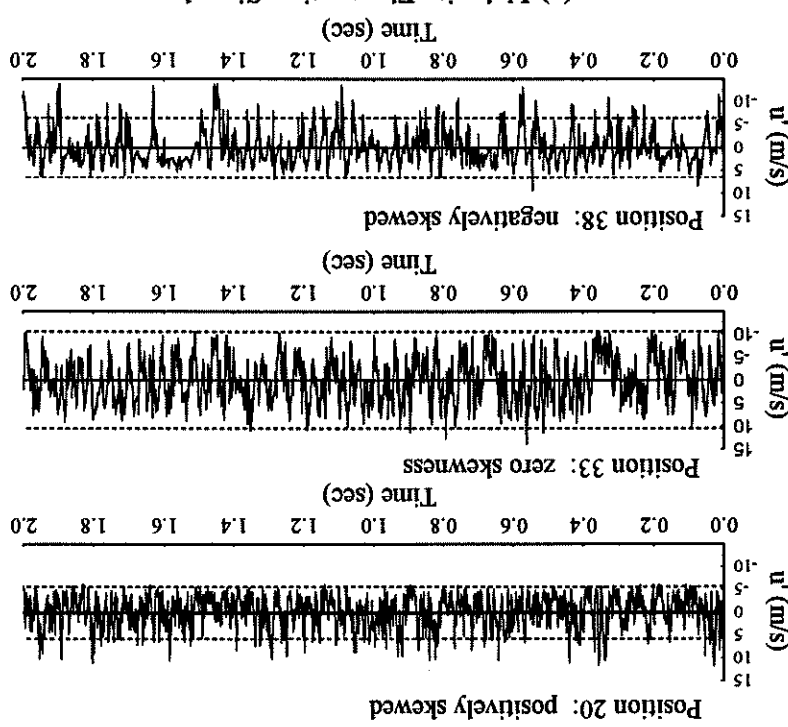


Figure 5.34(a) and (b):  $\alpha = 18^\circ$ ,  $Re = 315,000$ , 0.75C Wake

(b) Probability Density Function



(a) Velocity Fluctuation Signals



flow reversal occurs. This rectification causes the measured  $U_{mean}$  values to be too high

The hot-wire output voltage displays a folding or rectification (shaded areas) when signal in such a reversing flow is shown in Figure 5.39.

wire as a certain voltage regardless of the direction of the flow. A sample of a hot-wire measurements will result. For instance, a given flow speed will be registered by the hot-wire sensor is put in a reversing flow, such as the flow region near the boundary between the reverse flow and the shear layer flow on a stalled airfoil, ambiguity in the velocity detection a reversal of flow direction due to the symmetry of the sensing element. If a hot-wire can be found if hot-wire rectification is examined. A single sensor hot-wire can not detect a reversal of flow direction due to the symmetry of the sensing element. If a hot-wire sensor is put in a reversing flow, such as the flow region near the boundary between the reverse flow and the shear layer flow on a stalled airfoil, ambiguity in the velocity uncertainty in the velocity calculations alone. A possible explanation for this apparent

order of  $U/U_e \approx 0.15$  or  $U = 2$  m/s on the average. This shift can not be caused by than a percent. The shift seen in the mean profiles in Figures 5.36a to 5.38a is on the expected. For calculated velocities above one meter per second, the uncertainty is less For calculated velocities below one meter per second, only a two percent uncertainty is from which instantaneous velocity values are computed from the hot-wire output voltage. For calculating velocities below one meter per second, only a two percent uncertainty is shear region. A sensitivity analysis was performed on the hot-wire calibration polynomial also of interest is the apparent shift of the nondimensional mean velocity data by about 0.13 on the abscissa, Figure 5.36a. The mean data do not show the mean velocity 50%, and 70%, respectively.

flow region thicknesses are approximately one, three, and five centimetres for  $x/c = 25\%$ , region since the single sensor hot-wire is not directionally sensitive. Estimates of reverse near the wall. It is impossible to tell precisely, however, the thickness of the reverse flow data seem to indicate the flow reversal near the surface by an increase in mean velocity appears that a reverse flow region exists on the airfoil for these test conditions. The mean Figures 5.36a to 5.38a for chordwise locations of 25%, 50%, and 70%, respectively. It wake survey locations for  $\alpha = 20^\circ$ . The mean and rms velocity profiles are given in Figure 5.35 shows the three velocity profile locations on the airfoil along with the two

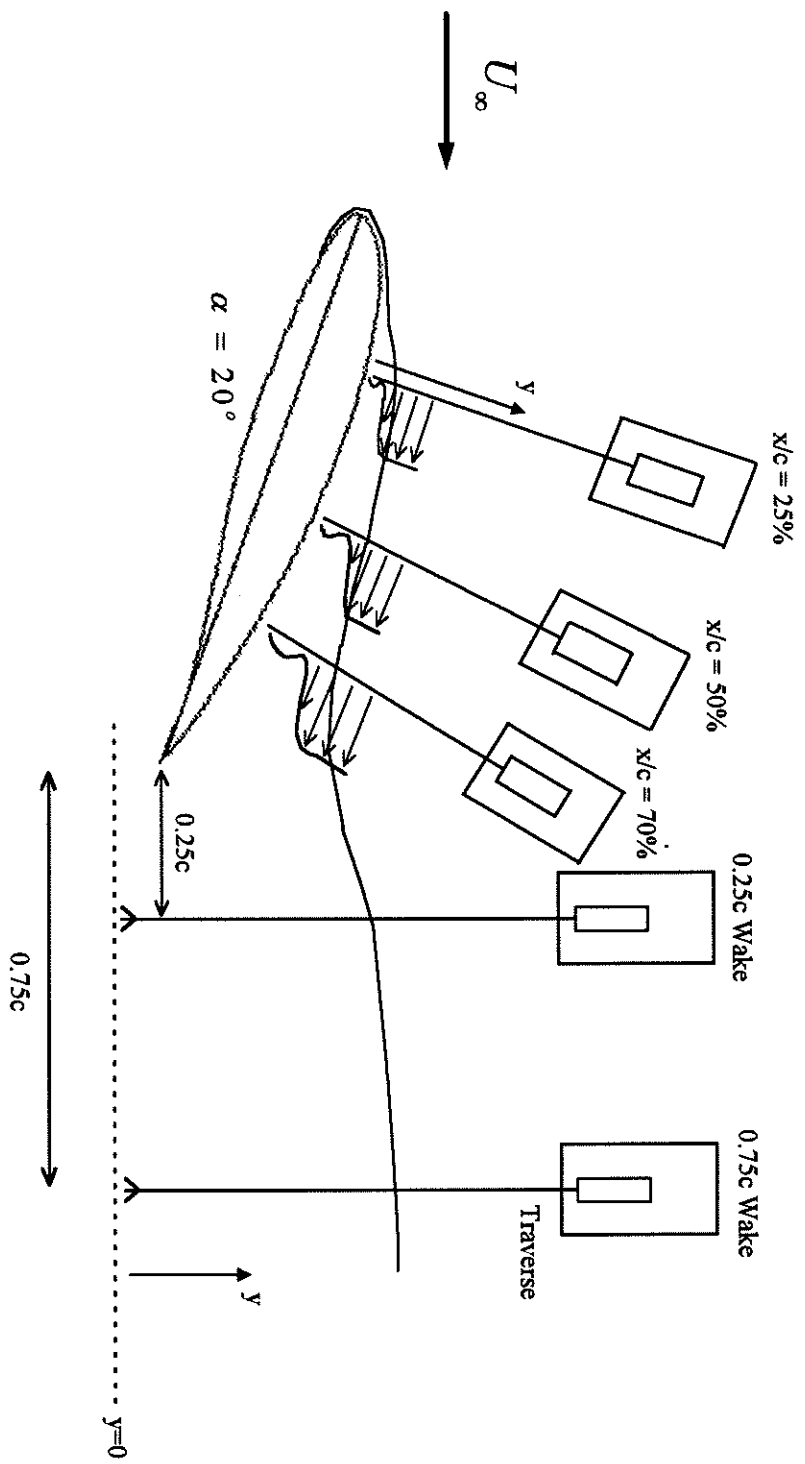
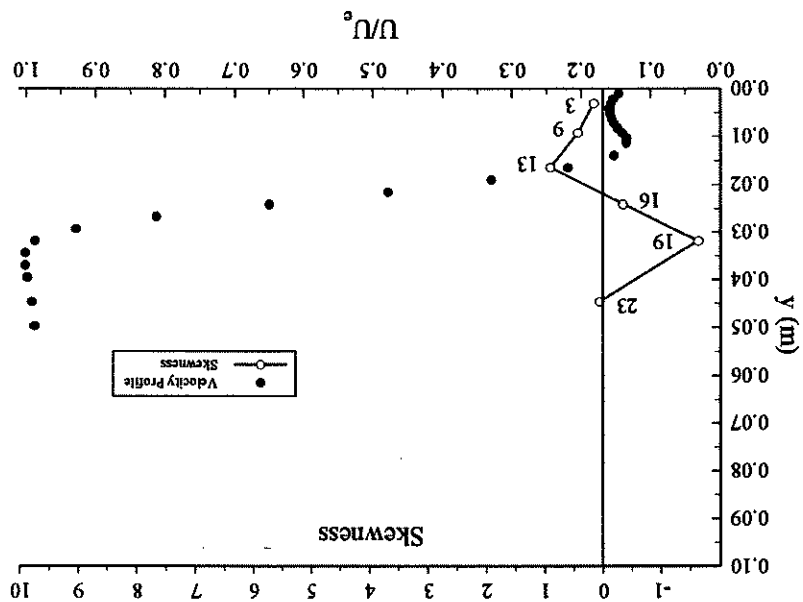


Figure 5.35: Velocity Profile and Wake Survey Locations for  $\alpha = 20^\circ$

Figure 5.36(a) and (b):  $\alpha = 20^\circ$ ;  $Re = 315,000$ ;  $x/c = 25\%$

(b) Skewness Profile



(a) Turbulence and Mean Velocity Profile

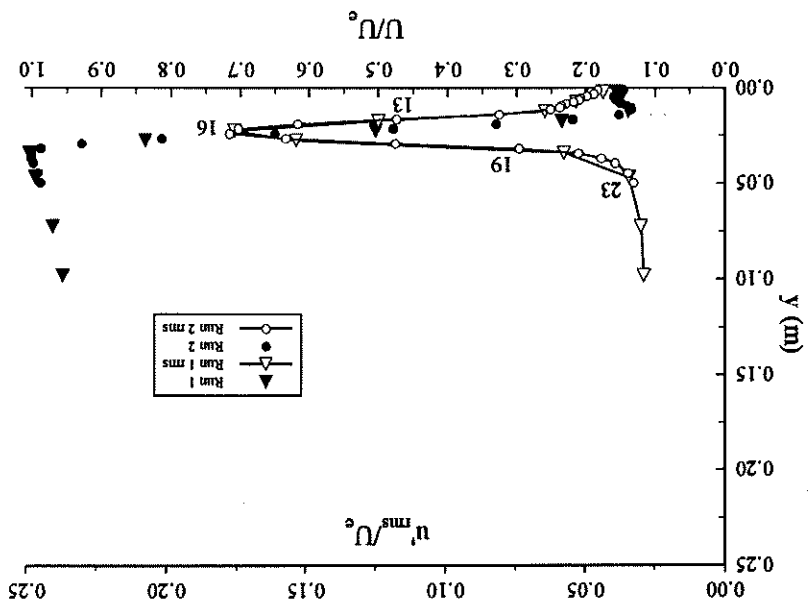
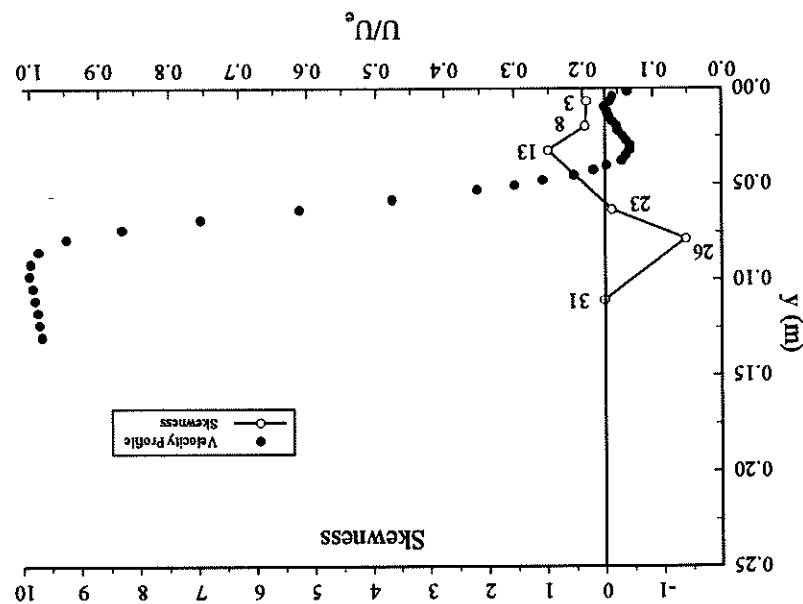


Figure 5.37(a) and (b):  $\alpha = 20^\circ$ ,  $Re = 315,000$ ,  $x/c = 50\%$

(b) Skewness Profile



(a) Turbulence and Mean Velocity Profile

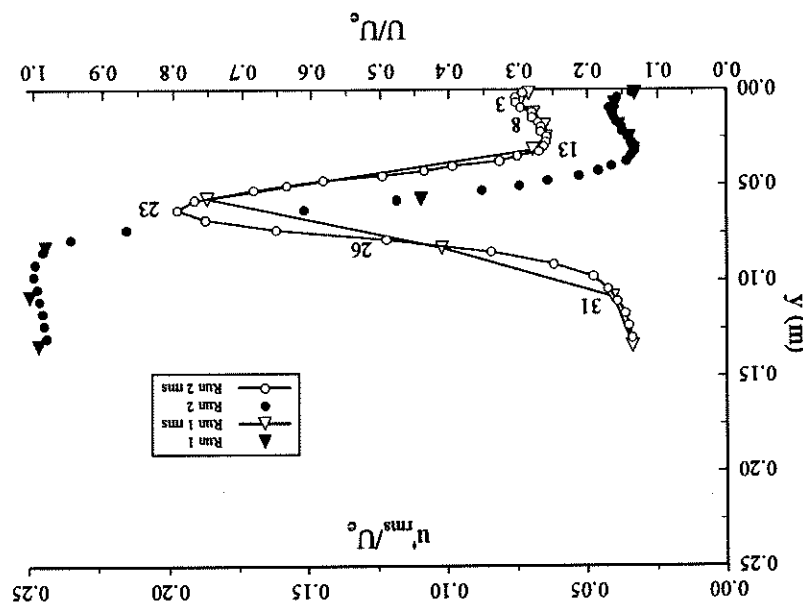
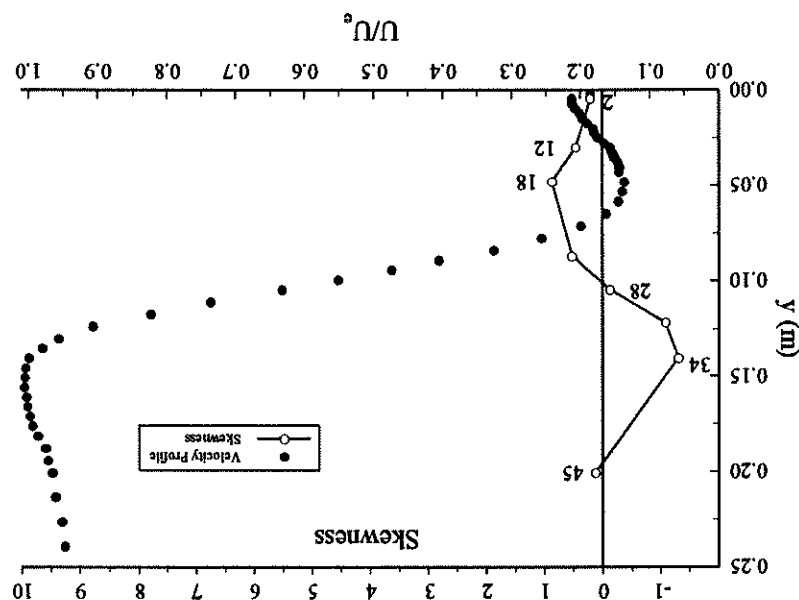


Figure 5.38(a) and (b):  $\alpha = 20^\circ$ ;  $Re = 315,000$ ;  $x/c = 70\%$

(b) Skewness Profile



(a) Turbulence and Mean Velocity Profile

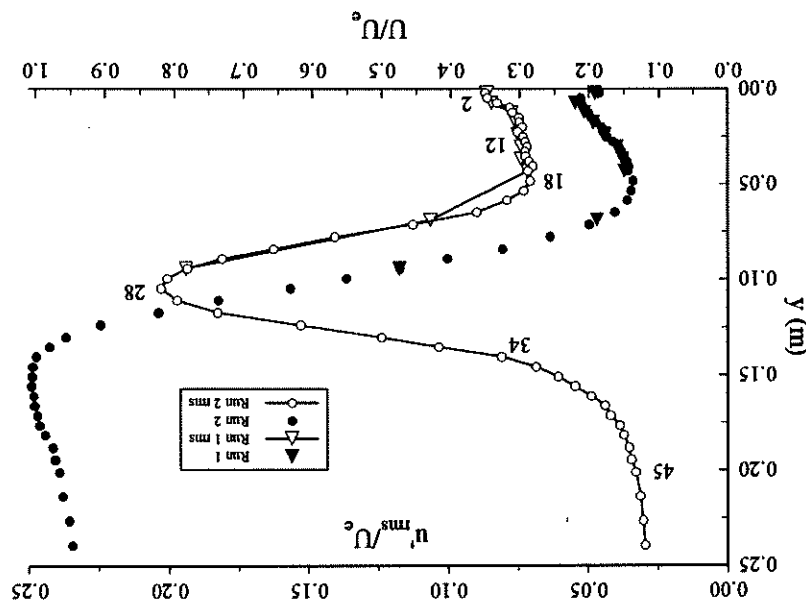
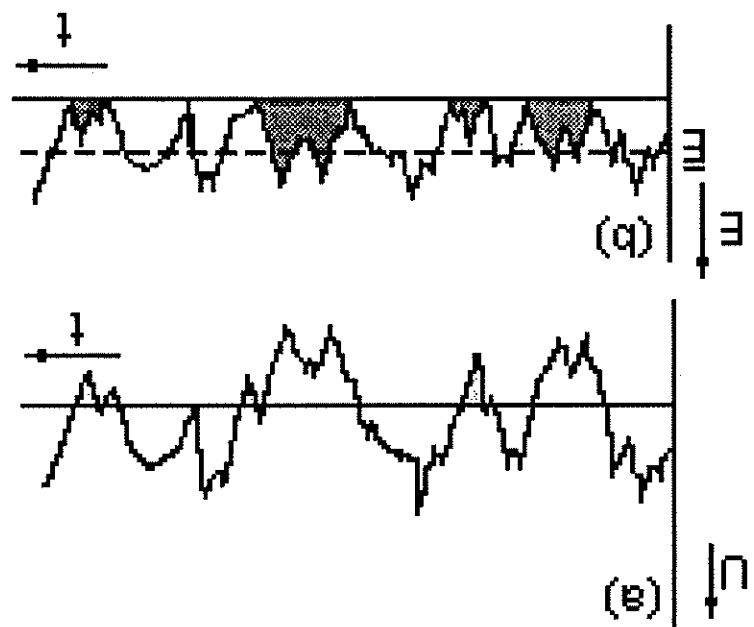


Figure 5.39: Hot-Wire Rectification in 1D Reversing Flowfield

Source: Bruun, 1995



and the measured  $u_{rms}^{1/2}$  values to be too low (Bruun, 1995). Thus, hot-wire rectification could be causing the mean data of Figures 5.36a to 5.38a to be too high near the boundary between the reverse flow region and the separated shear layer.

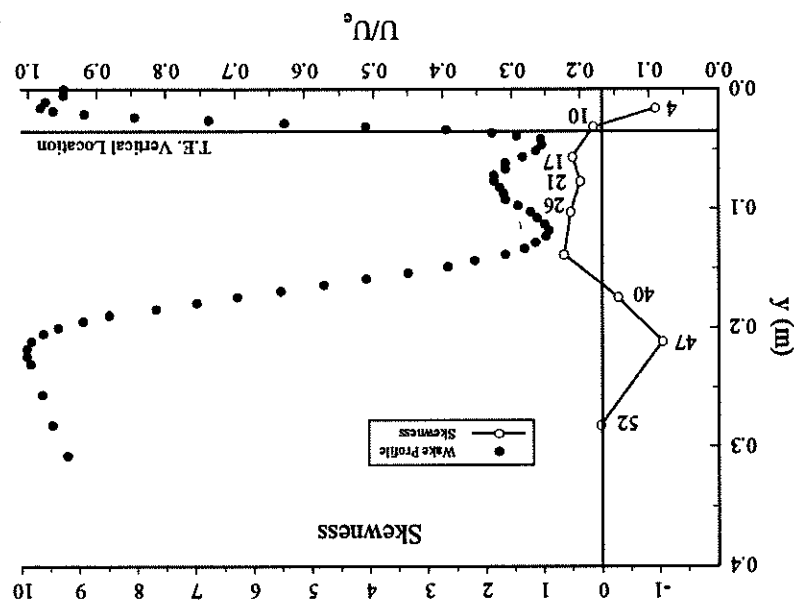
The skewness profiles for chordwise locations of 25%, 50%, and 70% are given as Figures 5.36b to 5.38b, respectively. For all three chordwise locations, the flow is positively skewed between the wall and the location of maximum  $u_{rms}/U$ . Above that peak  $u_{rms}/U$ , location, the flow is negatively skewed.

Wake survey results are given in Figures 5.40 and 5.41. As was the case for  $\alpha = 18^\circ$ , a local  $u_{rms}/U$  maximum occurs at the same vertical location as the airfoil's trailing edge. Rms levels are consistent with results for  $\alpha = 18^\circ$ . The velocity fluctuations are positively skewed between the two local  $u_{rms}/U$  maxima and negatively skewed outside of this rms peak-to-peak region (Figures 5.40b and 5.41b).

Power spectra were calculated for the various numbered points given in Figures 5.36 to 5.41. Figure 5.42 shows the development of a dominant flow instability over the chord to 5.41. Figure 5.42 shows the development of a dominant flow instability over the chord change at  $x/c = 50\%$  from  $x/c = 25\%$ . By 70% chord, a very slight indication of a dominant instability frequency begins to appear at position 45 located in the free stream (see Figure 5.42c). A subharmonic is also noticed. By the 0.25c wake location, the instability has amplified to be very noticeable. Figure 5.42d shows the instability to be approximately 33 Hz. Spectra at points 4, 10, 40, and 47 provide the strongest indication of the instability. These points are located in the regions of high mean shear between the maximum  $u_{rms}/U$  location and the free stream (refer back to Figure 5.40a). It appears that the lower half of the wake (positions 4 and 10) provides a slightly stronger indication of the instability than the upper half of the wake (positions 40 and 47). Position 26, located in the maximum velocity deficit region of the wake, does not provide a clear indication of a dominant instability frequency.

Figure 5.40(a) and (b):  $\alpha = 20^\circ$ ;  $Re = 315,000$ ; 0.25c Wake

(b) Skewness Profile



(a) Turbulence and Mean Velocity Profile

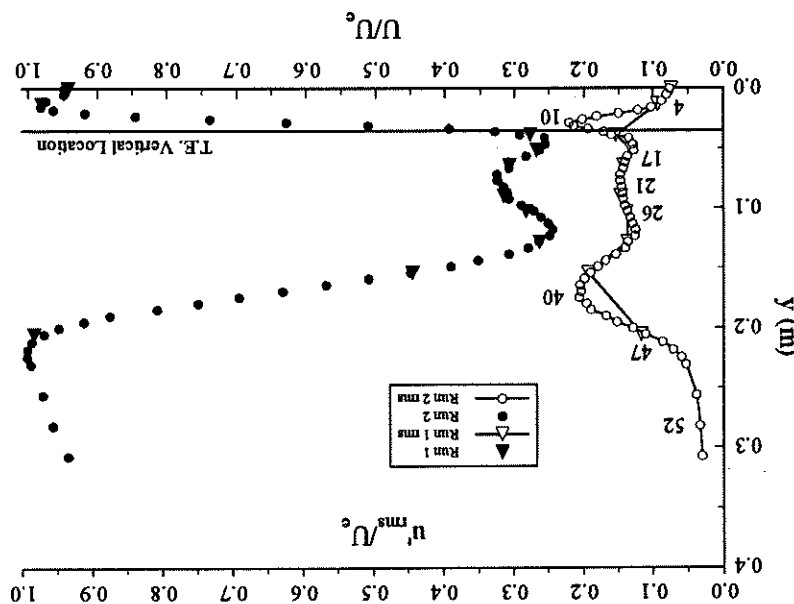
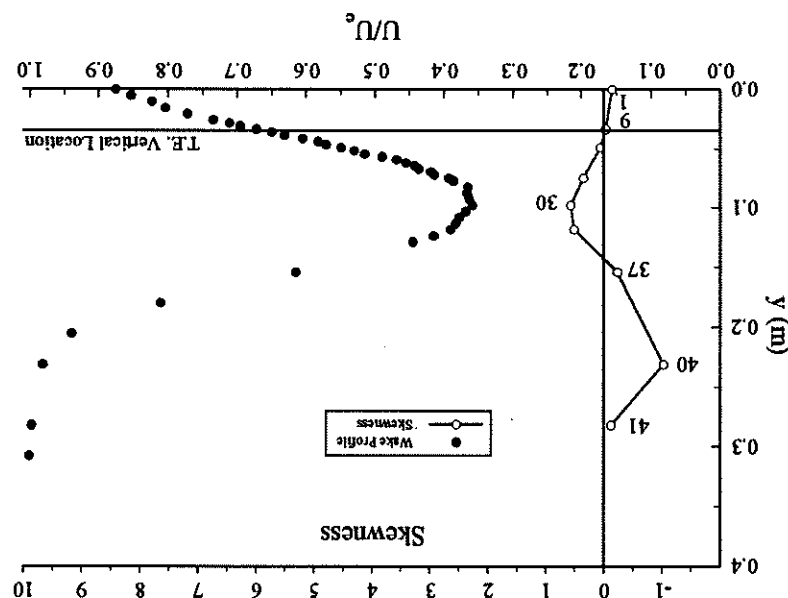


Figure 5.41(a) and (b):  $\alpha = 20^\circ$ ;  $Re = 315,000$ ; 0.75c Wake

(b) Skewness Profile



(a) Turbulence and Mean Velocity Profile

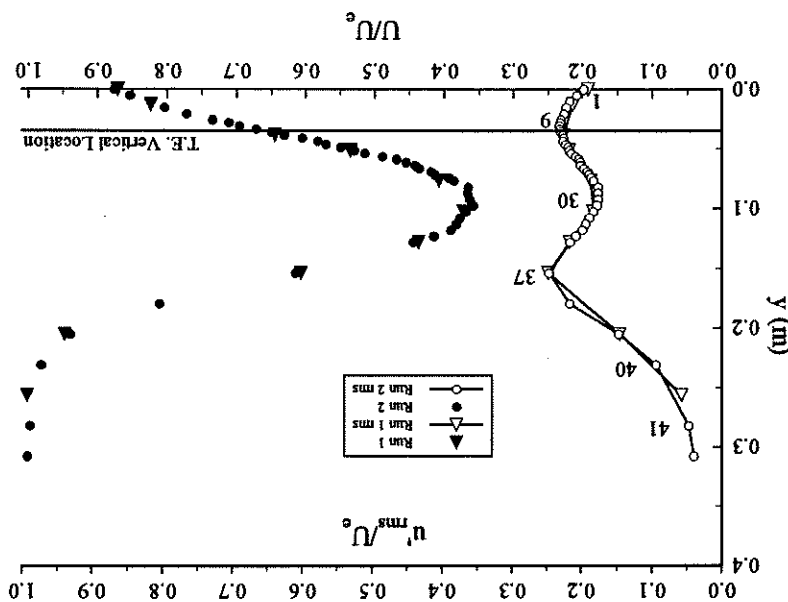
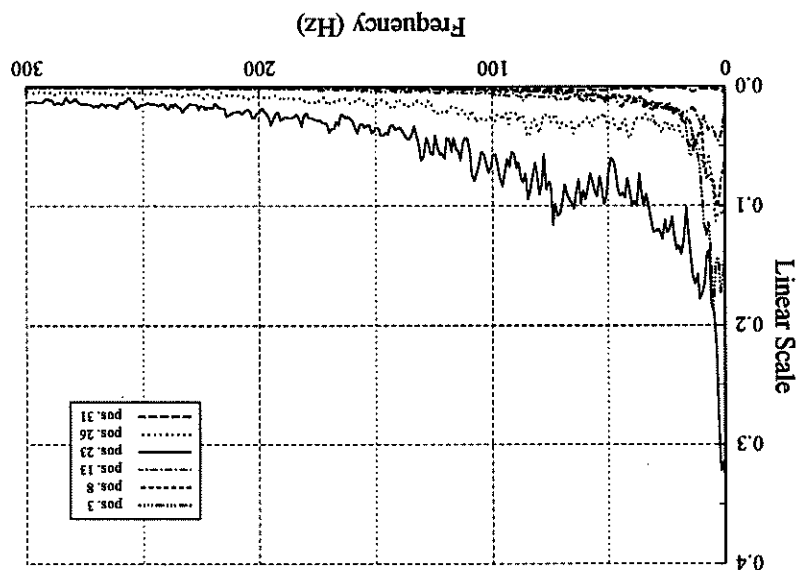


Figure 5.42(a) and (b):  $\alpha = 20^\circ$ ;  $Re = 315,000$

(b) Power Spectrum ( $x/c = 50\%$ )



(a) Power Spectrum ( $x/c = 25\%$ )

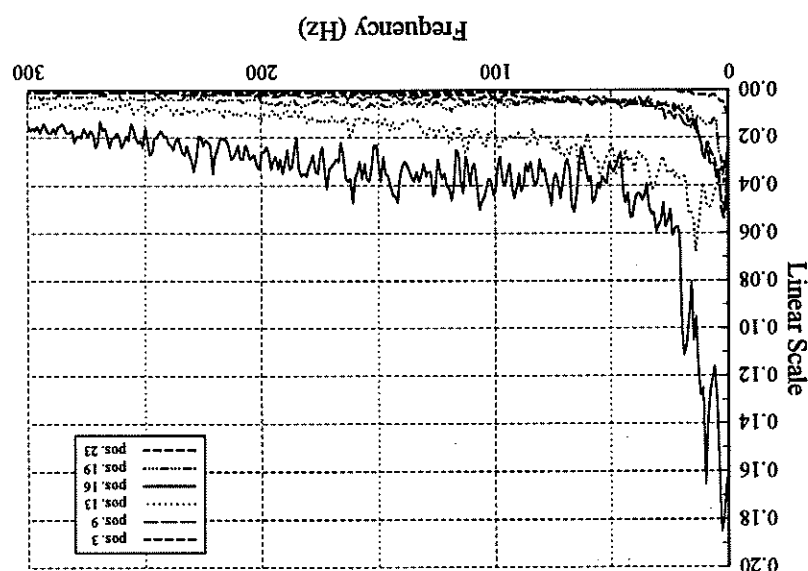
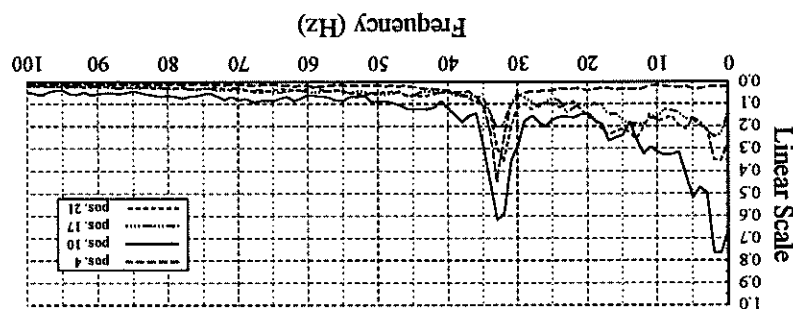
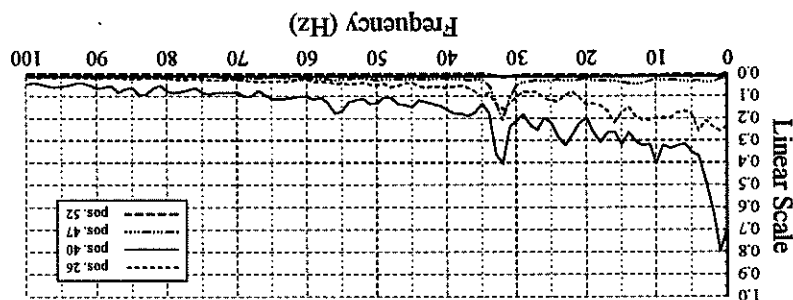


Figure 5.42(c) and (d):  $\alpha = 20^\circ$ ;  $Re = 315,000$

(d) Power Spectrum ( $0.25c$  Wake)



(c) Power Spectrum ( $x/c = 70\%$ )

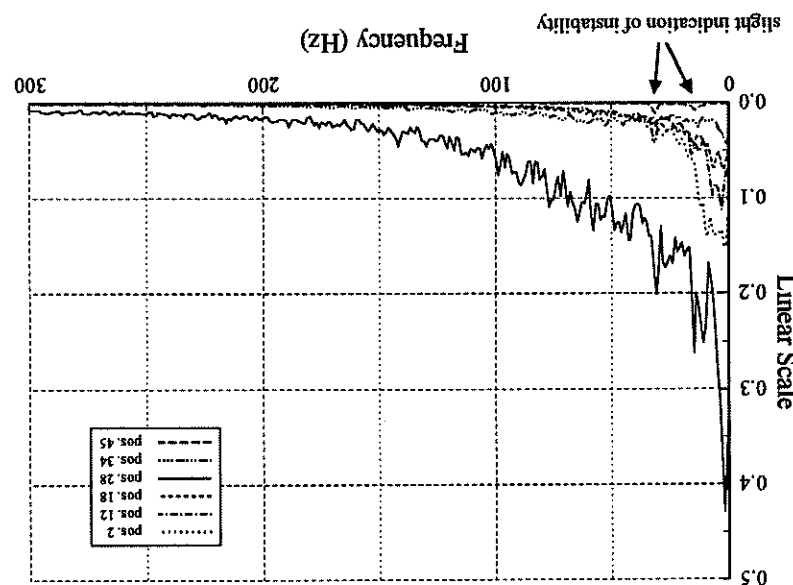


Figure 5.42(e):  $\alpha = 20^\circ$ ,  $Re = 315,000$

(e) Power Spectrum (0.75c Wake)

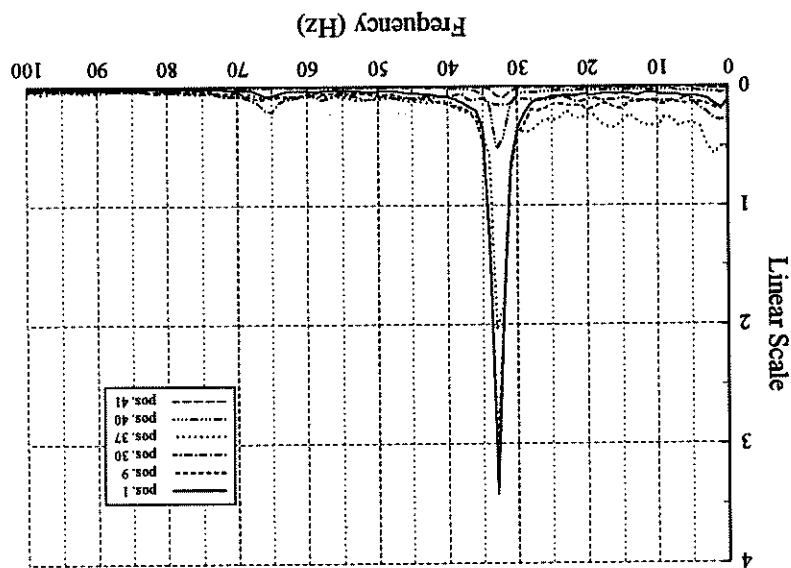


Figure 5.45 shows the wake survey location for  $\alpha = 25^\circ$ . Mean and rms velocity occurs at the same vertical location as the airfoil trailing edge. The velocity fluctuations consistent with the other stalled angle of attack cases. A maximum in the rms profile profiles are given in Figure 5.46a with skewness results in Figure 5.46b. Again, trends are

of approximately 59 Hz, a harmonic of the dominant 30 Hz instability frequency.

defect location gives no indication of a dominant instability but does indicate a frequency stream, respectively, of the upper half of the wake. Position 17 at the maximum velocity positions 29 and 45 lie near the maximum velocity defect location and near the free seen at points 29 and 45 to a lesser extent than for the previously discussed wake points. Positions 3 and 8 in the lower half of the wake. The dominant instability frequency is also maximum locations. The frequency peaks of the spectra are actually the strongest at points 3, 8, and 35 which lie in the regions of maximum shear near the  $U_{\text{rms}}/U$ . numbered positions indicated in Figure 5.44a. The dominant instability was best indicated frequency of about 30 Hz surface when velocity fluctuations spectra were examined at the of this rms peak-to-peak region, the skewness is negative. A dominant instability the maximum velocity defect region located between the two local rms maxima. Outside 0.25 when nondimensionalized by  $U$ . The velocity fluctuations are positively skewed in the same vertical position as the airfoil trailing edge. Rms maxima are on the order of consistent with wake results for  $\alpha = 18^\circ$  and  $\alpha = 20^\circ$ . The lower rms maximum occurs profiles are given in Figure 5.44a. Skewness is presented in Figure 5.44b. Trends are

Figure 5.43 depicts the wake survey location for  $\alpha = 22^\circ$ . The mean and rms velocity

reveal the dominant instability frequency but does give an indication of its first harmonic.

the best indication. Position 30, located in the maximum velocity defect region, does not location and the free stream. The positions in the lower half of the wake (1 and 9) give

high mean shear regions on both sides of the wake between the maximum  $U_{\text{rms}}/U$ .

37, and 40 most clearly indicate the dominant instability. These points are located in the instability frequency of 33 Hz is clearly seen along with its first harmonic. Locations 1, 9,

Figure 5.42 contains spectra for the 0.75C wake location. At this location a dominant

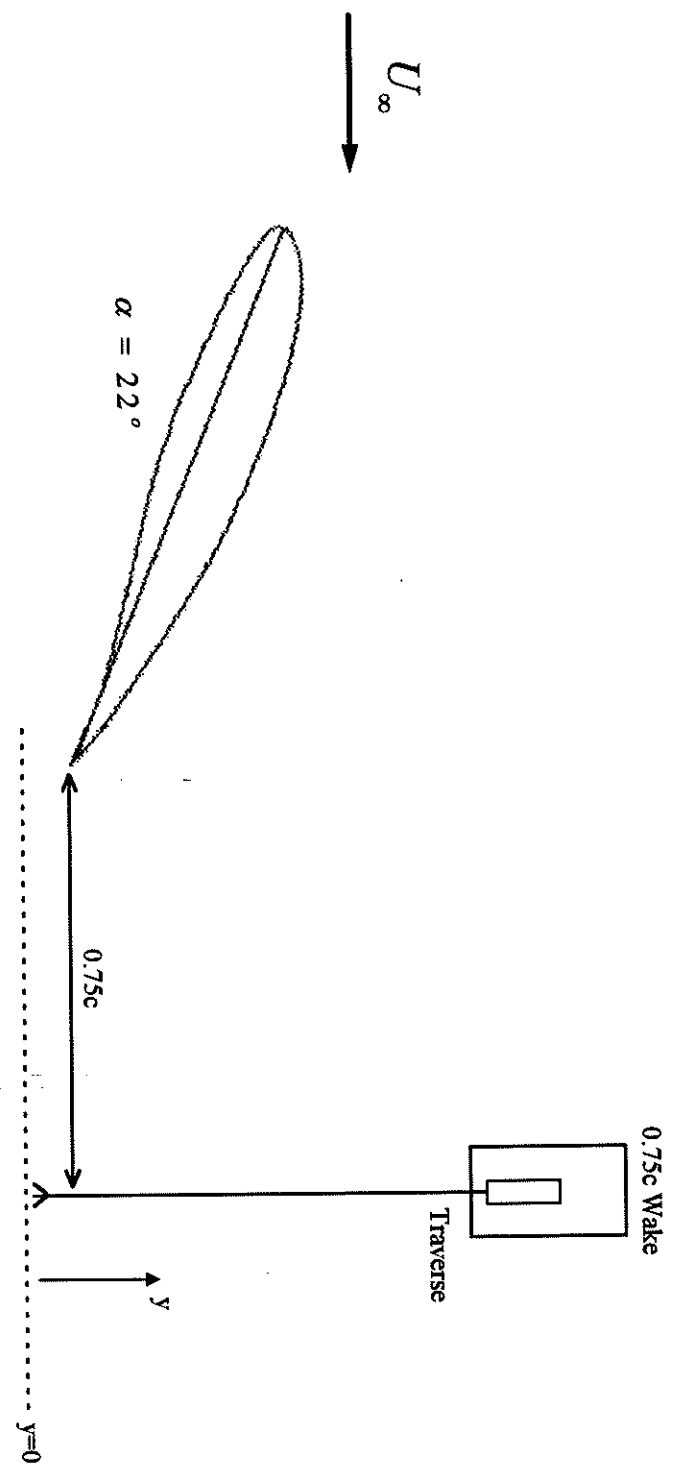
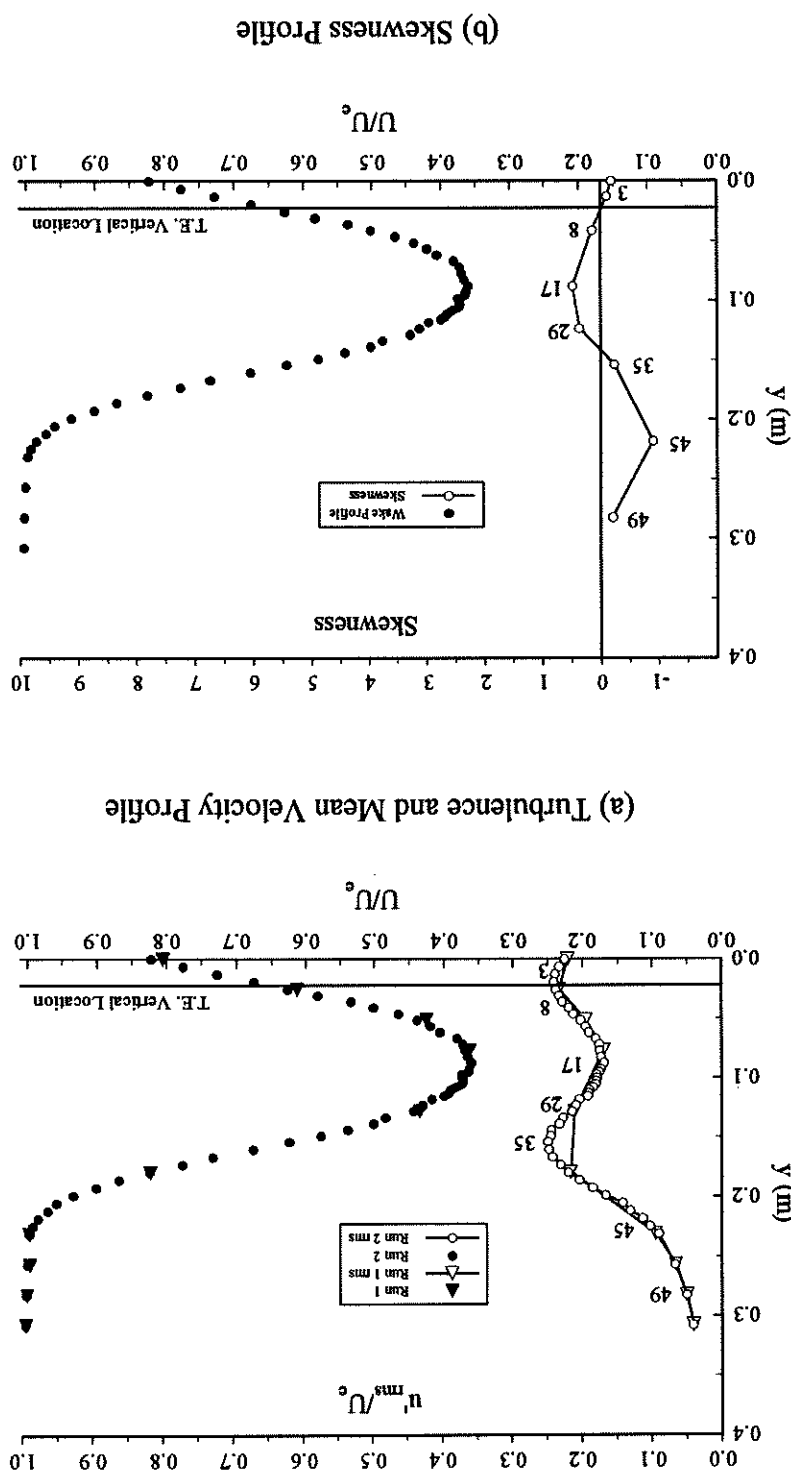


Figure 5.43: Wake Survey Location for  $\alpha = 22^\circ$

Figure 5.44(a) and (b):  $\alpha = 22^\circ$ ;  $Re = 315,000$ ; 0.75C Wake



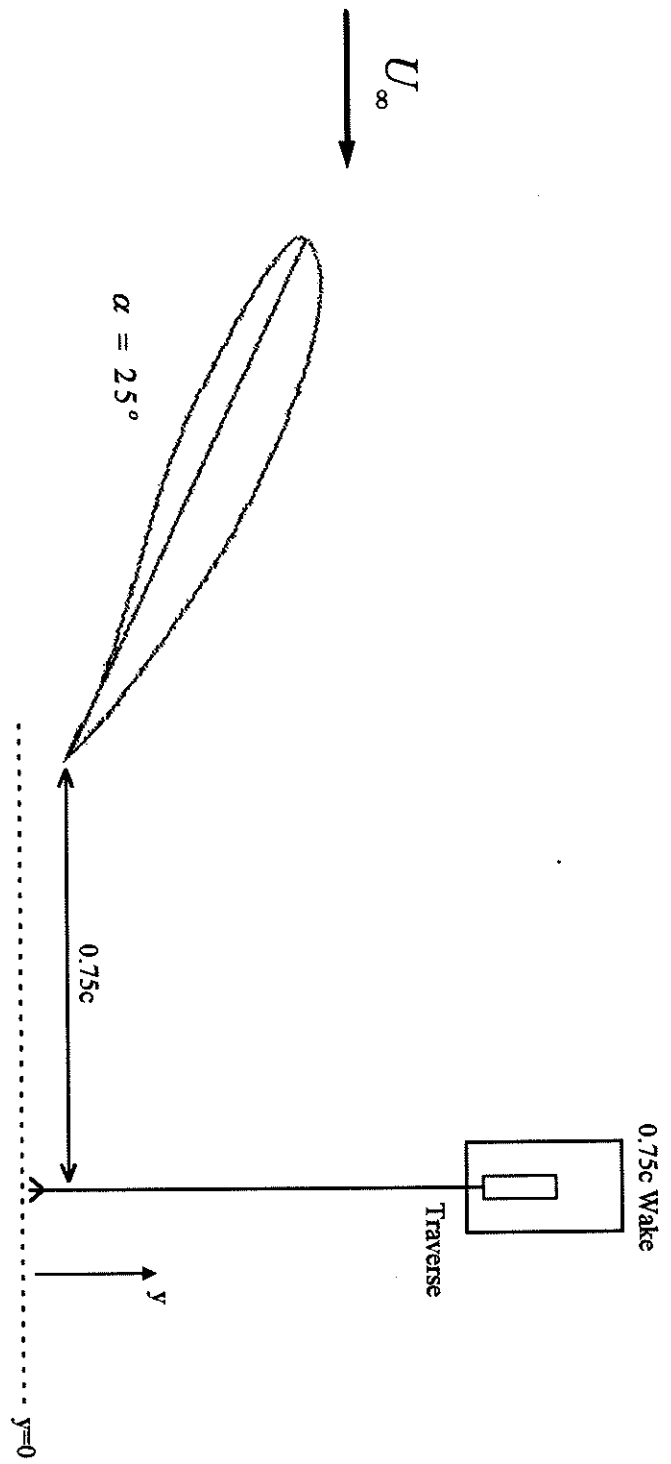
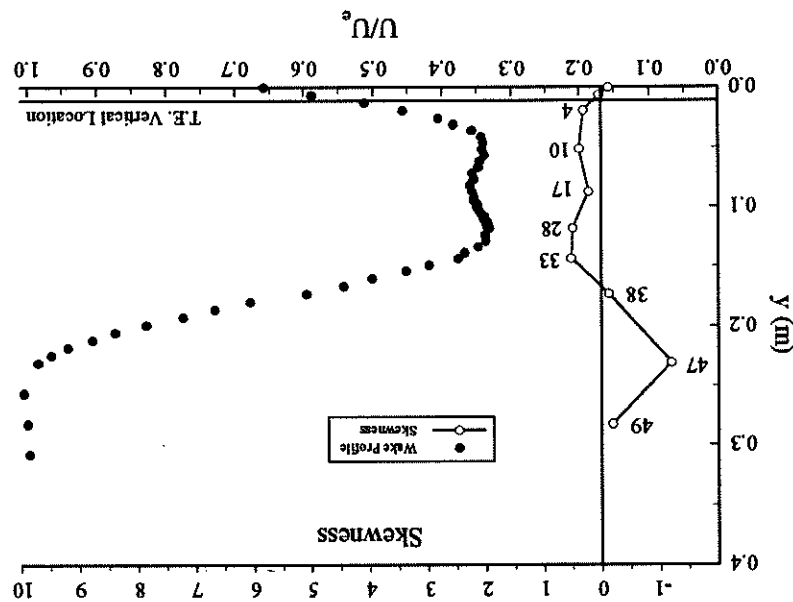


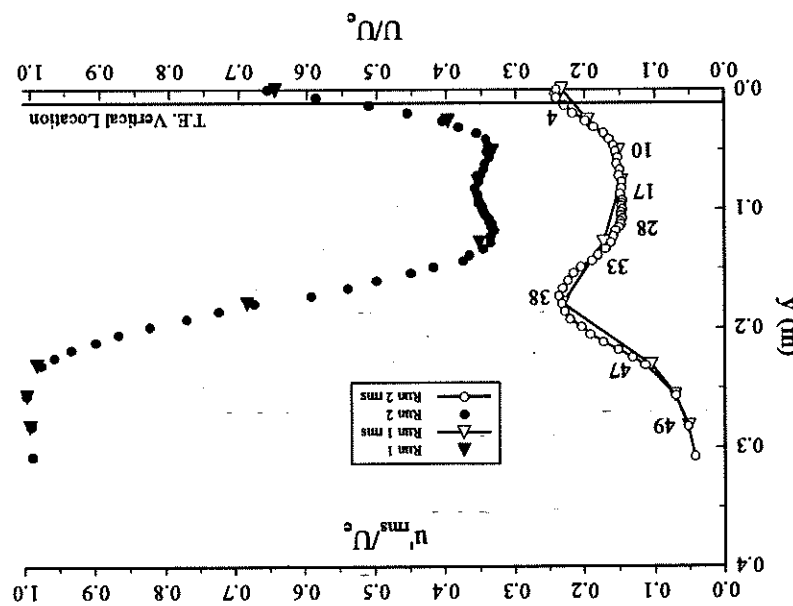
Figure 5.45: Wake Survey Location for  $\alpha = 25^\circ$

Figure 5.46(a) and (b):  $\alpha = 25^\circ$ ;  $Re = 315,000$ ; 0.75C Wake

(b) Skewness Profile



(a) Turbulence and Mean Velocity Profile



are positively skewed between the rms maxima in the two wake high mean shear regions; outside of these regions the velocity fluctuations are negatively skewed. A dominant instability frequency of 27 Hz is best observed when the frequency spectra is computed at points 4 and 38 in the high mean shear regions, with the position in the lower half of the wake yielding the tallest spectral peak. The dominant instability is also seen as smaller fluctuations in the wake profiles was positive between the two  $U_{ms}/U$ . Local maxima that exist in the regions of high mean shear on both sides of the wake. The skewness was consistent for all tests in the post-stalled regime, the skewness of the velocity yielded no indication of a dominant flow instability.

Consistent for all tests in the post-stalled regime, the skewness of the velocity fluctuations in the wake profiles was positive between the two  $U_{ms}/U$ . Local maxima that exist in the regions of high mean shear on both sides of the wake. The skewness was negative outside of that peak-to-peak  $U_{ms}/U$ , region. For the pre-stalled angle tested (a = 15°), the skewness was negative throughout the wake (Figure 5.30b). This change in rotating counterclockwise emanates from the trailing edge (refer back to Figure 5.14). At both edges of the wake where the shear layer meets the free stream, the x-direction velocity component of the coherent vortices caused by their rotation is in the free stream direction. Between the points of maximum  $U_{ms}/U$ , in the mean shear regions, the two counter-rotating coherent vortices have an x-direction velocity component caused by their directions due to the rotation of the coherent vortical structures create skewed fluctuation velocity signals throughout the wake. It is not completely understood at this time why the negative skewness in the wake is positive between the  $U_{ms}/U$ , maximum points and velocity signals throughout the wake.

For the current study negative skewness outside of those rms maxima instead of being vice-versa. For the current study negative skewness outside of those rms maxima instead of being vice-versa. For the current study negative skewness in the wake is positive between the  $U_{ms}/U$ , maximum points and velocity signals throughout the wake. These two different vortical structures create skewed fluctuation velocity signals throughout the wake. It is not completely understood at this time why the negative skewness in the wake is positive between the  $U_{ms}/U$ , maximum points and velocity signals throughout the wake.

Both edges of the wake where the shear layer meets the free stream, the x-direction velocity component of the coherent vortices caused by their rotation is in the free stream direction. Between the points of maximum  $U_{ms}/U$ , in the mean shear regions, the two counter-rotating coherent vortices have an x-direction velocity component caused by their directions due to the rotation of the coherent vortical structures create skewed fluctuation velocity signals throughout the wake.

At both edges of the wake where the shear layer meets the free stream, the x-direction velocity component of the coherent vortices caused by their rotation is in the free stream direction. Between the points of maximum  $U_{ms}/U$ , in the mean shear regions, the two counter-rotating coherent vortices have an x-direction velocity component caused by their directions due to the rotation of the coherent vortical structures create skewed fluctuation velocity signals throughout the wake.

Both edges of the wake where the shear layer meets the free stream, the x-direction velocity component of the coherent vortices caused by their rotation is in the free stream direction. Between the points of maximum  $U_{ms}/U$ , in the mean shear regions, the two counter-rotating coherent vortices have an x-direction velocity component caused by their directions due to the rotation of the coherent vortical structures create skewed fluctuation velocity signals throughout the wake.

Both edges of the wake where the shear layer meets the free stream, the x-direction velocity component of the coherent vortices caused by their rotation is in the free stream direction. Between the points of maximum  $U_{ms}/U$ , in the mean shear regions, the two counter-rotating coherent vortices have an x-direction velocity component caused by their directions due to the rotation of the coherent vortical structures create skewed fluctuation velocity signals throughout the wake.

Both edges of the wake where the shear layer meets the free stream, the x-direction velocity component of the coherent vortices caused by their rotation is in the free stream direction. Between the points of maximum  $U_{ms}/U$ , in the mean shear regions, the two counter-rotating coherent vortices have an x-direction velocity component caused by their directions due to the rotation of the coherent vortical structures create skewed fluctuation velocity signals throughout the wake.

Both edges of the wake where the shear layer meets the free stream, the x-direction velocity component of the coherent vortices caused by their rotation is in the free stream direction. Between the points of maximum  $U_{ms}/U$ , in the mean shear regions, the two counter-rotating coherent vortices have an x-direction velocity component caused by their directions due to the rotation of the coherent vortical structures create skewed fluctuation velocity signals throughout the wake.

Both edges of the wake where the shear layer meets the free stream, the x-direction velocity component of the coherent vortices caused by their rotation is in the free stream direction. Between the points of maximum  $U_{ms}/U$ , in the mean shear regions, the two counter-rotating coherent vortices have an x-direction velocity component caused by their directions due to the rotation of the coherent vortical structures create skewed fluctuation velocity signals throughout the wake.

Both edges of the wake where the shear layer meets the free stream, the x-direction velocity component of the coherent vortices caused by their rotation is in the free stream direction. Between the points of maximum  $U_{ms}/U$ , in the mean shear regions, the two counter-rotating coherent vortices have an x-direction velocity component caused by their directions due to the rotation of the coherent vortical structures create skewed fluctuation velocity signals throughout the wake.

Both edges of the wake where the shear layer meets the free stream, the x-direction velocity component of the coherent vortices caused by their rotation is in the free stream direction. Between the points of maximum  $U_{ms}/U$ , in the mean shear regions, the two counter-rotating coherent vortices have an x-direction velocity component caused by their directions due to the rotation of the coherent vortical structures create skewed fluctuation velocity signals throughout the wake.

Both edges of the wake where the shear layer meets the free stream, the x-direction velocity component of the coherent vortices caused by their rotation is in the free stream direction. Between the points of maximum  $U_{ms}/U$ , in the mean shear regions, the two counter-rotating coherent vortices have an x-direction velocity component caused by their directions due to the rotation of the coherent vortical structures create skewed fluctuation velocity signals throughout the wake.

Both edges of the wake where the shear layer meets the free stream, the x-direction velocity component of the coherent vortices caused by their rotation is in the free stream direction. Between the points of maximum  $U_{ms}/U$ , in the mean shear regions, the two counter-rotating coherent vortices have an x-direction velocity component caused by their directions due to the rotation of the coherent vortical structures create skewed fluctuation velocity signals throughout the wake.

Figure 5.48: Modified Strouhal Number as Function of Alpha

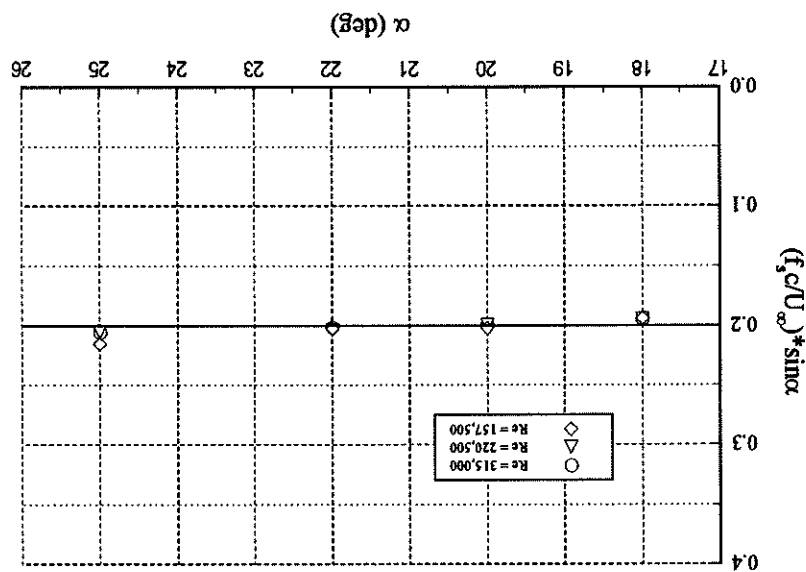
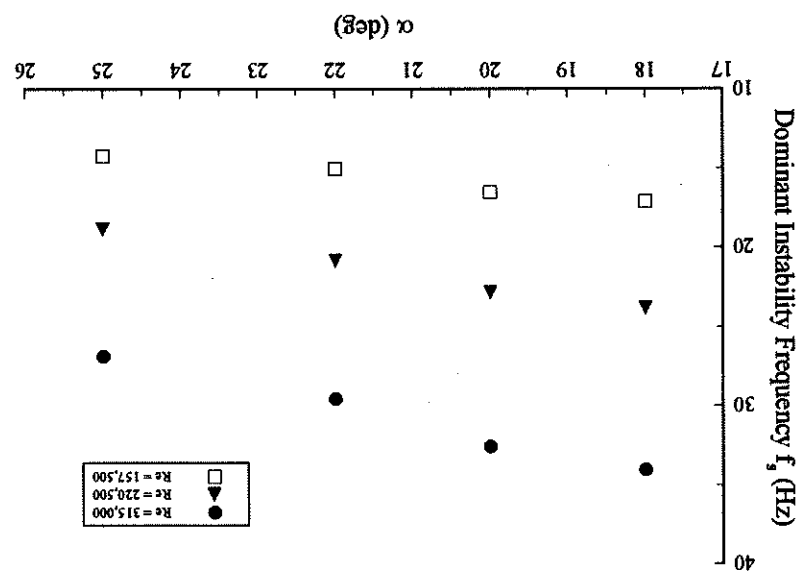


Figure 5.47: Dominant Instability Frequency as Function of Alpha



structures having been found through examination of velocity fluctuation spectra. Structures in the turbulent shear layers of the wake, the dominant frequency of these flow structures having been found through examination of velocity fluctuation spectra. Measured dominant flow instability frequencies for various angles of attack are presented in Figure 5.47 for three different Reynolds numbers. As expected, for a given Reynolds number the dominant instability frequency decreases with increasing angle of attack. For a given angle of attack, the dominant instability frequency increases with Reynolds number. When the dominant instability frequency is nondimensionalized as a modified Strouhal number,  $St_{\text{mod}} = \frac{U}{f_s c} \sin \alpha$ , a constant value of approximately 0.20 is perhaps be made for these results to the vortex shedding phenomenon from a cylinder in experiments are presented with the current findings in Table 5.3. An analogy can be made for the free stream length of which is also approximately 0.20 for a wide range of crossflow, the Strouhal number of which is the cross-stream length of the cylinder. The diameter, the cross-stream length of the free stream that is obstructed by the cylinder. The Reynolds numbers. The length scale used in the stalled airfoil Strouhal calculation is  $c \cdot \sin \alpha$ , the cross-stream length scale used in the free stream that is obstructed by the airfoil. It is interesting that different low-speed airfoils at different stalled angles of attack and different Reynolds numbers all create dominant coherent vortical structures at frequencies that can be nondimensionalized (using as the length scale the cross-stream obstructed length of the free stream) to give the same result as for vortex shedding from a cylinder in crossflow.

Velocity skewness profiles had distinct characteristics for pre-stalled and post-stalled angles of attack tested ( $\alpha = 18^\circ, 20^\circ, 22^\circ$ , and  $25^\circ$ ). The rms profiles of the streamwise velocity fluctuations revealed, as expected, a maximum fluctuation level peak in the region of high shear of the mean velocity and wake maximum fluctuation level peak in the lower half of the wake consistently occurred directly downstream from the airfoil's trailing edge when the airfoil was stalled. Maximum rms levels in the wake of the airfoil were of order 0.10 when nondimensionalized by  $U_\infty$ . for the pre-stalled angle of attack tested ( $\alpha = 15^\circ$ ) and of order 0.25 for the post-stalled tests. After stall, the skewness pattern changed. The skewness was positive in the wake between the two rms fluctuation peaks and negative outside of that peak-to-peak region. This skewness pattern is related to the post-stalled formation of counter-rotating coherent vortex structures that dominate the mixing in the turbulent free shear layers. With flow tests. A profile with all negative values was measured for the pre-stalled angle of attack tests. A profile with all positive values was measured for the post-stalled angle of attack tests. After stall, the skewness pattern changed. The skewness was positive in the wake between the two rms fluctuation peaks and negative outside of that peak-to-peak region.

The rms profiles of the streamwise velocity fluctuations revealed, as expected, a maximum fluctuation level peak in the region of high shear of the mean velocity and wake maximum fluctuation level peak in the lower half of the wake consistently occurred directly downstream from the airfoil's trailing edge when the airfoil was stalled. Maximum rms levels in the wake of the airfoil were of order 0.10 when nondimensionalized by  $U_\infty$ . for the pre-stalled angle of attack tested ( $\alpha = 15^\circ$ ) and of order 0.25 for the post-stalled tests. After stall, the skewness pattern changed. The skewness was positive in the wake between the two rms fluctuation peaks and negative outside of that peak-to-peak region.

### 5.2.7 Conclusions from Hot-Wire Flowfield Measurements

Experimenter	Airfoil Tested	$Re$	$St_{sin \alpha}$	$\alpha$	Current Work	SM701	315,000	0.20	$18^\circ, 20^\circ, 22^\circ, 25^\circ$
Zaman and McKinzie, 1988	LRN-(1)-1007	$40,000 < Re < 140,000$	0.2	$18^\circ, 20^\circ$	Hsiao et al., 1994	NACA 63-018	310,000	$0.17 - 0.19$	$24^\circ < \alpha < 35^\circ$
Hsiao et al., 1989	NACA 63-018	$6,300 < Re < 500,000$	$\approx 0.2$	$24^\circ$	Zaman and McKinzie, 1988	LRN-(1)-1007	$40,000 < Re < 140,000$	0.2	$18^\circ, 20^\circ$
Huang et al., 1987	18% thick symmetric airfoil	35,000	0.19	$20^\circ$	Hsiao et al., 1994	NACA 63-018	310,000	$0.17 - 0.19$	$24^\circ < \alpha < 35^\circ$

Table 5.3:  $St_{sin \alpha}$  Results for Various High-Angle-of-Attack Airfoil Experiments

forms due to the upper surface separation and a counter-clockwise vertical structure forms due to the trailing edge separation.

The frequencies of these coherent vortical structures originating during stall from the upper surface separation and the trailing edge separation were found to be the same. This dominant frequency scales with the free stream velocity such that the modified Strouhal number equals 0.20 for all angles of attack and all Reynolds numbers tested in the stalled regime. This result is consistent with the work of other researchers as seen in Table 5.3.

The best streamwise position at which to measure the dominant frequency of the wake is the trailing edge (the farthest downstream location that was studied). A dominant airfoil's trailing edge (the farthest downstream location that was studied). A dominant instability was not seen in velocity profiles on the airfoil. A dominant flow instability frequency surfaced, however, at the first wake survey location (25% chord behind the trailing edge) which grew more coherent as the wake developed.

Within a wake survey profile, the dominant instability was most clearly measured between the free stream and the peak  $u_{ms}/U$ . Location that occurred in the middle of the mean shear regions on both sides of the wake. These regions are where the entrainment of the free stream is occurring. A dominant instability was not seen in the wake's maximum velocity deficit region. Consistent for all tests at stalled angle of attack, this region of no dominant instability frequency was between the two peak  $u_{ms}/U$ . Locations in the regions of high mean shear which exist on both sides of the wake. This "quiet" region in the middle of the wake indicates that the coherent vortical structures are confined to the turbulent separated shear layers. Figure 5.49 summarizes some of these conclusions.

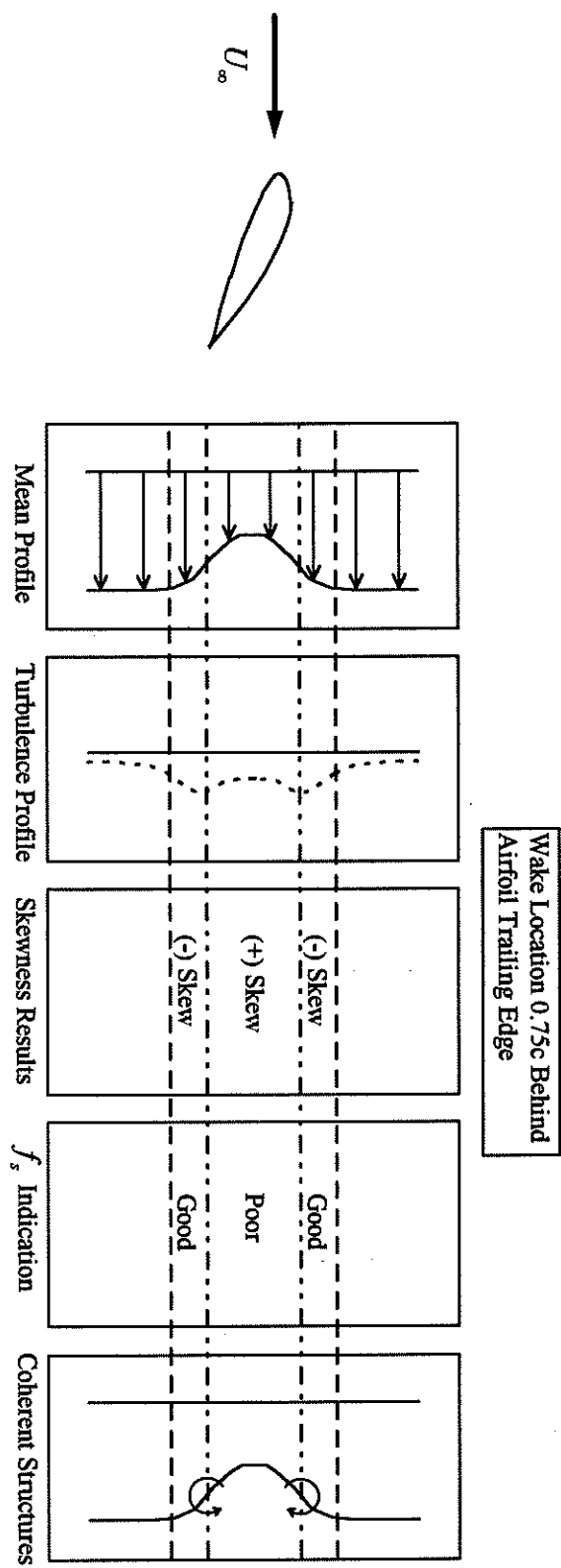


Figure 5.49: Summary of Important Hot-Wire Experimentation Conclusions

The beta phase polymer is then exposed to very high electric fields to align the crystallites molecules into parallel crystal planes. This state of the material is called the "beta phase." It is stretched to approximately 1/5 of its extruded thickness causing chain packing of the begins with a melt extrusion of PVD film pellets into sheet form. The sheet is then manufactured by AMP, Incorporated was used in this study. The manufacturing process piezoelectric films, as their name implies, also exhibit piezoelectric properties. PVD film Jacques Cuné first observed the piezoelectric phenomenon in natural quartz crystals. to produce electrical signals when mechanically deformed" (Chatigny, 1984). Pierre and materials to change their dimensions when subjected to an electrical field or, conversely, Piezoelectricity, meaning "pressure electricity," is "the capability of certain crystalline

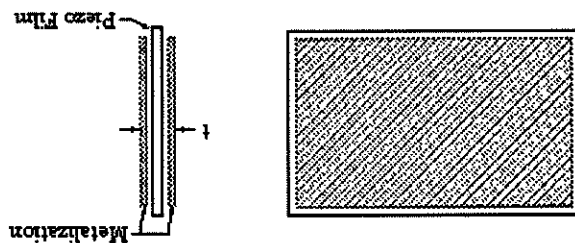
## 6.1 Background on Piezoelectric Materials

using piezoelectric films as a means to control a separated shear layer. results of this very brief study are by no means conclusive, they do reveal difficulties in surface as well as the absence of sliding parts in a piezoelectric film actuator. While actuator include the relatively non-intrusive nature of the very thin film on an airfoil's mixing rate of the separated shear layer. Advantages of using a piezoelectric film as an piezoelectric film was examined as an active control actuator that would enhance the (Whitehead et al., 1996). The angle of stall was increased slightly. For the current work, transition by small surface vibrations on a Clark-Y and a NACA 64-412 airfoil used a compressible dielectric electrostatic film transducer to also promote early early transition; the flow thus was energized and remained attached longer. Whitehead et (Kobayakawa et al., 1992) using such piezoelectric film on an airfoil's surface to promote active control actuator. Section 5.0.4 contained a description of experiments examination of the effectiveness of piezoelectric polyvinylidene fluoride (PVDF) film as an understood, an effort can be made to control the separation. This section describes a brief Now that the physics of the separated flow region of the SM701 airfoil is better

## 6 SIMPLE ACTIVE CONTROL TEST USING PIEZOELECTRIC FOIL

Figure 6.1: Piezoelectric Film

Source: AMP Incorporated, 1993



mode.

Figure 6.2. With this attachment method, the film would operate primarily in its thickness was attached at the midspan using Graftix 2 Sided Adhesive Double Tape as shown in given in Figure 6.1. The film had sputtered nickel copper alloy conductive surfaces and leading edge of the SM701 model in the ASWT. A sketch of the piezoelectric film is A 28  $\mu\text{m}$  thick PVDF film with dimensions of  $5 \times 7.5$  inches was attached to the

## 6.2 The Experiment

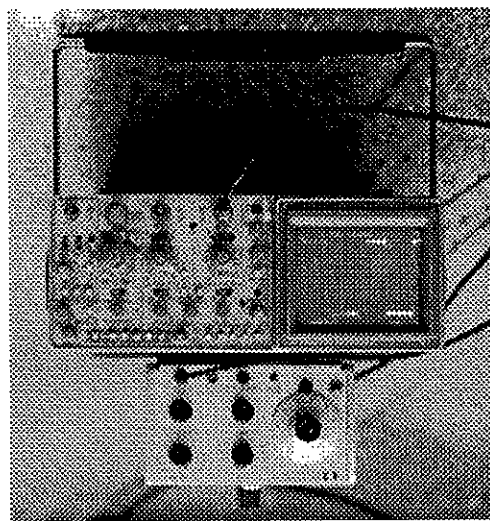
name a few applications.

PVDF film is very thin (order of  $1\mu\text{m}$ ), flexible, inert, and can withstand several thousand volts before breaking down. It has been used in pressure switches, acoustic transducers, high-fidelity tweeters, roadway counters, sports timers, and novelty items, to decrease in thickness or decreases in length and width while increasing in thickness. When voltage is applied to the piezo film, the film extends or contracts along the axis of stretching during its fabrication. The film increases in length and width while appears between the electrodes.

When the piezo film is deformed, a change in the surface charge density of the material occurs due to the piezoelectric effect. The electrodes collect the charge so that a voltage

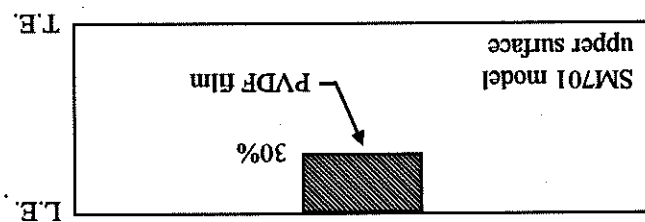
relative to the polling field. Finally, electrodes are applied to the piezo film surfaces (AMP Incorporated, 1993).

Figure 6.3: The Function Generator with Digital Oscilloscope



The film wrapped around the leading edge to the lower surface of the model where 32 test section of the ASWT and were connected to the output of a Hewlett Packard 3310B function generator. The output of the function generator was also sent to a Tektronix 2230 100MHz digital storage oscilloscope so that the generated signal could be viewed and its frequency set accurately. The function generator and the oscilloscope can be seen in Figure 6.3. For all control tests, a 30 Volt peak-to-peak (30 V p-p) square wave was used as the excitation signal. The rest of the experimental setup mirrored the setup as described in Section 5.2.2 for the hot-wire flowfield measurements. The angle of attack was set to  $20^\circ$ , and a Reynolds number of 315,000 was studied.

Figure 6.2: Attachment Location of PVDF Film Element on Model Upper Surface



The hot-wire sensor was positioned at point 37 (see Figure 5.41a of Section 5.2.6) in the wake 0.75c from the model's trailing edge. Under natural conditions, a modified Strouhal number of 0.20 (based on the dominant flow instability frequency) was measured from the airfoil wake approximately 28 Hz which led to a modified Strouhal number of 0.17. It appears that the mere presence of the film element on the model may be having an effect on the flow. The PVD film was then excited at frequencies of 14, 28, 56, 280, 560, and 2800 Hz. These values were chosen based on others' past work in active control of separated shear layers. The mean and rms fluctuation velocities as measured by the hot-wire sensor at its fixed location did not noticeably change under these different excitation frequencies. In addition, the power spectra of the velocity fluctuations under these different control frequencies did not vary noticeably. In short, no noticeable effect was observed at the single sensor hot-wire position in the wake when the PVD foil was oscillated.

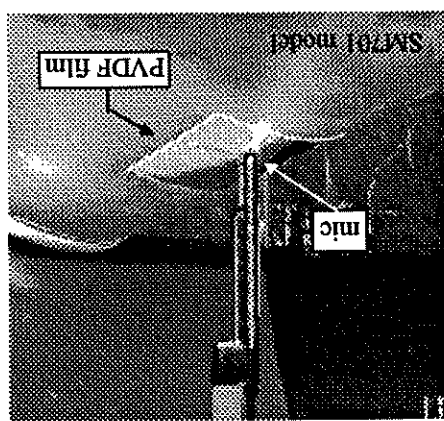
A possible explanation as to why no effect was observed when control was applied is that neither of the two main methods can be successful in controlling a separated airfoil. The first method is by using acoustic waves to generate induced normal velocity fluctuations at the airfoil surface near the separation point. Acoustic tunnelling resonance usually plays a role in this form of active control. The second method of controlling the separated shear layer is by providing a hydrodynamic disturbance, i.e. by controlling the shear layer is by introducing normal velocity fluctuations at the airfoil surface near the separation location. It is believed that neither of these methods (acoustically induced or directly introduced velocity fluctuations) are realistic options with the piezoelectric film as tested for this work.

The microphone was connected to a Larson-Davis 2200C Preamp/P.S., and the output positioned 0.125 inch above the film in the test section of the ASWT. See Figure 6.4. Tests were performed to determine the sound pressure level (SPL) of the PVD control element on the model surface. A Larson-Davis  $\frac{1}{4}$  inch condenser microphone was positioned on the model surface. The microphone was connected to a Larson-Davis 2200C Preamp/P.S., and the output positioned 0.125 inch above the film in the test section of the ASWT. See Figure 6.4. The microphone was connected to a Larson-Davis 2200C Preamp/P.S., and the output positioned 0.125 inch above the film in the test section of the ASWT. See Figure 6.4. The microphone was connected to a Larson-Davis 2200C Preamp/P.S., and the output positioned 0.125 inch above the film in the test section of the ASWT. See Figure 6.4.

The element was then excited at 2000 Hz with the spectrum analyzer showing a peak approximately 52 dB at the 1750 Hz energy peak. The SPL at the 2000 Hz peak was approximately 62 dB. This value was 42 dB above the background noise at 2000 Hz. The element thus seems to be responding much better to a high frequency input signal; however, to realize effective active control of the separated shear layer it is believed that the excitation frequency needs to be on the order of 30 Hz corresponding to the dominant natural flow instability frequency.

The control element was then excited at 30 Hz. The spectrum analyzer could not detect any difference from the background room noise. The PVD element was then excited at 250 Hz. The spectrum analyzer revealed energy peaks at approximately 1250 Hz, 1750 Hz, 2750 Hz, and at other higher harmonics. No noticeable energy peak was seen at the applied excitation frequency of 250 Hz. The element, due to its physical composition and geometry, is preferring to vibrate at the higher harmonics. The measured SPL was approximately 52 dB at the 1750 Hz energy peak.

Figure 6.4: The Microphone Above the PVD Element



signal was sent to a Hewlett Packard 35660A Dynamic Signal Analyzer. The microphone had been calibrated with a Larson-Davis pistophone producing a 250 Hz tone at 114.0 dB SPL prior to installation into the test section.

measured in the near or in the far field of the given acoustic source. The PVD<sub>F</sub> element can also act as a hydrodynamic disturbance source in that its vibration caused by the applied square wave electrical signal can directly create velocity fluctuations. However, based on deformation formulas provided by AMP Incorporated, the expected normal oscillation of the PVD<sub>F</sub> element (thickness mode) caused by the 30 V p-p square wave is around 0.001  $\mu\text{m}$ . This extremely small deformation is not expected to produce velocity fluctuations that are capable of interacting with the separated shear layer. Whitehead et al. present a similar view stating, "...none of the commercially available thin film transducers are capable of efficiently introducing substantial motion into the boundary layer air flow" (Whitehead et al., 1996). Chang et al. used maximum velocity fluctuations on the order of 10 m/s (induced by sound through a slot in a NACA 63-018 airfoil) to achieve flow reattachment (Chang et al., 1992). Their SPL level was roughly 120 dB. It is not expected that the piezoelectric foil as tested can produce either the velocity fluctuation level or the SPL that Chang et al. achieved.

Recapping, from the brief experimentation performed, the piezoelectric film element does not seem practical as an active control actuator for exciting a separated shear layer. The PVD<sub>F</sub> film does not seem to be generating an adequate SPL based on other experiments' work to acoustically induce the necessary normal velocity perturbations. Also, the PVD<sub>F</sub> element does not appear to vibrate normal to the airfoil surface with large enough amplitude to directly introduce the required velocity perturbations. PVD<sub>F</sub> films may possibly be used to promote early transition and thus delay separation; however, after separation occurs it does not seem that PVD<sub>F</sub> film actuators can be readily used to enhance the mixing in the separated shear layer thus causing flow reattachment to occur.

As a result of this study of the separated flow characteristics of the SM701 airfoil at high angle of attack and low Reynolds number, much insight has been gained into the nature of the coherent structures that dominate the separated flow region. Now that these dominant flow structures are better understood for a wide range of operating conditions (Reynolds numbers and angles of attack), future work can begin on actively enhancing (Reynolds numbers and angles of attack) these natural structures in an attempt to reduce the separated flow region.

The heat transfer study that was performed showed consistent results with a conventional fluorescent oil flow visualization study. By using both oil flow visualization and a heat transfer method, the viscous flow regions existing on the airfoil at various Reynolds numbers and angles of attack were revealed. The heat transfer method complemented the oil flow visualization method in revealing flow structures not captured by the qualitative oil flow visualization method. These details of the viscous flow at the airfoil's surface include a flow relaxation region when the laminar separation regions when the airfoil was stalled. This enhanced heat transfer trend in the turbulent reattachment method revealed an increasing heat transfer trend in the turbulent trailing edge in the separated region when the airfoil was stalled. This enhanced heat transfer near the separated regions when the airfoil was stalled. In addition, the laminar separation bubble was seen with the shear stress gauges. In addition, the level of turbulent fluctuations near the airfoil's surface was seen to increase near the trailing edge in the separated flow region when the airfoil was stalled. This increased turbulent fluctuation bubble was seen with the shear stress gauges. In addition, the level of turbulent fluctuations near the airfoil's surface was seen to increase near the trailing edge in the separated flow region when the airfoil was stalled. The flow relaxation region after the reattachment of the laminar heat transfer study. The flow relaxation region after the reattachment of the laminar heat transfer study that was undertaken gave results consistent with the

The qualitative shear stress study that was undertaken gave results consistent with the causal enhancement of heat transfer. Entrained free stream fluid is sent upstream and impinges near the trailing edge, thus caused by the counter-rotating coherent vortical structures that are shed from the airfoil. Separated by the trailing edge in the turbulent separated region when the airfoil was stalled is believed to be the laminar separation regions when the airfoil was stalled. This enhanced heat transfer near the separated regions when the airfoil was stalled. In addition, the laminar separation bubble at the airfoil's surface include a flow relaxation region when the laminar separation bubble by the qualitative oil flow visualization method. These details of the viscous flow at the airfoil's surface include a flow relaxation region when the laminar separation regions when the airfoil was stalled. This enhanced heat transfer trend in the turbulent reattachment method revealed an increasing heat transfer trend in the turbulent trailing edge in the separated region when the airfoil was stalled. This enhanced heat transfer near the separated regions when the airfoil was stalled. In addition, the laminar separation bubble was seen with the shear stress gauges. In addition, the level of turbulent fluctuations near the airfoil's surface was seen to increase near the trailing edge in the separated flow region when the airfoil was stalled. The flow relaxation region after the reattachment of the laminar heat transfer study. The flow relaxation region after the reattachment of the laminar heat transfer study that was undertaken gave results consistent with the

The heat transfer study that was performed showed consistent results with a conventional fluorescent oil flow visualization study. By using both oil flow visualization and a heat transfer method, the viscous flow regions existing on the airfoil at various Reynolds numbers and angles of attack were revealed. The heat transfer method complemented the oil flow visualization method in revealing flow structures not captured by the qualitative oil flow visualization method. These details of the viscous flow at the airfoil's surface include a flow relaxation region when the laminar separation regions when the airfoil was stalled. This enhanced heat transfer trend in the turbulent reattachment method revealed an increasing heat transfer trend in the turbulent trailing edge in the separated region when the airfoil was stalled. This enhanced heat transfer near the separated regions when the airfoil was stalled. In addition, the laminar separation bubble was seen with the shear stress gauges. In addition, the level of turbulent fluctuations near the airfoil's surface was seen to increase near the trailing edge in the separated flow region when the airfoil was stalled. The flow relaxation region after the reattachment of the laminar heat transfer study. The flow relaxation region after the reattachment of the laminar heat transfer study that was undertaken gave results consistent with the

## 7 CONCLUSIONS

structures in the separated flow region. These dominant structures exist in the turbulent separated shear layers while the shear stress gauges were located on the airfoil's surface. The flow recirculating region existing between the dominant coherent structures of the separated shear layers made the shear stresses on the airfoil's surface effectively invisible to the flow structures.

Hot-wire anemometry tests revealed dominant frequencies of coherent vortical structures in the separated shear layers when the airfoil was stalled. These dominant frequencies scaled with the free stream velocity such that the modified Strouhal number for all Reynolds numbers and post-stall angles of attack tested was approximately 0.20. The dominant coherent structures were best detected in the wake after they had a chance to develop over the airfoil. In a given wake profile, the dominant structures were best sensed with the hot-wire in the region between the free stream and the point of maximum skewness of the velocity fluctuations in the wake. The wake was also examined and the wake. Skewness of the velocity fluctuations in the wake was also examined and confirmed the existence of these dominant flow structures.

Enough information is now known on the post-stall flow behavior of the SM701 airfoil to begin a detailed active flow control study. A preliminary study using PVD<sub>F</sub> films as control actuators revealed difficulties involving SPL and vibration displacement levels of the films. Despite the current difficulties, active control has been shown by past experiments to be an attainable goal in fluid mechanics. Various methods have been employed, working with both laminar separation and turbulent separating flow regions.

practical in real-world applications.

The challenge that lies ahead is to take active control out of the laboratory and make it employable, working with both laminar separation and turbulent separating flow regions. The challenge that lies ahead is to take active control out of the laboratory and make it employable, working with both laminar separation and turbulent separating flow regions.

198

- Pieces were used to temporarily solve the problem for the current work.
- Redesign the traverse mount to eliminate vibration tendency. (Wooden reinforcement

### *Hot-Wire Flowfield Measurements*

- Reverse flow regions could then be better documented.
- Use both legs of the McCroskey sensor so that flow directionality can be sensed.

### *Qualitative Shear Stress Tests*

- Knowing  $t_{wall}$  and  $k_{wall}$  more accurately will lower the uncertainty in  $h$ .
- Use a model with more uniform wall thickness and built out of a uniform material.

- longer transients during calibration and thus more accurate calibrations.
- composition and less irregularities than the wing material. Using Plexiglas should yield piece is made out of the wing material composite. Plexiglas has a more isotropic
- Build a new liquid crystal calibration piece out of Plexiglas. The current calibration

- acceptable with this decreased heater strip width.
- dimensional color band width on the heater strip during experimentation should still be resistance to raise, thus lowering the overall uncertainty in  $h$  slightly. The two-
- Use a heater strip width of 2.5 inches. This reduced width will cause the heater strip

### *Liquid Crystal Thermography*

- too large to test in the ASWT.
- greatly influenced by the tunnel walls for tests in the ASWT. A 12 inch chord model is work be done in the LS TT only. The flow about the 12 inch chord airfoil tested was should help future experimentation go more smoothly. It is recommended that all future given in this section. These suggestions come from the work that has been done and suggestions regarding future experimentation in the areas explored for this thesis are

## 8 SUGGESTIONS FOR FUTURE WORK

- Use larger square wave amplitude to increase the film's displacements and SPL.
- Operate the film in its elongation mode (where deformations take place in the film and repeated use leading to lesser film displacements. The nickel copper conductive surfaces are more brittle and crack with high voltages conductive surfaces can take high voltages and repeated use without deterioration. Instead of in its thickness mode. The thickness mode is more suited for plane) instead of in its thickness mode. The thickness mode is more suited for ultrasound applications. The maximum transmission occurs at  $\frac{1}{2}$  wavelength resonance in the thickness mode, which for 28  $\mu\text{m}$  film is approximately 40 MHz. A film over 1 mm thick would be required to bring this value down to the low MHz range. In the elongation mode, lower frequencies and larger displacements can be achieved (on the order of 10's of  $\mu\text{m}$ ). However, to operate in elongation mode, the entire film could not be secured to the wing surface as was done in the thickness mode application (perhaps only 2 edges). Wind blowing over the film would then tend to shake and flutter the loose film leading to the possibility of tearing.

- Use films with silver ink conductive surfaces rather than nickel copper. The silver ink and repeated use leading to lesser film displacements.

## Using PVD

*Active Control*

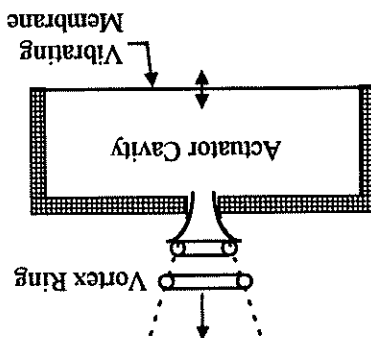
- Use two hot-wire sensors for measurements. One should be located in a region of positive velocity fluctuation skewness, and the second hot-wire should be located in a region of negative velocity fluctuation skewness. Coherence measurements can give more insight into the vortex shedding phenomenon.

- Perform the hot-wire tests that were done in the ASWT in the LS LT to re-determine the modified Strouhal number for vortex shedding from the SM701 model at high angle of attack. The results from the LS LT should be more accurate than the results obtained in the ASWT due to less tunnel blockage effects in the LS LT.

- Recommended that a system using direct introduction of velocity perturbations is first made to work. Then, experiments should be performed that examine what velocity profiles along the chord of the airfoil.

profiles along the chord of the airfoil. showed that the shedding frequency is seen stronger in the wake than in velocity hot-wire can be attached to the wake survey pilot probe traverse since hot-wire tests with hot-wire information to determine the effect of any applied active control. The recommended pressure tapping the model and using  $C_1$ ,  $C_2$ , and  $C_3$ , distribution, along

Figure 8.1: Synthetic Jet Actuator



- Synthetic jets offer an interesting control possibility. A synthetic jet is a push-pull, cavity-generated jet. The net mass flow from the cavity is zero. Thus for synthetic jets no additional fluid needs to be pumped, eliminating the need for tubing systems. A synthetic jet is depicted in Figure 8.1.

- Recommended putting aside PVD foil for now and examining control methods that directly introduce velocity perturbations (as opposed to acoustic methods in which sound induces velocity perturbations).

- Use films with larger surface area on the model to interact with a larger region of the flow.

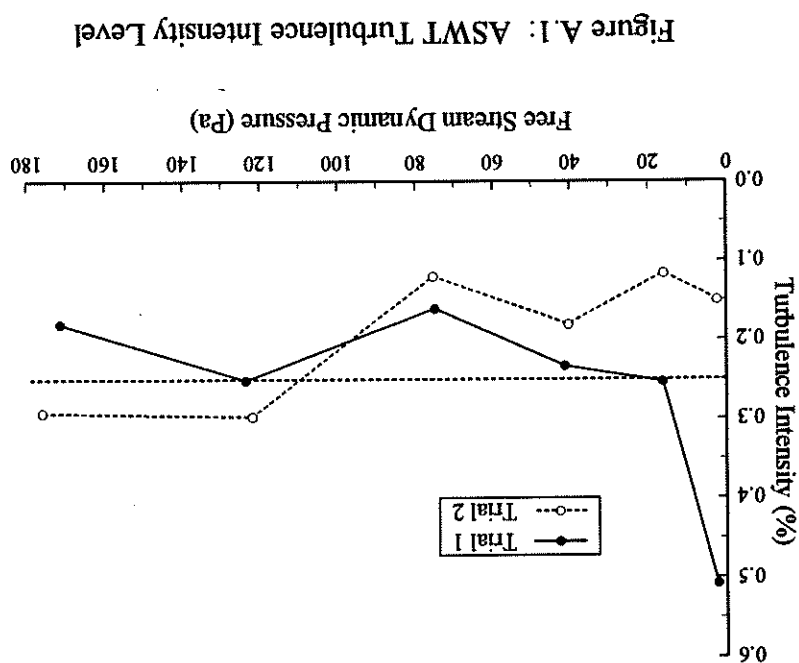
#### General suggestions

will be better seen.

perturbation levels are required to provide control under different experimental conditions. Once insight into the necessary magnitude of the forcing level for effective control is obtained, the feasibility of using PVDF films to create velocity fluctuations will be better seen.

This appendix contains turbulence intensity information for the ASWT.

#### APPENDIX A: ASWT Turbulence Intensity Information



Code Asks For	Answer Given
General output file?	out0.out
Cp output file?	outcp0.out
x,y output file?	outxy0.out
Type of analysis?	(0) Analysis of a given shape
Type of object?	(5) Arbitrary airfoil
Angle of attack?	0.0
Mach number?	0.0
Number of desired panels?	43
Clustering?	0.8
Input file with x/c, y/c airfoil coordinates?	sm701.dat
Include following or subsection?	(0) No

Table B.1: Inputs for panel.f for Angle of Attack = 0 degrees

This appendix contains input information used in the prediction of the convective heat transfer coefficients on the SM701 airfoil. The tables in this appendix are discussed in Chapter 3.0.

## APPENDIX B: Numerical Predictions Input Information

RUN 015 AOA = 0 degrees ReAVG = 310601					
TITLE LINE					
0.000835	0.319148	2.0	290	0.05	0.0090
(EXCLUDES Y=0 PT)	# # DELTAX RETRAN 0.05 ENTRA 0.0	NOTE: VARV DELTAX, RETRAN, ENTRA TO TRY TO OBTAIN BETTER RESULTS 39 = # POINTS ALONG BOUNDARY AT WHICH U(s) IS SPECIFIED	39	1	99492.1 1.174 0.0000183 0.72
0.002581	1.0	0.004579	1.0	0.006990	1.0
0.009964	1.0	0.013642	1.0	0.018131	1.0
0.023525	1.0	0.029905	1.0	0.037319	1.0
0.045785	1.0	0.055297	1.0	0.065821	1.0
0.077296	1.0	0.089636	1.0	0.102735	1.0
0.116466	1.0	0.130685	1.0	0.145237	1.0
0.159959	1.0	0.189232	1.0	0.203451	1.0
0.217183	1.0	0.242623	1.0	0.254098	1.0
0.274136	1.0	0.282606	1.0	0.290024	1.0
0.296412	1.0	0.301816	1.0	0.306309	1.0
0.312968	1.0	0.309988	1.0	0.315387	1.0
0.317393	1.0	0.319148	1.0	0.319148	1.0
0.322907	0.0	0.328535	0.0	0.328535	0.0
CODE; THIRD COLUMN IS U(s) FROM PANEL	FIRST COLUMN IS U(s) FROM PANEL	11.882699	0.0	11.882699	0.0
14.710274	0.0	14.710274	0.0	14.710274	0.0
16.978252	0.0	16.978252	0.0	16.978252	0.0

Table B.2: STAN5 Input File - SM701 Airfoil,  $\alpha = 0^\circ$ ;  $Re=315000$

18.514802 0.0	304665.8	19.937199 0.0	304665.8	20.980344 0.0	304665.8	21.647628 0.0	304665.8	21.958311 0.0	304665.8	22.041322 0.0	304665.8	22.000875 0.0	304665.8	21.895056 0.0	304665.8	21.636130 0.0	304665.8	21.437016 0.0	304665.8	21.293046 0.0	304665.8	20.951147 0.0	304665.8	20.683146 0.0	304665.8	20.421249 0.0	304665.8	19.613651 0.0	304665.8	19.113549 0.0	304665.8	18.745883 0.0	304665.8	18.374198 0.0	304665.8	18.066007 0.0	304665.8	17.773847 0.0	304665.8	17.496313 0.0	304665.8	17.162097 0.0	304665.8	16.728523 0.0	304665.8	16.166471 0.0	304665.8	15.475848 0.0	304665.8	14.998527 0.0	304665.8	14.690658 0.0	304665.8	14.340861 0.0	304665.8	13.977651 0.0	304665.8	12.515596 0.0	304665.8	0.00000000 0.00000000 304665.8	0.0000261 0.0433922 004458.3	0.0000522 0.0826964 304250.8	0.0000782 0.1180063 304043.4	0.0001043 0.1494606 30385.9	0.0001304 0.1772403 003421.0	0.0001565 0.2015616 303421.0	0.0001826 0.2226668 303213.6	0.0002087 0.2408142 303006.1	0.0002347 0.2562685 302798.7	0.0002608 0.2693042 302591.2	0.0002869 0.2801926 302383.8	0.0003130 0.2891920 302176.3	0.0003391 0.2965575 301968.9	0.0003652 0.3025184 301761.4	0.0003912 0.3072942 301554.0	0.0004173 0.3110754 301346.5	0.0004434 0.3140333 301139.1	0.0004695 0.3163259 300931.6	0.0004956 0.3180793 300724.2	0.0005217 0.3194032 300516.7	0.0005477 0.3211275 300101.8	0.0005738 0.3216603 299894.4	0.0005999 0.3220413 299479.5	0.0006260 0.32220413 299479.5	0.0006521 0.3223158 299479.5
---------------	----------	---------------	----------	---------------	----------	---------------	----------	---------------	----------	---------------	----------	---------------	----------	---------------	----------	---------------	----------	---------------	----------	---------------	----------	---------------	----------	---------------	----------	---------------	----------	---------------	----------	---------------	----------	---------------	----------	---------------	----------	---------------	----------	---------------	----------	---------------	----------	---------------	----------	---------------	----------	---------------	----------	---------------	----------	---------------	----------	---------------	----------	---------------	----------	---------------	----------	---------------	----------	--------------------------------	------------------------------	------------------------------	------------------------------	-----------------------------	------------------------------	------------------------------	------------------------------	------------------------------	------------------------------	------------------------------	------------------------------	------------------------------	------------------------------	------------------------------	------------------------------	------------------------------	------------------------------	------------------------------	------------------------------	------------------------------	------------------------------	------------------------------	------------------------------	-------------------------------	------------------------------

0.0006781 0.3225063 299272.0	0.0007042 0.3226387 299064.6	0.0007303 0.3227291 298857.1	0.0007564 0.3227905 298649.7	0.0007825 0.3228325 298442.2	0.0008086 0.3228583 298234.8	0.0008346 0.3228777 298027.3	0.0008607 0.3228874 297819.9	0.0009129 0.3229003 297405.0	0.0009390 0.3229035 297197.5	0.0009651 0.3229035 296990.1	0.0009911 0.3229035 296782.6	0.0010172 0.3229070 296575.2	0.00000 0.3229000 296197.4	0.41 0.085 0.01 0.22 0.38 1.0 0.0 MATCHES FIRST U(g) VALUE	25.0 1.0 1.0 1.0 0.86 4000.0 0.86 MAKE SURE LAST U(g) VALUE	1 21 2
------------------------------	------------------------------	------------------------------	------------------------------	------------------------------	------------------------------	------------------------------	------------------------------	------------------------------	------------------------------	------------------------------	------------------------------	------------------------------	----------------------------	--	---	--------

```

*****  

* This appendix contains the FORTRAN codes that were used for data acquisition and  

* data reduction throughout the LS/TT heat transfer experiments. The codes are well-  

* commented.  

*****  

* This program is the Data Acquisition code for my liquid crystal  

* work at APB. It samples the venturi voltage, the income  

* voltage, and the 9 thermocouple voltages. The code is  

* completely menu driven, so just run it and it will be self-  

* explanatory.  

*  

* integer*2 sch,fch,nsapch,range(g),tosamp,nch,i,ans,switch,iter  

* integer*2 param(10),mode,das20  

* real frepch,b(8),xsllope,vsllope,(g),patm,wventd,vimc0,vincon  

* real v1l,v12,v13,v14,v15,v16,v17,v18,vint,inv,vvent,vinc  

* real mu,rho,g,vel,re,chord,dot,l,w,ang,ring,relarge,even  

* real v1mf0,v1l0,v120,v130,v140,v150,v160,v170,v180,temp  

* real tslop1,tslop2,tslop3,tslop4,tslop5,tslop6,tslop7,tslop8  

* real v1mf0,vt10,vt20,vt30,vt40,vt50,vt60,vt70,vt80,temp  

* character*15 date  

* character*10 name,fnamel,fname2  

* character*6 imgnam  

* character*8 imgcnt  

* *** tunnel calibration slopes  

* units -> Pa/Volt  

* units -> Pa/Pa  

* units -> 2.7778  

* units -> Actual Volts (voltmeter)/DAS20 Sensed Volts  

* incslp=0.9999637  

* units -> deg.C/Volt  

* tslop2=11.5132345  

* tslop1=11.5132545  

* units -> deg.C/Volt  

* tslop6=11.5582363  

* tslop5=11.5411361  

* tslop4=11.5320815  

* tslop3=11.5158382  

* tslop2=11.5132345  

* tslop1=11.4819661  

* units -> deg.C/Volt  

* *** tunnel calibration slopes

```

#### APPENDIX C: Heat Transfer Codes

```

*** user inputs run information
read(0,(33)) runno
print*, 'Enter 3 digit run number'
read(0,(40)) des
print*, 'Enter run description'
print*, 'Enter test date'
read(0,(15)) date
print*
print*, 'Enter test date'
read(0,(15)) dat
print*
print*, 'Enter run number'
read(0,(32)) nchno
print*, 'Enter 3 digit run number'
read(0,(43)) nchno
print*, 'Enter run information
*** user inputs run information

fch=sch+nch-1

*** total number of samples = #channels * #samples per channel
totstamp=nch*nchapch
if(totstamp.gt.32760)then
print*, 'Total # of samples must not exceed 32760'
print*, '# of channels * # of samples per channel',
print*, 'must be less than 32760'
endif

close(unit=8)
read(8,*)
read(8,*) b(7)
read(8,*) b(4),b(5),b(6)
read(8,*) b(1),b(2),b(3)
read(8,*) irange(7)
read(8,*) irange(4),irange(5),irange(6)
read(8,*) irange(1),irange(2),irange(3)
read(8,*) irange(1)*irange(2)*irange(3)
read(8,*) sch,nch,nchapch
open(unit=8,file='board.dat',status='old')
*** read in board calibration information
read(8,*)

switch=0
flag=0
iter=0
ainc=1.*w
chord=0.3048
c      rinc = 0.2479
rinc=0.2643
w=0.0762
l=0.3984625
*** properties of the Inconel strip in SI units
dmalev=1
idlev=2
baseadr=#300
*      baseadr=base address, idlev=interrupt level, dmalev=DMA level
*** DAS20 settings
tslop9=11.5687180
tslop8=11.5590531
tslop7=11.5853887

```

```

print*,Enter output file name without extension (max 6 letters)
read(0,(a6)) name
print*,Enter crystal temperature (30,45)
print*,Enter crystal temperature
read*,crysitem
name1(1:6)=name(1:6)
name1(7:10)='raw'
name2(1:6)=name(1:6)
name2(7:10)='out'
frame2(1:6)=frame(1:6)
frame2(7:10)=frame(7:10)
print*,Enter ambient Temperature (deg.F)
print*,Enter ambient Temperature (deg.F)
read*,temper
* convert deg.F to deg.C
temper=(5.0/9.0)*(temper-32.)
*** DAS20 channel information
frame1(1:6)=frame(1:6)
frame1(7:10)='raw'
frame2(1:6)=frame(1:6)
frame2(7:10)='out'
print*,Enter INCORRECT VOLTAGEx
print*,CHANNEL 1 -----> INCORRECT VOLTAGEx
print*,CHANNEL 0 -----> VENTURI CONTRACTION PRESSURE XDUCER
print*
print*
print*
print*,INCORRECT VOLTAGEx
print*,CHANNEL 2 -----> ALL THERMOCOUPLES
print*,Enter Actual Incorrec Voltag reading with POWER OFF
print*,VINCACD
read*,vincacd
*** open output files
open(unit=9,file='name1',status='new')
open(unit=9,file='name2',status='new')
open(unit=10,file='name2',status='new')
*** write header information to data files
*** initialize DAS20: Mode 0
mode=0
param(1)=basadr
param(2)=imdev
param(3)=dmalev
rcode=das20(imode,param)
if(rcode.ne.0)print*,imode,rcode
bufler=alloc(32766)
*** take zeroes
l print*
print*,Ready to take zeroes? (y or n)

```

```

read(0,(a1)) yesno
if(yesno.eq.'Y'.or.yesno.eq.'y')then
  vven10=0.0
  vmc0=0.0
  print*
  pause'Set thermocouple to Tinside1 and press <enter>',
  call vmean(v,sch,fch,nch,nsapch,frepch,iter,react,range,b)
  vven10=vven10+v(1)
  vmc0=vmc0+v(2)
  v110=v(3)
  print*
  pause'Set thermocouple to Tinside2 and press <enter>',
  call vmean(v,sch,fch,nch,nsapch,frepch,iter,react,range,b)
  vven10=vven10+v(1)
  vmc0=vmc0+v(2)
  v120=v(3)
  print*
  pause'Set thermocouple to Tinside2 and press <enter>',
  call vmean(v,sch,fch,nch,nsapch,frepch,iter,react,range,b)
  vven10=vven10+v(1)
  vmc0=vmc0+v(2)
  v110=v(3)
  print*
  pause'Set thermocouple to Tinside3 and press <enter>',
  call vmean(v,sch,fch,nch,nsapch,frepch,iter,react,range,b)
  vven10=vven10+v(1)
  vmc0=vmc0+v(2)
  v130=v(3)
  print*
  pause'Set thermocouple to Tinside3 and press <enter>',
  call vmean(v,sch,fch,nch,nsapch,frepch,iter,react,range,b)
  vven10=vven10+v(1)
  vmc0=vmc0+v(2)
  v140=v(3)
  print*
  pause'Set thermocouple to Tinside4 and press <enter>',
  call vmean(v,sch,fch,nch,nsapch,frepch,iter,react,range,b)
  vven10=vven10+v(1)
  vmc0=vmc0+v(2)
  v150=v(3)
  print*
  pause'Set thermocouple to Tinside5 and press <enter>',
  call vmean(v,sch,fch,nch,nsapch,frepch,iter,react,range,b)
  vven10=vven10+v(1)
  vmc0=vmc0+v(2)
  v160=v(3)
  print*
  pause'Set thermocouple to Tinside6 and press <enter>',
  call vmean(v,sch,fch,nch,nsapch,frepch,iter,react,range,b)
  vven10=vven10+v(1)
  vmc0=vmc0+v(2)
  v170=v(3)
  print*
  pause'Set thermocouple to Tinside7 and press <enter>',
  call vmean(v,sch,fch,nch,nsapch,frepch,iter,react,range,b)
  vven10=vven10+v(1)
  vmc0=vmc0+v(2)
  v180=v(3)
  print*

```



```

switch=1
endif
$ne1 2 now? (Y or N)
read(0,(A1)) yesno
if(yesno.eq.'Y'.or.yesno.eq.'y')then
  call vmean(v,sch,fch,nch,nsapch,frapch,iter,fract,range,b)
  vini=v(3)
  tini=temper+(vini-vlimd)*tislope9
  convrt temperature from degrees Celsius to degrees Kelvin
  dum=dum+273.15
  tavg=(tini+(crysmt+273.15))/2.0
  else
    goto 2
  endif
  tavg=tavg-(vini-vlimd)*tislope
  event=((2.99958065442e-10)*retrag**2*tavg**4)/(chord**2*pattm*(1
  -read*,tretarg
  print*,Event,Desired Reynolds number
  print*,event
  print*,tretarg
  print*,event
  print*,tavg+110.0)**2*xslope*vslope)
  write(0,20)Target Venturi Voltage = ,event+vven10
  20   format(1x,a,f6.3)
  pausePress enter to continue
  print*
  print*
  print*,vinacl0+(event)*incslp
  print*,print*
  user chooses to enter new value of P atm
  elseif(ans.eq.2)then
    *** user chooses to take data
    elseif(ans.eq.3)then
      *** user chooses to enter new value of P atm
      read*,pattm
      print*,Enter value of atmospheric pressure (inHg)
      print*,Enter value of atmospheric pressure (inHg)
      convert inHg to Pascal
      pattm=pattm*3386.38815789
      switch=1
      pausePress <enter> to continue
      print*,print*
      if(switch.eq.0)then
        print*,You must first tell me the atmospheric pressure,
        print*,to continue
      endif
      vven1=0.0
      vinc=0.0
      print*
      print*

```



```

*** calculate temperatures in degrees Celsius
t1=temper+(vt1-vt10)*tslop1
t2=temper-(vt2-vt20)*tslop2
t3=temper+(vt3-vt30)*tslop3
t4=temper+(vt4-vt40)*tslop4
t5=temper+(vt5-vt50)*tslop5
t6=temper+(vt6-vt60)*tslop6
t7=temper+(vt7-vt70)*tslop7
t8=temper+(vt8-vt80)*tslop8
t9=temper+(vt9-vt90)*tslop9
t10=temper+(vt10-vt100)*tslop10
t11=temper+(vt11-vt110)*tslop11
vvenu=vvenu/9.0
vinc=vinc/9.0
*** convert temperatures from degrees Celsius to degrees Kelvin
t11=t11+273.15
t12=t12+273.15
t13=t13+273.15
t14=t14+273.15
t15=t15+273.15
t16=t16+273.15
tavg=(t11+(crysitem+273.15))/2.0
mu=0.000018*(tavg/293.15)**1.5*(403.15)/(tavg+110.0)
rho=patm/(287.0*tinf)
*** calculate air density
*** calculate air viscosity using Sutherland's Law
* temperature near strip assumed average of freestream
* and liquid crystal strip temperature
* calculate dynamic pressure and airspeed
d=(vvent-vvenu0)*xslope*vslope
vel=sqr(2.0*q/rho)
*** calculate Reynolds number
*** calculate dynamic pressure and airspeed
*** calculate dynamic pressure and airspeed
*** calculate air density
*** calculate Reynolds number
re=(rho*vel*chord)/mu
calcReynoldsNumber
*** calculate dynamic pressure and airspeed
print*,vinc=vinc0+(vinc-vinc0)*incslip
vincon=vinc0+(vinc-vinc0)*incslip
print*,vinccon = ,vinccon
print*,vvent = ,vvent
print*,vvent = ,vvent
print*,vvnu = ,vvnu
print*,vvel = ,vvel
print*,rho = ,rho
print*,rho = ,rho
print*,re = ,re
*** print*,Do you wish to use these values?
read(0,(a1))yesno
if(yesno.eq.'n' .or.yesno.eq.'N')go to 2
print*,yessno

```

```

*** calculate total heat flux generated per unit area
*** read*,vincoun
print*,Enter INCONEL voltage,
read*,vincoun
*** input image name and counter number
*** print*,Enter image name (6 characters)
read(0,(a6)) imgnam
print*,Enter video counter (xx:xx:xx)
print*,Enter video counter (xx:xx:xx)
read(0,(a8)) imgcnt
*** read(0,(a8)) imgcnt
print*,Enter video counter (xx:xx:xx)
print*,Enter video counter (xx:xx:xx)
*** write raw voltages and processed data to files
*** write(9,50) imgnam,imgcnt,vvenc-vvend0,vincon,vinl-vind0,vi1-
$0
$16,vi2-vi20,vi3-vi30,vi4-vi40,vi5-vi50,vi6-vi60,vi7-vi70,vi8-vi8
white(10,60) imgnam,imgcnt,re,vel,rho,qdot,tint,i1,i2,i3,i4,i5
50 format(1x,a6,1x,a8,1x,f7.0,1x,f5.2,1x,f5.3,1x,f10.4,1x,9(f7.3,1x))
60 format(1x,a6,1x,a8,1x,f5.3,1x,f6.3,1x,9(f8.3,1x))
else
print*
print*,PLEASE CHOOSE A NUMBER BETWEEN 1 AND 3 (OR 90 TO QUIT)
endif
***** SUBROUTINE VMEAN(V,SCH,FCH,NCH,NSAPCH,FREPCH,ITREC,FREACT,
* Calculates the mean voltage sampled in each input channel
* INTEGER*2 COUNT(11000),IRANGE(8)
* INTEGER*2 NCCH,SCH,FCH,IPRINT,NSAPCH
***** end
1000 close(unit=9)
close(unit=10)
goto 2

```

```

REAL *4 IE,E,V,A(8),B(8)
* COMMON A(8),B(8)
* DIMENSION IE(8),E(8),V(8)
* USE of Mode 6 for sampling
* SAMPLE: extremal subroutine (MODE6VG,FOR)
* IPINT=0
* IPINT=0
CALL SAMPL(E,SCH,FCH,NCH,NSAPCH,FREPCH,ICOUNT,IPRINT,JTER,
&FREACT,JRANGE)
DO 10 I=1,11000
* Scaling conversion when transferring bipolar data in unipolar mode
* Make sure this conversion is performed before the averaging loops.
IF (ICOUNT(I).GT.2047) THEN
  ICOUNT(I)=ICOUNT(I)-4096
DO 10 I=1,11000
  ICOUNT(I)=ICOUNT(I)-4096
  ENDIF
  10 CONTINUE
* WRTE(0,*)(COUNT(I),I=1,NSAPCH*NCH)
  DO 20 j=1,NCH
    * in the 1-D array ICOUNT and categorize the averaged data by channels
    * into a different 1-D array E(j).
    IF (IE(j).EQ.0) THEN
      E(j)=E(j)+REAL(IE(j)-E(j))/A
      IE(j)=ICOUNT(INDEX+j)
    ENDIF
    20 CONTINUE
  DO 40 I=1,NSAPCH
    INDEX=(I-1)*NCH
    * These loops average (running average) all sampled data (counts)
    * in the 1-D array ICOUNT and categorize the averaged data by channels
    * into a different 1-D array E(j).
    IF (IE(j).EQ.0) THEN
      E(j)=E(j)+REAL(IE(j)-E(j))/A
      IE(j)=ICOUNT(INDEX+j)
    ENDIF
    40 CONTINUE
  DO 45 j=1,NCH
    * PRINT*,INDEX,j
    * PRINT*,INDEX,j,INDEX,j
    * STOP
    * ENDIF
    * CONTINUE
    * DO 60 I=1,NCH
      * Continue from counts to volts for the appropriate input range
      * V(I)=B(SCH+I)*E(I)
      * RETURN
      * END
END

```

```

***** Data Reduction Code apbwining.jor *****

$include: 'C:\aurora\aunderst\for'
$include: 'C:\aurora\aunderst\for'

***** apbwining for: This program was written to reduce data for the
***** liquid crystal experiments on the SM701 airfoil done at ABB
***** apbwining for: This program reads an input file called input.dat which
***** contains the following information:
***** Line 1 : Liquid Crystal Temperature (30 or 45)
***** Line 2 : Starting Value of Hue, Band of Hue, Saturation
***** Line 3 : # of intensities to reduce (nred)
***** Line 4 : Intensity 1, Intensity 2, Intensity 3, ...
***** Line 5 : output file name to contain h, x/c data for Intensity 1
***** (be sure to include extension)
***** Line 6 : output file name to contain h, x/c data for Intensity 2
***** (be sure to include extension)
***** Line 7 : " " " " " " Intensity 3
***** Line nred+1: atmospheric pressure in Pa
***** Line nred+2: number of images that need to be column-corrected
***** Line nred+3: image#, column correction value
***** Line . . . : number of images that need user-added h values
***** Line . . . : image#, col 1 to calc.h, col 2 to calc.h, col 3 to calc.h
***** Line . . . : beginning screen row of reduction, ending row
***** Line . . . : total # of images
***** Line . . . : image names (total number equal to line nred+4)
***** Line XX-XX : image#, re,vel,rho,dotl,imf,tcc(1),tcc(2),
***** tcc(3),tcc(4),tcc(5),tcc(6),tcc(7),tcc(8)
***** Line . . . : each image. These values come from the data
***** for each image.
***** Line . . . : average, cryst, vinc, slope, intcp, ratio
***** real ddotl,rho,re,xocc(8),tcc(8),intf
***** real pdcovv,pdcovd,qdrad,xoverc,averat,avgmu
***** real q,vel,chorid,mu,twinc,haa,bb,xocc(21)
***** real sigma,epsmc,epswal,k,tavg,insid,avgrate,avgvel,avgrho
***** integer*2 init,erst,status,endd,bu0(1),bu1(1),bu2(1)

***** acquisition code getdata.exe.
***** acquisition code getdata.exe.

*****
```

real tot(500),rad(500),tcr(500),inflim(500),xovc(500),cond(500)  
 real convy(500),hh(500),adv(500),advx(500),advy(500),advz(500)  
 real dhdtn,dhdtr1,w,rstdp,epsp,deltw,delt,dhdw,dhdz,dhdy,dhdx  
 real delk,delle,deltw,deltc,deltin,deltl,deltv,uh,u1,uhd10,uhdcoo  
 integer numpc,col(21),begrw,endrow,ni,j,imgnum,imgcrc(20)  
 integer npic,nred,int(20),cryslem,numarl,numcor,covral,addp13(20)  
 integer mb,nr,nc,sal,cout  
 integer addpt(20),addpl(20),numpls,colpt1,colpt2,colpt3,unmet  
 character\*16 imgnam  
 character\*16 print(20),printf1  
 integer flag1,flag2,flag3,unmet  
 character\*8 imgnam  
 character\*8 imgnam  
 character\*8 imgnam  
 \* hardcoded physical data  
 \* thermal conductivity of wing material in Watts/m/K  
 \* wing chord in meters (chord is 12 inches)  
 $k=0.224$   
 \* Inconel strip length in meters  
 $l=0.3984625$   
 \* Inconel strip width in meters  
 $w=0.0762$   
 \* Inconel strip resistance in ohms  
 $rstrip=0.2643$   
 \* Stefan-Boltzmann constant in Watts/m<sup>2</sup>/K<sup>4</sup>  
 $\sigma_{\text{Stefan}} = 5.67 \times 10^{-8}$   
 \* emissivity of the beige tunnel walls with Plexiglas sections  
 $\epsilon_{\text{ps\_epsic}} = 0.94$   
 \* emissivity of the black paint on the Inconel strip  
 $\epsilon_{\text{psimc}} = 0.94$   
 \* Ideal Gas constant in SI units  
 $R=287.0$   
 \* uncertainty analysis values in SI units  
 $dell=0.00079375$   
 $delw=0.00079375$   
 \* Uncertainty analysis values in SI units  
 $delle=0.02$   
 $delk=0.02$   
 $delw=0.000381$   
 $delr=0.001$   
 $deltin=0.2$   
 $deltl=0.2$   
 $xocc(1)=0.02$   
 \* of the 8 thermocouple positions  
 \* x/c locations and corresponding wing thicknesses (inches)

```

        read(14,*)
        crytem

        averho=0.0
        avgve=0.0
        avere=0.0
        numerat=0
        numerac=0
        ratio=0.0
        print*
        blank=0.0
        j=1
        open(unit=14,file='input.dat',status='old')
* read input file containing all necessary information for an entire run

        continue
        addp3(i)=0
        addp2(i)=0
        addp1(i)=0
        imgecor(i)=0
        do 2 i=1,20
* zero addp's (array for user added b points)
* zero imgecor (image column correction array)
        close(unit=10)
        125 format(i3,F5.2)
        read(10,125) (col(i),xoc(i),i=1,numxc)
        open(unit=10,file=xfile,status='old')
        xfile='colxoc.dat'

        numxc=21
* read column, x/c data table

        continue
        thick(i)=thick(i)*0.0254
        do 1 i=1,8
* convert inches to meters
        thick(8)=0.382
        thick(7)=0.387
        thick(6)=0.412
        thick(5)=0.377
        thick(4)=0.413
        thick(3)=0.410
        thick(2)=0.414
        thick(1)=0.405
        xoc(8)=0.82
        xoc(7)=0.70
        xoc(6)=0.545
        xoc(5)=0.40
        xoc(4)=0.26
        xoc(3)=0.175
        xoc(2)=0.10
        xoc(1)=0.05

```

```

if(cryitem.eq.30)then
  deltc=0.2
  elseif(cryitem.eq.45)then
    deltc=0.15
  endif
  print*, 'Crystal Temperature must be either 30 or 45!'
else
  read(14,*), mb, sat
  read(14,*), nred
  read(14,*), (imt(i),i=1,nred)
  read(14,*), p
  read(14,*), numcor
  if(numcor.eq.0)goto6
  do 5 i=1,numcor
    read(14,*), imgnum,corrval
    read(14,*), colpt1, colpt2, colpt3
    read(14,*), imgnum,corrval
    addpt3(imgnum)=colpt3
    addpt2(imgnum)=colpt2
    addpt1(imgnum)=colpt1
    continue
  5 continue
  read(14,*), numps
  if(numps.eq.0)goto8
  do 7 i=1,numps
    read(14,*), imgnum,corrval
    addpt2(imgnum)=colpt2
    addpt1(imgnum)=colpt1
    read(14,*), imgnum,corrval
    addpt3(imgnum)=colpt3
    continue
  7 continue
  read(14,*), npt
  if(npt.eq.0)print(1)
  print(1)
  inten=int()
  printint=print()
  open(unit=13,file='printitl,status='unknown')
* open print file which will contain all x/c, h data to facilitate plotting
* Output files will contain the following information
*   x/c(hc/m^2/K) Uh %Uh qdot(W/m^2) Uqdot qdotn Uqdotn qdotn
*   Uqdotn qdotn Uqdotn (crys-t-un) U(crys-t-un) %COND %COND %RAD
*   cryst(k) insid(k) int(k) twing(m)
*   Second Quadcond qdotn Uqdotn tcryst minus tcryst minus tcryst
*   CONV Percent COND Percent RAD cryst insid int twing
*   write(13,135), xoc h Uh Percent Uqdot qdotn Uqdotn qdotn ad
*   cryst(k) insid(k) int(k) twing(m)
*   * * *

```

```

135 format(lx,a)
$CONV_Percent_COND_Percent_RAD_tcrst_tnsid_tnt_twincg
$Second_Uqdcoond_drdad_Uqdrad_tcrv_minus_tnt_U_tcrv_minus_tnt_Percen
write(11,135) 'xoc h Uh_Percent_Uh_ddot_Uqdcoot_dcoony_Uqdcoony_d
130 format(lx,2a)
write(0,130)'Name of print file : ',printfl
write(0,130)'Name of log file : ',logfl
write(0,130)'Name of output data file : ',outfl
write(0,130)'Name of image file : ',imgfl
write(0,*)'called colxoc.dat'
write(0,*)'Name of file containing column,x/c information must be
open(unit=12,file=logfl,status='unknown')
logfl(1:10)='log
logfl(1:6)=imgnam
open(unit=11,file=outfl,status='unknown')
outfl(7:10)='out
outfl(1:6)=imgnam
open(unit=8,file=imgfl,status='old')
imgfl(7:10)='img
imgfl(1:6)=imgnam
avgrho=avgrho+rho
avgvel=avgvel+vel
average=average+re
endif
devl=0.01
else
devl=0.001
if(vinc.lt.3.25)then
$16.3)
10 format(1x,a6,1x,a8,1x,f7.0,1x,f5.2,1x,f5.3,1x,f10.4,1x,9(f7.3,1x),
$3),tcc(4),tcc(5),tcc(6),tcc(7),tcc(8),vinc
read(14,10) imgnam,imgcnt,re,vel,rho,ddot,tint,tgc(1),tgc(2),tcc
status=audsisp(1)
status=ausmod(0)
init=auinit()
err=auerrm()
* Initialize 2871 board to default settings
***** ****
* Initialization and set-up
***** ****
do 1000 ii=1,ni
* begin loop to reduce each image in turn
flag1=0
flag2=0
flag3=0

```

```

        count=counter+1
        * passes all criteria, keep point and count it

        if(buf2(l).lt.lb.or.buf2(l).gt.lb+mb) goto 100
        * discard if hue is not in defined range
        * hue buffer filtering

        if(buf0(l).lt.limten) goto 100
        * check local intensity value and discard if less than threshold value

        if(buf1(l).lt.sat) goto 100
        * check local saturation value and discard if less than threshold value

        * this line was to correct the hardware problem on psu image processor
        * status=auptrx(0,nr,nc+l,lbuff,buf1,buf2)
        * status=augtrx(0,nr,nc,l,buff,buf1,buf2)

        * and copy into next column to fix bad columns
        * read HSI

        do 100 nr=beginrow,endrow,l
        count=0
        avghue=0.0
        if(nc+imgcor(i)).gt.col(l).or.nc+imgcor(i).lt.col(numxc)) goto 200
        do 200 nc=510,2,-2
        ****
        **** GET HUE VALUES AND SAVE
        ****
        status=aurest(0,0,0,imagefile,jer)

        write(0,*)
        165 format(1x,a25,f7.0)
        write(0,165) Reynolds Number; 're
        160 format(1x,a25,f5.2)
        write(0,160) 'Wind Velocity (m/s); 'vel
        write(0,155) Density (kg/m3); 'rho
        write(0,*)
        write(0,*) 'Computed Quantities..'
        write(0,*)
        157 format(1x,a25,f8.1)
        write(0,157) Atmospheric Pressure (Pa); 'p
        155 format(1x,a25,f5.3)
        write(0,*)
        write(0,150) 'Saturation Threshold; 'sat
        write(0,150) Intensity Threshold; 'inten
        write(0,150) Band of Hue; 'mb
        150 format(1x,a30,i3)
        write(0,150) Starting value of Hue; 'lb
        write(0,150) Crystal Temperature (deg.C); 'crysitem
        write(0,*)
        write(0,*)
        * print to screen so user can check for input errors

```

```

224

    avghue=avghue+real(buf2(1))

    * now that the hue has been recorded, change the pixel on the image
    * processor screen to a DARK COLOR so it can be seen
    buf0(1)=0
    buf1(1)=180
    buf2(1)=170
    status=auptx(0,nr,nc,l,buf0,buf1,buf2)

    100 continue

    c now it's done with one column, average the hue
    if(count<1.c,nc-1)goto200
    avghue=avghue/real(count)

    * convert hue to temperature based on liquid crystal calibration
    * this temperature will be in degrees Celsius
    * Note that 2 calibrations are coded: 30 and 45 deg. C crystals
    * from the hue vs temperature calibration in degrees Celsius
    if(crytem.eq.30)then
        slope=122.52
        intcpt=-335.5
        slope=549.01
        intcpt=-24182.0
        else
            slope=549.01
            intcpt=-24182.0
            print*, 'Only 30 and 45 degree Celsius crystals are valid!!'
            goto 2000
        endif
        cryst=crys+273.15
        * convert degrees Celsius to Kelvin
        cryst=(avghue-intcpt)/slope
        179 continue
        do 180 i=1,numxc-1
            if(nc+imgcor(i).le.col(i).and.nc+imgcor(i).ge.col(i+1))goto185
            180 continue
            185 continue
            aa=real(nc+imgcor(i)-col(i))/real(col(i+1)-col(i))
            bb=xoc(i+1)-xoc(i)
            xoverc=aa*bb+xoc(i)
            if(xoverc.ge.0.0.and.xoverc.lt.xoc(i))then
                ifnmid=tcc(i)
                twindg=tthick(i)
                goto 195
            else
                find conduction losses
                * x/c falls before the first TC location (0.02)
                if(xoverc.ge.0.0.and.xoverc.lt.xoc(i))then
                    ifnmid=tcc(i)
                    twindg=tthick(i)
                    goto 195
                else
                    ifnmid=tcc(i)
                    twindg=tthick(i)
                    goto 195
                end if
            end if
        end do
        195 continue
        * find x/c location for the given column, nc
        xoverc=aa*bb+xoc(i)
        if(xoverc.ge.0.0.and.xoverc.lt.xoc(i))then
            ifnmid=tcc(i)
            twindg=tthick(i)
            goto 195
        else
            ifnmid=tcc(i)
            twindg=tthick(i)
            goto 195
        end if
    end if
end if

```

```

        h=qdcconv/(tcryst-tint)
qdcconv=qdot-qdcond-qdrad
* find convective heat transfer coefficient, h (Watts/m^2/K)

        endif
        goto206
xoverc(umems)=xoverc
tintin(umems)=tint
tcryst(umems)=tcryst
rad(umems)=qdrad
tot(umems)=qdot
umems=umems+1
if(xoverc>t,xoverc,t,xoverc,le,1.0)then

```

- \* easy calculation of the conduction losses.
- \* This is because the internal structure of the wing does not allow an conduction loss that occurs during the first 0.82 % of the chord.
- \* the conduction losses will be estimated as the average percentage
- \* Note that if x/c falls after the last TC location (0.82), then

```

        endif
        avgrat=ratio/real(umarat)
umarat=umarat+1
ratio=ratio+qdccond/qdot
if(xoverc,le,xoverc,gt,xoverc,lt,xoverc,le,0.82)then
qdrad=sigma*(epslinc*tcryst**4-epswal*um**4)
* find radiation losses
qdccond=k*(tcryst-tinsid)/twine

```

195 continue

```

twine=aa*bb+thick(i)
bb=thick(i+1)-thick(i)
aa=(xoverc-xocc(i))/(xocc(i+1)-xocc(i))
193 continue
192 continue
if(xoverc,ge,xocc(i).and.xoverc,lt,xocc(i+1))goto 193
do 192 i=1,7
* then find wing thickness at x/c location

```

```

tinsid=aa*bb+ttc(i)
bb=ttc(i+1)-ttc(i)
aa=(xoverc-xocc(i))/(xocc(i+1)-xocc(i))
191 continue
190 continue
if(xoverc,ge,xocc(i).and.xoverc,lt,xocc(i+1))goto 191
do 190 i=1,7
* from thermocouple array
* find internal temperature at x/c location by interpolating

```

endif

$\$2x), 3(f6.2, 2x), f7.5)$

198 format(lx,f5.3,2x,2(f8.2,2x),f6.1,2x,8(f7.2,2x),2(f6.2,2x),3(f6.1,

$\$qdot{t}*100, qdrad/qdot{t}*100, tcryst, tinsid, tinf, twinge$

$\$sound, uquadcod, qdrad, uquadrad, (tcryst-tinf)/u1, uquadconv, qdot{t}*100, qdcodan/d$

$wfile(11,198) xoverc, h, uh, uh/b*100, qdot{t}, uquadtot, uquadconv, uquadconv, qdc$

\* store xc and h data along with all other data in a file

$uquadconv=uquadtot+uquadcod+uquadrad$

\* uncertainty in qdcodn calculation (conductive heat flux)--> h numerator

$uquadrad=sqr((drdce*dele)*2+(drdce*dele)*2+(drdce*dele)*2+(drdce*dele)*2)$

$drdce=-4, *sigma*eps*tcryst*3$

$drdce=4, *sigma*(tcryst*4-tinf*4)$

\* uncertainty in qdrad calculation (radiative heat flux)

$\$dcddtw*delw)**2)$

$uquadod=sqr((dcdkk*dekk)*2+(dcddc*delc)*2+(dcddt*deltin)*2+(dc$

$dcddtw=k*(tcryst-tinsid)/twinge**2$

$dcddt=k/twinge$

$dcddc=k/twinge$

$dcdkk=(tcryst-tinsid)/twinge$

\* uncertainty in qdcodn calculation (conductive heat flux)

$\$oldw*delw)**2)$

$uquadtot=sqr((doldv*delv)*2+(doldr*delr)*2+(doldl*dell)*2+(d$

$doldw=-vinc**2/(rstrip*I*w**2)$

$doldr=-vinc**2/(rstrip*I*w**2)$

$doldl=-vinc**2/(rstrip*I*w)$

\* uncertainty in qdot{t} calculation (total heat flux generated)

$ut=sqr(dele)*2+delef*2)$

\* uncertainty in (Tcryst-Tinf) calculation--> h denominator

$\$**2+(dhdtl*delli)*2+(dhde*dele)*2)$

$\$2+(dhdkk*dekk)*2+(dhdc*delc)*2+(dhdtm*delli)*2+(dhdtw*delw)*2$

$uh=sqr((dhdv*delv)*2+(dhdr*delr)*2+(dhdl*dell)*2+(dhdw*delw)*2$

$dhdtm=k/(twinge*(tcryst-tinf))$

$\$*(tcryst**4-tinf**4)/(tcryst-tinf)**2$

$\$inc*(tcryst-tinf)**2+4, *sigma*eps*tinf**3/(tcryst-tinf)-sigma*eps$

$dhdtl=vinc**2/rstrip*I*w*(tcryst-tinf)**2-k*(tcryst-tinf)/(twi$

$dhdtw=vinc**2/rstrip*I*w*(tcryst-tinf)**2-k*(tinsid-tinf)/(twi$

$\$g*(tcryst-tinf)**2-4, *sigma*eps*tcryst**3/(tcryst-tinf)+sigma*eps$

$dhdc=-vinc**2/rstrip*I*w*(tcryst-tinf)**2-k*(tinsid-tinf)/(twi$

$dhde=-sigma*(tcryst-tinsid)/(twinge*(tcryst-tinf))$

$dhdk=-tcryst-tinsid)/(twinge*(tcryst-tinf))$

$dhdw=vinc**2/(w**2*rstrip*I*(tcryst-tinf))$

$dhdl=-vinc**2/(l**2*rstrip*w*(tcryst-tinf))$

$dhvi=2.*vinc/(rstrip*I*w*(tcryst-tinf))$

\* uncertainty in h calculation

```

199 format(1x,f4.2,3x,f6.2,3x,f6.1)
write(0,199) xoverc,h,uuh,h*100.,adot,uqdot,dcovn,uqdcnv,qdc
200 continue
201 continue
* continue onward to the next column
if(flag1.eq.1.or.flag2.eq.1.or.flag3.eq.1)goto201
206 continue
$adot*100.,qdrad/qdot*100.,tcryst,insid,tint,twing
$ond,uqdcod,qdrad,uqdrad,(tcryst-tint),ut,qdcovn/qdot*100.,adcoand/
write(13,198) xoverc,h,uuh,h*100.,adot,uqdot,dcovn,uqdcnv,qdc
200 continue
if(addptl(i).ne.0)then
  tcryst=44.23+273.15
  if(addpt2(i).ne.0)then
    tcryst=44.23+273.15
    addpt2(i)=0
    nc=addpt2(i)
    flag2=1
    goto179
  endif
if(addpt3(i).ne.0)then
  tcryst=44.23+273.15
  addpt3(i)=0
  nc=addpt3(i)
  flag3=1
  goto179
endif
* write test information to log file
* all columns done now
* write test information to log file
write(12,150)'Crystral Temperature (deg.C):',crysitem
write(12,150)'Starting value of Hue:',hb
write(12,150)'Band of Hue:',mb
write(12,150)'Intensity Threshold:',inten
write(12,150)'Saturation Threshold:',sat
write(12,150)'Atmospheric Pressure (Pa):',p
write(12,155)'Density (kg/m^3):',rho
write(12,160)'Wind Velocity(m/s):',vel
write(12,165)'Reynolds Number:',re
if(h.eq.0)then
  write(12,250)
endif

```

```

        end
stop

* all images for all intensity criteria values now done
2000 close(unit=14)

gotof3
* continue on to next intensity criteria value
j(j+1)gotof2000
j=j+1

rewind(unit=14)
close(unit=13)

1500 continue

$blank
$00,cond(i)/tot(i)*100,rad(i)/tot(i)*100,tcr(i),blank,imfin(i),
$nd(i),blank,rad(i),blank,(tcr(i)-imfin(i)),blank,conv(i)/tot(i)*1
write(13,198) xcov(i),hh(i),blank,tot(i),blank,conv(i),blank,co
hh(i)=conv(i)/(tcr(i)-imfin(i))
conv(i)=tot(i)-cond(i)-rad(i)
cond(i)=avgrat*tot(i)
do 1500 i=1,numest
* now write x/c,h data to print file for x/c > xoclc(g)
* continue on to next image
1000 continue
* continue on to next image
1000 continue
close(unit=12)
close(unit=11)
close(unit=8)

write(0,('A10,I3')) ENDD = ,endd
endd=auend()

250 format(lx,a,f7.0)
251 format(lx,a,f5.2)
252 format(lx,a,f5.3)
253 format(lx,a,f11.9)
endit
write(12,253)'Average Mu (all images): ',avgmu
avgmu=(avgrho/real(m))*(avgve/real(m))*chord/(avge/real(m))
write(12,252)'Average Rho (all images): ',avgrho/real(m)
write(12,251)'Average Vel (all images): ',avgve/real(m)
write(12,250)'Average Re (all images): ',avgrho/real(m)

```

```

upack F:\hwdata.bin,e:\todd\hw\aswtsm70\hotwire%1.raw,0-104448/b/das16
erase F:\hwdata.log
copy F:\hwdata.log e:\todd\hw\aswtsm70\hotwire%1.log
copy F:\hwdata.bin e:\todd\hw\aswtsm70\hotwire%1.bin
piotshot
streamer /b=stream.bat
speedisk F:\

mkfile F:\hwdata.bin/v 204
erase F:\hwdata.bin
waitgain
hotlast.bat

rem NO TRAVERSE IS DESIRED)
rem THIS BATCH FILE DOES NOT TRAVERSE THE PROBE!!! (USED FOR LAST POINT WHERE

```

*hotlast.bat*

```

rem upack F:\hwdata.bin,e:\todd\hw\aswtsm70\hotwire%1.raw,0-104448/b/das16
erase F:\hwdata.log
copy F:\hwdata.log e:\todd\hw\aswtsm70\hotwire%1.log
copy F:\hwdata.bin e:\todd\hw\aswtsm70\hotwire%1.bin
trav%2
piotshot
streamer /b=stream.bat
speedisk F:\

mkfile F:\hwdata.bin/v 204
erase F:\hwdata.bin
waitgain
hotwire.bat


```

```

copy cond.out E1C0N000.CON
call hotlast e103f000
call hotwire e102f000 100
call hotwire e101f000 100
zeroes

```

*Sample Main Batch File sample.bat*

This appendix contains the FORTRAN codes that were used for data acquisition and data reduction throughout the ASWT hot-wire anemometry experimentation. The codes are well-commented.

#### APPENDIX D: Hot-Wire Anemometry Codes

```

Zeros for program zeroes ****
* This program acquires initial atmospheric pressure and temperature
* Values as well as zeroes for : contraction pressure xducer, TC,
* Totalwake pressure xducer, and Static wake pressure xducer.
* CHANNEL 2 ----> Contraction Pressure Transducer
* CHANNEL 3 ----> Thermocouple
* CHANNEL 4 ----> Total wake Pressure Transducer
* CHANNEL 5 ----> P static wake Pressure Transducer
*
* CHANNEL 2 ----> Counteractation Pressure Transducer
* CHANNEL 3 ----> Thermocouple
* CHANNEL 4 ----> Total wake Pressure Transducer
* CHANNEL 5 ----> P static wake Pressure Transducer
*
real patm,temp,rapp,vventil,vco,clock,v(8),em(8),frpech
real vptwo,vpswo
integer totstamp
character*40 date
character*1 ans
common a(8),b(8)
open(unit=7,file='board.dat',status='old')
read(7,*),sch,fch,nsapch
read(7,*),range(1),range(2),range(3)
read(7,*),range(4),range(5),range(6)
read(7,*),range(7),range(8)
do 3 i=1,8
read(7,*),a(i),b(i)
do 3 continue
3 close(unit=7)
call adinit(basdat,dmalev,imlev,imleve,range)
* initialize DASH-16 board
* set sampling information
nch = fch-sch+1
itype = 0
* user enters information
PRINT*, 'Total no. of samples must not exceed 32,760'
PRINT*, 'i.e. No. of samples per channel x No. of channels',
PRINT*, 'must be less than 32,760'
IF (TOTSAMP.GT. 32760) THEN
TOTSAMP=NCH*NSAPCH
* Total number of samples = no. of channels x no. samples per channel
ENDIF
stop

```

```

print*,Please enter the DATE
read(0,'(40)') date
print*,Please enter the APPLIED FREQUENCY (Hz)
read(0,'(40)') freq
c* convert inHz to Pascals
c* read*,pattm
c* read*,pattm
c* convert inHg to Pascals
c* read*,pattm
print*,Please enter ATMOSPHERIC PRESSURE (inHg)
print*,Please enter ATMOSPHERIC PRESSURE (mmHg)
read*,pattm
c* convert mmHg to Pascals
pattm=pattm*133.322368421
print*,Please enter Temperature (deg.F)
read*,temper
* convert deg.F to Kelvin
temper=(5.0/9.0*(temper-32.0))+273.15
print*,Ready to sample zeroes? (y/n)
read(0,'(1)') ans
* record zeroes
if(ans.eq.'Y'.or.'ans.eq.'Y')then
call vmean(em,v,sch,nch,nsapch,trepcch,itype,iter)
print*,chan.0 zero = ',v(1)
print*,chan.1 zero = ',v(2)
print*,chan.2 zero = ',v(3)
print*,chan.3 zero = ',v(4)
print*,chan.4 zero = ',v(5)
print*,chan.5 zero = ',v(6)
vpsw0=v(6)
vptw0=v(5)
vtco=v(4)
vvent0=v(3)
pausesPress <enter> to continue
else
endif
goto 5
print*
print*
print*
print*
print*
print*,Well, when you are ready press y!
write(8,*),date
write(8,*),pattm
write(8,*),temper
write(8,*),fapp
open(unit=8,file='cond.out',status='unknown')

```

```

SUBROUTINE VMERGE(V,SCH,FCH,NCH,NSAPCH,FREPCH,ITYPE,ITER)
*-----*
      write(8,*), vmeanl0
      write(8,*), vtc0
      write(8,*), vptwo
      write(8,*), vpswo
      close(unit=8)

      end

      SUBROUTINE VMERGE(V,SCH,FCH,NCH,NSAPCH,FREPCH,ITYPE,ITER)
      *-----*
      INTEGER*2 ICOUNT(10000)
      INTEGER*2 NCH,SCH,FCH,NSAPCH
      DIMENSION A(8),B(8)
      IMERGE MODE
      CALL SAMPLF(clock,SCH,FCH,NCH,NSAPCH,FREPCH,ICOUNT,ITYPE,mode,fre
      DO 20 J=1,NCH
      DO 40 I=1,NSAPCH
      IF(PRINT,EG,1) WRITE(6,300) I,(E(J),J=1,NCH)
      20 E(J)=0.0
      DO 20 j=1,NCH
      DO 45 J=1,NCH
      INDEX=(I-1)*NCH
      DO 45 I=1,NSAPCH
      IF(PRINT,EG,1) WRITE(6,300)
      45 E(J)=E(J)+REAL((B(I)-E(I))/real(I)
      INDEX=ICOUNT(INDEX+j)
      DO 45 J=1,NCH
      IF(PRINT,EG,1) WRITE(6,330) I,(E(j),j=1,NCH)
      40 CONTINUE
      DO 50 j=1,NCH
      50 V(j)=(B(SCH+j)*E(j)+A(SCH+j)
      300 FORMAT(//,9X, No.,9X, Ch.1,9X, Ch.2)
      320 FORMAT(4F15.5)
      330 FORMAT(4I15)
      RETURN
      END

```

*Waiting for*  
program waitgain  
print\*  
print\*, MAKE SURE TUNNEL IS UP TO SPEED,  
print\*  
print\*, PLEASE SET GAIN then press <enter> to begin sampling,  
print\*  
print\*  
*Sstream.bat*

DAS16 LF=F:\HWDATA\LOG DR=F DF=HWDATA.BIN R=4.096 FC=0 LC=1 STRT=INT CSRC= INT BA=330 DL=3 CLK=1

```

*****  

* This program will read an input file containing data from previous  

* traverse positions. It will then sample new information for the  

* current traverse position. Then it will write all the traverse  

* positions' data back to the original file. Finally it will traverse  

* the probe to a new location.  

* CHANNEL 2 ----> Contaction Pressure Transducer  

* CHANNEL 3 ----> Thermocouple  

* CHANNEL 4 ----> Total wake Pressure Transducer  

* CHANNEL 5 ----> Static wake Pressure Transducer  

* positions' data back to the original file. Finally it will traverse  

* the probe to a new location.  

*****  

program pilothole
*****  

* This program will read an input file containing data from previous  

* traverse positions. It will then sample new information for the  

* current traverse position. Then it will write all the traverse  

* positions' data back to the original file. Finally it will traverse  

* the probe to a new location.  

* CHANNEL 2 ----> Contaction Pressure Transducer  

* CHANNEL 3 ----> Thermocouple  

* CHANNEL 4 ----> Total wake Pressure Transducer  

* CHANNEL 5 ----> Static wake Pressure Transducer  

* integer*2 basadr,dmalev,intlev,intype,sch,jch,nch,nsapch,range(8),func  

* integer*i2 real vevent(500),vvc(500),vpw(500),vpsw(500),gain(500)  

* real patm,temp,rapp,vvento,vcc0,v(8),em(8),frepch  

* character*40 date  

*****  

* read in data from previous traverse positions  

* open(unit=8,file='cond.out',status='old')  

* read(8,(a40)) date  

* read(8,(a40)) datt  

* read(8,*),temper  

* read(8,*),rapp  

* read(8,*),vvento  

* read(8,*),vcc0  

* read(8,*),vpw0  

* read(8,*),vpsw0  

* do 10 i=1,500  

* read(g,*),end=50) hwpos(i),motor(i),vvent(i),vcc(i),vpw(i),vpsw(i)  

* 10 continue  

* 50 if(i.eq.1)then  

* else  

* numpos=i  

* endif  

* close(unit=8)  

* note that a(3) is for channel 2, a(4) is for channel 3...  

* set DASH-16 calibration constants for +/- 5V range  

* open(unit=7,file='board.dat',status='old')  

* read(7,*),sch,jch,nsapch  

* read(7,*),frepch  

* read(7,*),range(2),range(3)  

* read(7,*),range(1),range(2),range(3)

```

*Pilot hole for*

```

        open(unit=8,file='cond.out',status='old')
* write new cond.out output file including the new traverse position data
*2
        c  pause Press <enter> to continue
        print*,chan.5 = ,v(6)
        print*,chan.4 = ,v(5)
        print*,chan.3 = ,v(4)
        print*,chan.2 = ,v(3)
        print*,chan.1 = ,v(2)
        print*,chan.0 = ,v(1)
        print*
        v(4)=vtc(numpos)
        read*,vtc(numpos)
        print*,Please enter thermocouple Mv:
        edit
        motor(numpos)=0
        if(numpos.eq.1)then
        hwp0s(numpos)=numpos
        vpsw(numpos)=v(6)
        vptw(numpos)=v(5)
        vtc(numpos)=v(4)
        vvenut(numpos)=v(3)
        call vmean(em,v,sch,fch,nch,nsapch,frepch,itype,iter)
        * voltages for the current traverse position
        * sample Venutri contraction, thermocouple, Protalwake, and Pstalcwake
        *2
        call vmean(em,v,sch,fch,nch,nsapch,frepch,itype,iter)
        * voltages for the current traverse position
        * sample Venutri contraction, thermocouple, Protalwake, and Pstalcwake
        ENDIF
        stop
        PRINT*,must be less than 32,760.
        PRINT*,i.e. No. of samples per channel x No. of channels,
        PRINT*,total no. of samples must not exceed 32,760.
        IF(TOTSAMP.GT.32760) THEN
        TOTSAMP=NCH*NSAPC
        * Total number of samples = no. of channels x no. samples per channel
        nch = fch-sch+1
        itype = 0
        * set sampling information
        call admitt(basadr,dmalev,inlev,rinle)
        * initialize DASH-16 board
        close(unit=7)
        70  continue
        read(7,*),a(i),b(i)
        do 70 i=1,8
        read(7,*),irange(7),irange(8)
        read(7,*),irange(4),irange(5),irange(6)

```

```

if(ans.eq.6)then
gain(numpos)=1.997174
elseif(ans.eq.10)then
gain(numpos)=3.159860
elseif(ans.eq.12)then
gain(numpos)=3.981072
elseif(ans.eq.16)then
gain(numpos)=6.309573
elseif(ans.eq.20)then
gain(numpos)=10.001598
elseif(ans.eq.26)then
gain(numpos)=19.952623
elseif(ans.eq.30)then
gain(numpos)=31.622777
elseif(ans.eq.34)then
gain(numpos)=50.118723
elseif(ans.eq.36)then
gain(numpos)=63.095734
elseif(ans.eq.40)then
gain(numpos)=100.00000
elseif(ans.eq.42)then
gain(numpos)=125.89254
elseif(ans.eq.46)then
gain(numpos)=125.89254

```

```

c ANS=10
read*,ANS
print*
print*, "-----> USER INPUT GAIN VALUE"
print*, 0,"-----> "
print*, 6 dB -----> 1.997174 gain
print*, 10 dB -----> 3.159860 gain
print*, 12 dB -----> 3.981072 gain
print*, 16 dB -----> 6.309573 gain
print*, 20 dB -----> 10.001598 gain
print*, 26 dB -----> 19.952623 gain
print*, 30 dB -----> 31.622777 gain
print*, 34 dB -----> 50.118723 gain
print*, 36 dB -----> 63.095734 gain
print*, 40 dB -----> 100.00000 gain
print*, 42 dB -----> 125.89254 gain
print*, 46 dB -----> 199.52623 gain
print*, 52 dB -----> 398.10717 gain
print*, 56 dB -----> 630.95734 gain
print*, 60 dB -----> 1000.00000 gain
elseif(ans.eq.6)then
gain(numpos)=1.997174
elseif(ans.eq.10)then
gain(numpos)=3.159860
elseif(ans.eq.12)then
gain(numpos)=3.981072
elseif(ans.eq.16)then
gain(numpos)=6.309573
elseif(ans.eq.20)then
gain(numpos)=10.001598
elseif(ans.eq.26)then
gain(numpos)=19.952623
elseif(ans.eq.30)then
gain(numpos)=31.622777
elseif(ans.eq.34)then
gain(numpos)=50.118723
elseif(ans.eq.36)then
gain(numpos)=63.095734
elseif(ans.eq.40)then
gain(numpos)=100.00000
elseif(ans.eq.42)then
gain(numpos)=125.89254
elseif(ans.eq.46)then
gain(numpos)=125.89254

```

```

write(g,*),date
write(g,*),pattm
write(g,*),temper
write(g,*),rapp
write(g,*),vvenm0
write(g,*),vcco
write(g,*),vpw0
write(g,*),vpswo

```

80

print\*,Please enter GAIN"

```

      END
      RETURN
      330 FORMAT(4F15.5)
      320 FORMAT(4F15.5)
      300 FORMAT(//,9X, No.,9X, Ch.1,9X, Ch.2)

      DO 50 J=1,NCH
        V(J)=B(SCH+J)*E(J)+A(SCH+J)
      50

      40 CONTINUE
      IF(IPRINT.EQ.1) WRITE(6,330) I,IE(I),J=1,NCH
      45 E(J)=E(J)+READ(IE(J)-E(J)/real(I)
      IE(J)=ICOUNT(INDEX+J)
      DO 45 J=1,NCH
        INDEX=(I-1)*NCH
      40 I=1,NSPCH
      IF(IPRINT.EQ.1) WRITE(6,300)
      IPRINT=0

      20 E(J)=0.0
      DO 20 J=1,NCH
        CALL SAMPLE(clock,SCH,FCH,NCH,NSPCH,FRPCH,ICOUNT,ITYPE,mode,free
$ct)
        mode =17
        DATA clock/1.e6/
        DIMENSION IE(8),E(8),V(8)
        COMMON A(8),B(8)
        integer MODE
        integer NCH,SCH,FCH,NSPCH
        INTEGER*2 ICOUNT(10000)
        SUBROUTINE VMEAN(E,V,SCH,FCH,NCH,NSPCH,FRPCH,ITYPE,ITER)
*-----*
        100 continue
        $ini()
        write(8,*),hwpos(i),motor(i),vvenet(i),vtc(i),vpfw(i),vpsw(i),ga
        do 100 i=1,numpos
        print*
        edit*
        read*,gain(numpos)
        print*,Enter GAIN: '
        else
        goto 80
        read*,gain(numpos)
        print*,'
        elseif(ans.eq.0)then
        gain(numpos)=398.10717
        elseif(ans.eq.52)then
        gain(numpos)=199.52623
        elseif(ans.eq.1)then
        gain(numpos)=199.52623
        endif
        close(unit=8)
        end
      
```

```

        integer*2 mode,param(16),flag
        integer*2 basadr,dmaslev,imlev
*****
* NOTE: The computer code must be linked to the library: dasg.lib
*****
* Use delay loops inside the stepping loop to control motor speed.
* This completes 1 step in the +X direction. Use a loop for many steps.
* call dasg(mode,param,flag)
param(1)=3
*
*
*
0 0 1 1 ---> 2A0 = 3
OP3 OP2 OP1 OP0
*
*
*
Now finish the step by bringing OP1 back up to high.
call dasg(mode,param,flag)
param(1)=1
*
*
*
0 0 0 1 ---> 2A0 = 1
OP3 OP2 OP1 OP0
*
*
*
the motor to step in the +X direction, we need to cause OP1 to go low.
to step, send a low signal to one of the channels. For instance, to cause
* Now both output channels (0 and 1) will see +5 volts. To cause the motor
* call dasg(mode,param,flag)
param(1)=3
*
*
*
0 0 1 1 ---> 2A0 = 3
OP3 OP2 OP1 OP0
*
*
*
will send +5V to both output channels.
first of all send voltage to both digital outputs OP0 and OP1. This
* to the digital outputs. The Maxwell box operates ACTIVE LOW, so
* Thus to step the motor, use mode 13 of the DASH-16 to send pulses
*
*
GND ---> pin 1 (logic ground)
GND ---> pin 8 (X motor enable)
OP0 ---> pin 6 (X single step -)
OP1 ---> pin 7 (X single step +)
+5V ---> pin 2 (+5V logic power)
*****
DASH-16 outputs ----> Maxwell Parallel I/O pin
* Box Parallel I/O port:
* DASH-16 output writing to Maxwell Stepping Motor Controller (SMC-102A)
*
param(1)=1 will drive motor one direction
*
param(1)=2 will drive motor in other direction
*****
* DASH-16 digital outputs.
* This program will drive the traverse stepping motor by using the
*****
program trav100
*****
```

*Trav100 for*

```

        call fdatasg(mode,param,flag)
param(1)=3

*** and thus complete the step
*** setting param(1)=3 will cause both digital outputs 0 and 1 to see +5V
*****
50    continue
print*,TRaversing Probe ("shortening") ...
do 50 j=1,4
* internal delay loop controlling motor speed

ENDIF

PRINT*,FLAG=,FLAG
PRINT*,INDEXING ERROR HAS OCCURRED
IF (FLAG.NE.0) THEN
call fdatasg(mode,param,flag)
param(1)=1

* output 1 will be pulsed from high to low. This leads to a +X step.
* while causing digital output 1 to go to zero volts. Thus digital
* setting param(1)=1 will cause digital output 0 to remain at +5V
DO 105 I=1,steps
*** index traverse ----- param(1)=1 will "shorten" entire setup
*****
endif
pause
print*,FLAG=,FLAG
if(flag.ne.0)then
call fdatasg(mode,param,flag)
param(1)=3
param(1)=3

*** send +5V to digital outputs 0 and 1 to establish "high" reference
mode=13

*** set mode to write to digital outputs of DASH-16
call fdatasg(mode,param,flag)
param(3)=dmalev
param(2)=imdev
param(1)=basadr
mode=0

*** initialize DASH-16 board
data basadr,dmalev,imdev,clock/816,3,5,1.066/
parameter(steps=100)

integer i,hwpos(500),motor(500),steps,numpos
real vvenet(500),vtc(500),vpbw(500),vpbsw(500),gain(500)
real param,temper,fapp,vvenet,vtc,vptwo,vpswo
character*40 date

```

```

* internal delay loop controlling motor speed
* update COND file with motor counts for new position that was just moved to
* read in data from previous traversing probe ("shortening") ...
*****105 CONTINUE*****
60 continue
do 60 j=1,4
print*,Traversing probe ("shortening") ...
60 continue
* internal delay loop controlling motor speed
* update COND file with motor counts for new position that was just moved to
* read in data from previous traversing probe ("shortening") ...
*****105 CONTINUE*****
105 continue
read(8,*),vpsw0
read(8,*),vptw0
read(8,*),vtemp
read(8,*),patm
read(8,*),fapp
read(8,*),vmeto
read(8,*),vccl
read(8,*),vpsw
read(8,*),vptw
read(8,*),vtemp
read(8,*),patm
read(8,*),fapp
read(8,*),vmeto
read(8,*),vccl
read(8,*),vpsw0
read(8,*),vptw0
write(8,*),vtemp
write(8,*),vmeto
write(8,*),vccl
write(8,*),vpsw0
write(8,*),vptw0
write(8,*),fapp
write(8,*),temper
write(8,*),patm
write(8,*),date
open(unit=8,file='cond.out',status='old')
* write new cond.out output file including the new traverse position data
motor(numpos)=motor(numpos-1)+steps
hwpos(numpos)=0
vmeto(numpos)=0
vccl(numpos)=0
vptw(numpos)=0
vpsw(numpos)=0
vtemp(numpos)=0
patm(numpos)=0
fapp(numpos)=0
gain(numpos)=0.0
vpsw(numpos)=0.0
vptw(numpos)=0.0
vccl(numpos)=0.0
vtemp(numpos)=0.0
date('a40') date
open(unit=8,file='cond.out',status='old')
* write new cond.out output file including the new traverse position data
200 continue
$ini()
write(ga,*) hwpos(i),motor(i),vmeto(i),vccl(i),vptw(i),vpsw(i),ga
do 200 i=1,numpos
write(ga,*) vpsw0
write(ga,*) vptw0
write(ga,*) fapp
write(ga,*) temper
write(ga,*) patm
write(ga,*) date
open(unit=8,file='cond.out',status='old')
* write new cond.out output file including the new traverse position data
210 continue
c print*
print*,Start Delay Loop...
close(unit=8)
210 continue
print*,End Delay Loop...
end

```

```

double precision sum,sum2,avgvel,avolt,avel,avgvolt,msavel
double precision sum,sum3,voltt,avgvt,a(g),b(g),c(l),d(l)
integer tt(61)
real aa,bb,vt(61)
REAL *8 PI
REAL *8 X,XX,X2
character*1 elem
character*2 tpchar
character*3 tpeap
character*40 date
CHARACTER*30 raw,fft,fdoc,hwcal,fcond,fout,input,fdad

```

PARAMETER (M=2048,MH=M/2)

\$LARGE

---

```

* UNT 4 --> TEMPORARY FILE
*
* UNT 13 --> WRITING VELOCITY FLUCTUATIONS FOR USE BY DADISP TO FFT
*
* UNT 12 --> WRITING HWLOC,UMEAN,UMEAN/UMF,URMS
*
* UNT 9 --> WRITING CALCULATED VELOCITY, RE,...,also Cd
*
* UNT 3 --> WRITING DOC INFORMATION
*
* UNT 2 --> WRITING FFT INFORMATION
*
* UNT 14 --> READING K-TYPE THERMOCOUPLE CHART
*
* UNT 11 --> READING HOT WIRE CALIBRATION FILE
*
* UNT 10 --> READING IN DATA FILE CONTAINING RAW COUNT VALUES
*
* UNT 8 --> READING TEST CONDITIONS FOR EACH TRAVERSE POSITION
*
* UNT 7 --> READING TUNNEL AND BOARD CALIBRATION INFORMATION
*
* UNT 5 --> READING SAMPLING INFORMATION
*
* The following unit numbers are used in this code.

```

CHANNEL 1 --> FLOW FLUCTUATIONS (AMPLIFIED)

CHANNEL 0 --> MEAN FLOW

When data were taken, the following channels were used.

Note: The file containing the hot-wire calibration constants  
must be called "hwcal.cal".

calculated for current experimentation.  
needs to be done for this to occur. (Cd not  
an integration technique; a little work  
This program also will calculate Cd by  
velocities, as well as flow conditions.  
and calculate mean and fluctuation  
acquired during hot-wire experimentation  
HWREDUCE.FOR : This program will take the raw data

---

program hwreduce

*HWreduce for*

\* slope ---> Pa/Pa -----> PSTATIC vs contraction drop

\* tensile ---> Pa/Volt -----> Venturi PRESSURE TRANSDUCER slope

\* tensile ---> Pa/Pa -----> TUNNEL DYNAMIC vs contraction drop

\* Note:

\*\*\* read tunnel and board calibration information

close(unit=14)

2 format(12.16,3)

read(14,2)(n(i),w(i),i=1,61)

open(unit=14,file='chark.dat',status='old')

\*\*\* Read K-Type Thermocouple Chart

close(unit=11)

read(11,\*)(c1(j),j=1,nlp1)

nlp1=n1+i

read(11,\*), n1

open(unit=1,file='hwcal',status='old')

\*\*\* Read hot wire calibration file

read(5,(220)'hwcal

read(5,\*), k,freqch,npnts

\* that I must loop to in order to read all raw data

\* is divided by 2 since I sampled 2 channels to obtain the number

\* note that npnts is the total number of samples taken...later it

open(unit=5,file='input',STATUS='OLD')

input='e://elem//inp//freqap//inp'

\*\*\* read control parameters

read(0,'(a3)') freqap

print\*, 'Enter APPLIED FREQUENCY (3 digits)'

read(0,'(a1)') elem

print\*, 'Enter ELEMENT #'

\*\*\* user enters information

chord=0.3048

pi =acos(-1.0)

HANWIN(j) =0.5\*(1.-COS(2.\*PI\*real(j-1)/real(M-1)))

DIMENSION XX(M)

DIMENSION XM(M), X2(M), WINDOW(M)

DIMENSION FXX(M)

COMPLEX\*16 RX(M),FX2(M)

integer count,k,numhw,hotpos(200),motor(200)

integer ij,jl,npnts,counts,m,l,nlp1,hwpos(200),lopos,traps

double precision dw

real deltw

real ptw(200),psw(200),psi(200),cd,tol,qin(200)

real freqch,vptw,vpsw0,offset,mach,reach,maave

real slope,rho,venstl,tunstl,veini,re,chord,ui

real fapp,vvenstl,vct0,paltm,dint,mu,temperr,psloc,velloc

real fapp,vvenstl,vct0,paltm,dint,mu,temperr,psloc,velloc

real fapp,vvenstl,vct0,paltm,dint,mu,temperr,psloc,velloc

```

*    777 or static-patm vs contraction drop777
*      ptwslp ---> Pa/volt -----> Static/wake PRESSURE TRANSDUCER slope
*      pswslp ---> Pa/volt -----> Static/wake PRESSURE TRANSDUCER slope
*      slope ---> deg/K/volt ---> THERMOCOUPLE slope
*      open(unit=7,file='calib.dat',status='old')
*      read(7,*),binslp,venslp,pslode
*      read(7,*),ptwslp,pswslp,tslope
*      read(7,*),read(pslode,pswslp)
*      * read in wake traverse single step increment {meters per count}, distance
*      * between Pitot-Static probe and hotwire {meters}, and
*      * tolerance {XXXXXXXXXXXXXX777777}
*      * read in board calibration constants
*      * do 3 i=1,8
*      * read(7,*),a(i),b(i)
*      * continue
*      * Note: I don't need to read the IRANGE() values that tell the DAS20
*      * the individual channel gains since I'm not sampling in this code. I'm
*      * only doing data reduction.
*      * read in the traverse position values at which HW data were taken
*      * only doing data reduction.
*      * read(7,*),end=7) hotspos(i)
*      do 5 i=1,1000
*      continue
*      5   numhw=i-1
*      read(7,*),end=7) hotspos(i)
*      do 5 i=1,1000
*      continue
*      3   continue
*      read(7,*),a(i),b(i)
*      do 3 i=1,8
*      read(7,*),dw,offset,tof
*      * read in board calibration constants
*      * read in wake traverse single step increment {meters per count}, distance
*      * between Pitot-Static probe and hotwire {meters}, and
*      * tolerance {XXXXXXXXXXXXXX777777}
*      * read in board calibration constants
*      * only doing data reduction.
*      * read(7,*),end=7) hotspos(i)
*      do 5 i=1,1000
*      continue
*      *** read test conditions for each traverse position
*      open(unit=8,file='cond.dat',status='old')
*      read(8,*),con
*      read(8,*),vtemp
*      read(8,*),vapp
*      read(8,*),vvent0
*      read(8,*),vcco
*      read(8,*),vpriwo
*      read(8,*),vpsswo
*      read(8,*),j=1,200
*      do 10 j=1,200
*      topsos=0
*      read(8,*),vpsswo
*      read(8,*),vpriwo
*      read(8,*),vcco
*      read(8,*),vvent0
*      read(8,*),vapp
*      read(8,*),temper
*      read(8,*),patm
*      read(8,*),data
*      open(unit=8,file='cond.dat',status='old')
*      read(8,*),con
*      read(8,*),vtemp
*      read(8,*),vapp
*      read(8,*),vvent0
*      read(8,*),vcco
*      read(8,*),vpriwo
*      read(8,*),vpsswo
*      read(8,*),j=1,200
*      do 10 j=1,200
*      topsos=0
*      read(8,*),vpsswo
*      read(8,*),vpriwo
*      read(8,*),vcco
*      read(8,*),vvent0
*      read(8,*),vapp
*      read(8,*),temper
*      read(8,*),patm
*      read(8,*),data
*      close(unit=8)
*      continue
*      10
*      **** ANALYZE THE WAKE DEFICIT ****
*      ****
*      * open output file that will contain calculated velocity, Re ... values
*      * write(*,*)'traps psloc velem mre rho tru mu psw ps
*      * open(unit=9,file='fout',status='unknown')
*      * fout=e//elem//out//fredep//.out
*      * finf
*      * reavg=0.0
*      * mavg=0.0

```

```
maaveg=maaveg+mach
```

```
    $,2x,f9.8,(2x,f8,1))  
40   format(1x,i2,2x,f8.6,2x,2(f5.2,2x),f5.3,2x,f7.0,2x,f5.3,2x,f6.2  
$trapos),psw(trapos),psiin(trapos)  
write(9,40) trapos,psloc,velin,velloc,mach,re,rho,int,mu,pwtr  
*** write information for current traverse position to output file  
psloc=real(motor(trapos))*dw  
c   psloc=real(trapos-1)*dw  
* find Pilot-Static probe location  
c   psiin(trapos)=(vvenit(trapos)-vvent0)*venslp*pslope + patm  
* find P static infinty  
c   velloc=sqr(2*(pwtr(trapos)-psw(trapos))/rho)  
* find vlocat  
c   psw(trapos)=(vpsw(trapos)-vpsw0)*pswslp + patm  
* find Psticwake  
c   pwtr(trapos)=(vpw(trapos)-vpw0)*pwslp + patm  
* find Ptotawake  
print* mach=velinf/sqr(1.4*287.0*int)  
* find Mach number  
re=(rho*velinf*chord/mu)  
* find Reynolds number  
velinf=sqr(2.0*qinf(trapos)/rho)  
qinf(trapos)=(vvenit(trapos)-vvent0)*venslp*venslp  
* find dynamic pressure and dispersed in SI units  
rho=patm/(287.0*int)  
* find air density in SI units  
mu=0.000018*(int/293.15)**1.5*(403.15)/(int+110.0)  
* find air viscosity in SI units using Sutherland's law  
int=inf+273.15  
c convert int from Celsius to Kelvin  
int=aa*bb+float(int))  
bb=float((int+1))-float(int))  
aa=(vtc(trapos)-vt(i))/(vt(i+1)-vt(i))  
35 continue  
30 continue  
if(vtc(trapos).ge.vt(i).and.vtc(trapos).lt.vt(i+1))goto 35  
do 30 i=1,60  
c   vtc(trapos)=vtc(trapos)/630.9573445  
* correct for gain on thermocouple (56 dB)  
c   temp=temper+tslope*(vtc(trapos)-vtc))  
c   int=temper+temp  
* find temperature in Kelvin  
*** calculate tunnel velocity, Re, ... for current traverse position  
do 50 trapos=1,totpos  
*** begin loop over all traverse positions in wake
```

```

        if(traps[i].l0) ifchar(i;i)=0,
        close(unit=4)
        read(4,(a2) ifchar
        rewind(unit=4)
        write(4,48) traps
        open(unit=4,file='temp.tem',status='unknown')
        format(12)
        48
        hwooc=real(motor(traps))*dw-offset
        traps=hotos(i)
        do 1000 i = 1,numhw
        open(unit=12,file='profile.pro',status='unknown')
        *
***** ANALYZE THE FREQUENCY CONTENT *****
*****
        close(unit=9)
        47  format(lx,a,f5.3)
        46  format(lx,a,f7.0)
        45  format(lx,a,f8.6)
        write(9,47)'Average Mach -----> ',mavge
        write(9,46)'Average Re -----> ',reave
        c   write(9,45)'Coefficient of Drag ---> Cd = ',cd
        write(9,*)
        write(9,*)
        7777  continue
        call wake(ptw,psw,psi,cd,dinl,tol,deltw,chord,topos)
        deltw=dw*40.
        =====
        c   THE CODE
        c   FOR EXAMPLE,40. MAYBE MAKE THIS A PARAMETER IN THE BEGINNING OF
        c   DISTANCE,DW, TIMES THE # OF STEPS BETWEEN EACH WAKE POINT,
        c   DISTANCE,BETWEEN EACH WAKE POINT WHICH FOR ME IS THE SINGLE STEP
        c   MAKE SURE EVERYTHING IS DEFINED RIGHT. THE DELTW I THINK IS THE
        c   ***** IS C (chord) IN INCHES? MY CHORD IN METERS.
        * 99999
        *77777
        cc this section to calculate Cd needs a little work
*** call subroutine to calculate Cd
        mavge=mavge/real(topos)
        reave=reave/real(topos)
        50  continue
        reave=reave+re

```

```

do 170 j = 1,npnts/2
open(unit=13,file=fread,status='unknown')
fread=e//elem//tpchar//f//fredep//.dat

SUM4=0.0
rmsvel=0.0
sum3=0.0

read(10,*)
read(10,*)

rewind(unit=10)
print*, 'Calculating TL..'
print*
* Find fluctuation velocity value
*** Calculate Turbulence Intensity
c      print*, 'Amplified Fluctuation DC offset = ',avgvl,' volts'
print*
print*, 'Mean velocity = ',avgev,' m/s'
avgvlt=avgvl/real(npnts/2)
avgvel=avgvl/real(npnts/2)
sum=0.0
sum2=0.0
sum+=avgev
avgvl=avgvl+voltl
voltl=a(2)+b(2)*real(countl)
* calculate offset amplified voltage of fluctuation
sum2+=avgvl
sum+=avgvl
avgvl=avgvl/voltl
100 continue
100 continue
90 continue
90 do jj=2,ninp1
      ave=avvel+c(jj)*avolt*(jj-1)
      avg=c(jj)
      avolt=(a(1)+b(1)*real(countm))
      read(10,*)
      countm, countl
      do 100 j = 1,npnts/2
            read(10,*)
            read(10,*)

            sum=0.0
            sum2=0.0
            avgvel=0.0
            avgvl=0.0
            * Mean Velocity calculation & amplifier offset DC voltage calculation
            print*, 'Calculating Mean Hot Wire Velocity..'
            * raw data file has 2 columns: mean flow counts, fluctuation flow counts
            print*, 'Raw data file contains: mean flow counts, fluctuation flow counts
            *** Find Umean and do FFT
            open(unit=10,file=raw,status='old')
            print*, raw
            raw=e//elem//tpchar//f//fredep//.raw
            *** open data file containing raw counts from DAS board

```

```

170    continue
      sum3=sm3+avol*avel
      write(13,*),real(avol)
      sm3=sm3+avol*avel
      close(unit=13)
      PRINT*, 'AVERAGE OF FLUCTUATIONS: ',SUM4/REAL(NPTS/2)
170    continue
      msvel=sqr(sum3/real(npts/2))
      * find temperature in Kelvin
      tinf=tinf+273.15
      rho_pam=(287.0*ninf)/ninf
      * find air density in SI units
      ninf=ninf+273.15
      rho=rho*(rho/ninf)
      * find air speed in SI units
      velinf=sqr(2.0*qinf(rho)/rho)
      * find turbulence intensity
      u=u*msvel/velinf
      print*,TT=,u*100.,percent
      print*, 'Print*,average volts = ,avgl
      print*, 'rms Velocity = ,rmsvel
      print*, 'Print*,rmsvel/volinf
      write(12,190) hvolc,avgvel,avgvel/volinf,rmsvel/rmsvel/volinf
190    format$(lx,ly,s))

```

```

250    CONTINUE
       XX(j)=avel
       avel=avel-avgvel
* find fluctuation velocity
260    continue
       avel=avel+c1(j)*avolt**((j)-1)
       do 260 jj=2,nlp1
          avel=c1(j)
* find instantaneous velocity
          avolt=avolt+avgvt
* add fluctuation volts to average volt value
          avolt=avolt/gain(traps)
* reverse gain to obtain actual voltage of fluctuation
          avolt=avolt-avgvt
* correct for DC shift due to amplification of DC tackle through filter
          avolt=a(2)+b(2)*real(count)
* find offset amplitude voltage of fluctuation
          IT=IT+1
          read(10,*), countm, countl
DO 250 j=1,MH
      IT=0
      WRTE(0,*), BEGIN FFT
220    CONTINUE
      FXX(j)=(0.0,0.0)
DO 220 j=1,M
      DO 220 j=1,M
          open(unit=3,file=fdoc,status='unknown')
          fdoc='e//elem//tpchar//f//fredep//.doc'
          open(unit=2,file=fft,status='unknown')
          fft='e//elem//tpchar//f//fredep//.fft'
* prepare output files
          rewmid(unit=10)
          read(10,*)
          read(10,*)
          read(10,*)
DO 210 j=1,M
      SUMW=SUMW+WINDOW(j)**2
      CONTINUE
      DEN=real(k*M*M)*FACT
      FACT=SUMW/REAL(M)
210    CONTINUE
      DO 210 j=1,M
          SUMW=0.0
200    CONTINUE
          WINDOW(j)=HANWIN(j)
          DO 200 j=1,M
* calculate window weighting factor
          NTOTAL=(K+1)*MH
          DELTAF=1./FREPCH
          DELTAF=FREPCH/REAL(M)
          OLD=FREPCH/2.
* calculate frequency bin
          *** PERFORM FFT

```

```

260      KK=0
DO 300 IK=1,K
      DO 265 J=1,MH
CONTINUE
      X0=XX(J)
      DO 275 J=1,MH
CONTINUE
      IT=IT+1
      read(10,*), countm, countd
      * Find offset amplitude voltage of fluctuation
      avolt=a(2)+b(2)*real(countd)
      * correct for DC shift due to amplification of fluctuation
      avolt=avolt-avgvlt
      * reverse gain to obtain actual voltage of fluctuation
      avolt=avolt/gain(traps)
      * add fluctuation volts to average volt value
      avolt=avolt+c1(j)*avolt***(j-1)
      do 270 jj=2,npl
      ave=c1(jj)
      * find instantaneous velocity
      ave=ave+c1(j)*avolt***(j-1)
      270 continue
      ave=ave-avgvel
      * find fluctuation velocity
      XX(J)=ave
      275 CONTINUE
      WRTE(0,*),IK,IT
      DO 280 J=1,MH
CONTINUE
      XG+MH)=XX(J)
      DO 290 J=1,M
CONTINUE
      X0=X(J)*WINDOW(J)
      DO 295 J=1,M
CONTINUE
      FXX(J)=FXX(J)+CONJG(FX(J))*FX(J)
      CALL TWOFRT(X,X2,FX,FX2,M)
      DO 295 J=1,M
CONTINUE
      WRTE(3,330) FDOC
      WRTE(3,340) FRPCH,IT,K
      WRTE(3,350) traps,hwloc,avgvel,rmsvel,it*100.
      * write to FFT output file
      DO 320 J=1,MH
CONTINUE
      GXX=2.0*FXX(J)/DEN/DELTAF
      AGXX=10.0*ALOG10(CABS(GXX))
      F=(real(j-1))*DELTAF
      WRTIE(2,310) F,AGXX,GXX
      * write to DOC output file
      320 CONTINUE
      AS=0.

```





```

      END
      RETURN
12 CONTINUE
      FFT2(N2-J)=CONJG(H2)
      H2=F2(J)-H2
      FFT1(N2-J)=CONJG(H1)
      H1=F1(J)-H1
      H2=C2*(FFT1(J)+CONJG(FFT1(N2-J)))
      H1=C1*(FFT1(J)+CONJG(FFT1(N2-J)))
      DO 12 J=1,N/2+1
      c
      N2=N+2
      *
      c
      FFT1(N+1)=FFT1(1)
      *
      c
      FFT1(1)=CMPLX(REAL(FFT1(1)),0.0)
      FFT2(1)=CMPLX(AIMAG(FFT1(1)),0.0)
      *
      CALL FOUR1(FFT1,N,1)

11 CONTINUE
      FFT1(J)=CMPLX(DATA1(J),DATA2(J))
      DO 11 J=1,N
      C2=CMPLX(0.0,-0.5)
      C1=CMPLX(0.5,0.0)
      COMPLEX*16 FFT1(N),FFT2(N),H1,H2,C1,C2
      REAL*8 DATA1(N),DATA2(N)

* from Press et al., 1992
      SUBROUTINE TWOFFT(DATA1,DATA2,FFT1,FFT2,N)
      *
      end
      return
      cd = 2.*cd/c
      *
      *55555555555555555555555555555555555555555555555555555555555555555555
      *
      do n = 1, w, 1
      cd = cd + cd(i)*dw + .5*dw*(cd(i+1) - cd(i))
      cd = 0.0
      *
      *5555555555555555555555555555555555555555555555555555555555555555555555
      *Comment 5: Integrate to determine the large coefficient
      *
      *5555555555555555555555555555555555555555555555555555555555555555555555555555555
      *
      *444444444444444444444444444444444444444444444444444444444
      enddo
      *
      do n = 1, w, 1
      cd(i) = cd(i) - cdoff
      cd(i) = cd(i) - (n-1)*dw, cd(i)
      write(17,*), (n-1)*dw, cd(i)
      c
      *44444444444444444444444444444444444444444444444444444444444444444444444444
      enddo
      *
      do n = 1, w, 1
      cd(i) = cd(i) - cdoff
      cd(i) = cd(i) - (n-1)*dw, cd(i)
      write(17,*), "this is corrected cd"
      c
      write(17,*), "this is corrected cd"

```

\* from Press et al., 1992  
SUBROUTINE FOURI(DATA,NN,ISIGN)

REAL\*8 WR,WI,WPR,WPI,WTEMP,THETA,data

\* dimension data(\*)

N=2\*NN

j=1

DO 11 I=1,N,2

IF(GT,I)THEN

TEMPR=DATA(j)

DATA(j)=DATA(j+1)

TEMP1=DATA(j+1)

DATA(j)=DATA(j)

DATA(j+1)=DATA(j+1)

DATA(j)=TEMPR

DATA(j+1)=TEMP1

ENDIF

M=N/2

j=j+M

IF (N.GT.MAX) THEN

MAX=2

IF (N.LT.MAX) THEN

ISTEP=2\*MAX

WR=1.0D0

WP=DSIN(THETA)

THETA=6.28318530717959D0/(ISIGN\*MAX)

WPR=-2.0D0\*DSIN(0.5D0\*THETA)\*\*2

WP=DSIN(THETA)

WR=1.0D0

WP=2.0D0\*DSIN(0.5D0\*THETA)\*\*2

THETA=6.28318530717959D0/(ISIGN\*MAX)

ISTEP=2\*MAX

WR=1.0D0

WP=DSIN(THETA)

THETA=6.28318530717959D0/(ISIGN\*MAX)

WP=2.0D0\*DSIN(0.5D0\*THETA)\*\*2

THETA=6.28318530717959D0/(ISIGN\*MAX)

WP=DSIN(THETA)

WR=1.0D0

WP=2.0D0\*DSIN(0.5D0\*THETA)\*\*2

THETA=6.28318530717959D0/(ISIGN\*MAX)

- Ahuja, K., K. Whitkey, R. R., and Jones, G. S., "Control of Turbulent Boundary Layer Flows by Sound," AIAA Paper 84-2298, Oct. 1984.
- Ahuja, K., K. Whitkey, R. R., and Jones, G. S., "Control of Flow Separation by Sound," AIAA Paper 83-0726, 1983.
- Aitnauis, D., and Wuerz, W., "Wind Tunnel Tests of the SM701 Airfoil," Institut Für Aerodynamik Und Gasdynamik, Universität Stuttgart, Germany, Jun. 1991.
- Andbar, M., "Clinical Applications of Computerized Thermography," In NASA, Baldwin, J. T., Tabrell, J. M., Deutsch, S., and Geselowitz, D. B., "Wall Shear Stress Measurements Within an Artificial Heart Ventricles," 1987 IEEE Engineering in Medicine and Biology Ninth Annual Conference, Vol. 3, 1987, pp. 1189-1191.
- Bar-Sever, A., "Separation Control on an Airfoil by Periodic Forcing," AIAA Journal, Vol. 27, Jun. 1989, pp. 820-821.
- Becker, H. A., and Massaro, T. A., "Vortex Evolution in a Round Jet," *J. Fluid Mechanics*, Vol. 31, 1968, pp. 435-448.
- Bellhouse, B. J., and Schultz, D. L., "Determination of Mean and Dynamic Skin Friction, Separation and Transition in Low-Speed Flow with a Thin-Film Heated Element," *J. Fluid Mechanics*, Vol. 24, part 2, 1966, pp. 379-400.
- Bossetti, C., "Experimental Investigation of the Effects of Windward Surface Devices on the Primary Vortices of an Aspect Ratio 1.0 Delta Wing," Master's Thesis, The Pennsylvania State University, Department of Aerospace Engineering, 1995.
- Bradshaw, P., and Wong, F. Y. F., "The Reattachment and Relaxation of a Turbulent Shear Layer," *J. Fluid Mechanics*, Vol. 52, 1972, pp. 113-135.
- Brown, G. L., and Roshko, A., "On Density Effects and Large Structure in Turbulent Mixing Layers," *J. Fluid Mechanics*, Vol. 64, 1974, pp. 775-816.

## BIBLIOGRAPHY

- Brophy, C. M. *Turbulence Management and Flow Qualification of the Pennsylvania*. State University Low-Turbulence, Low-Speed, Closed-Circuit Wind Tunnel. Master's Thesis, The Pennsylvania State University, 1994.
- Brunn, H. H. *Hot-Wire Anemometry, Principles and Signal Analysis*. Oxford University Press, New York, 1995, pp. 234-235.
- Butter, D. J. "Recent Progress on Development and Understanding of High Lift Sytems." In AGARD Conference on Improvment of Aerodynamic Performance through Boundary Layer Control and High Lift Sytems, AGARD-CP-365, Brussels, Belgium, 1984, pp. 1-1 to 1-26.
- Camci, C. "Liquid Crystal Thermography." A book chapter published for the 1996 von Karman Institute Lecture series on Temperature Measurements, VKI-L-5-1996-09, Brussels, Belgium, Apr. 1996.
- Camci, C. "Liquid Crystal Thermography on the Rotating Surfaces of Turbomachinery Systems." A book chapter in *Advanced Turbomachinery Design*, ed. Chumill Hash, published by Marcel Dekker Inc., New York, 1996.
- Camci, C. "Liquid Crystal Thermography on the Fluid Solid Interface of Rotating Systems." *J. Heat Transfer*, Vol. 119, No. 1, Feb. 1997, pp. 20-29.
- Camci, C., Hippenssteel, S. A., and Poinsette, P. E. "Evaluation of a Hue Capturing Based Transient Liquid Crystal Method for High Resolution Mapping of Convective Heat Transfer on Curved Surfaces." *J. Heat Transfer*, Vol. 115, No. 2, May 1993.
- Camci, C., Kim, K., and Hippenssteel, S. A. "A New Hue Capturing Technique for the Quantitative Interpretation of Liquid Crystal Images Used in Convective Heat Transfer Studies." *J. Turbomachinery*, Vol. 114, No. 4, Oct. 1992, pp. 765-775.
- Carslaw, H. S. and Jaeger, J. C. *Conduction of Heat in Solids*. 2<sup>nd</sup> edition, Clarendon Press, Oxford, 1959.
- Castro, I. P. and Eppik, E. "Boundary-Layer Relaxation After a Separated Region." *Experimental Thermal and Fluid Science*, Vol. 13, n. 4, Nov. 1996, pp. 338-348.
- Centolaizza, L., Dunn, C., Papay, P., Park, D., Smith, R., and Thibodeau, T. "Composite Wind Tunnel Model Design." Senior project final report, The Pennsylvania State University, Department of Aerospace Engineering, May 1995.
- Chandrusda, C. and Bradshaw, P. "Turbulent Structure of a Reattaching Mixing Layer." *J. Fluid Mechanics*, Vol. 110, 1981, pp. 171-194.

- Chang, R. C., Hsiao, F. B., and Shyu, R. N., "Forcing Level Effects of Internal Acoustic Excitation on the Improvement of Airfoil Performance," *J. Aircraft*, Vol. 29, No. 5, Sept.-Oct. 1992, pp. 823-829.
- Chatigny, V. J., "Piezo Film Yields Novel Transducers," *Electronics Week* 57 (17), Aug. 6, 1984, pp. 74-77.
- Coe, D. J., Allen, M. G., Trautman, M. A., and Glezer, A., "Addressable Micromachined Jet Arrays," *The 8th International Conference on Solid-State Sensors and Actuators, and Euroensors IX*, Stockholm, Sweden, Jun. 25-29, 1995.
- Coe, D. J., Allen, M. G., Smith, B. L., and Glezer, A., "Micromachined Jets for Manipulation of Macro Flows," *Solid-State Sensor and Actuator Workshop*, Hilton Head, SC, Jun. 13-16, 1994.
- Colle, K. D., "Separation Detection with Stochastic Signals From Flush-Mounted Hot-Film Sensors," *Fluid Measurement and Instrumentation Forum*, Vol. 95, 1990, pp. 35-37.
- Cooper, T. E., Field, R. J., and Meyer, J. F., "Liquid Crystal Thermography and Its Application to the Study of Convective Heat Transfer," *J. Heat Transfer*, Aug. 1975, pp. 442-449.
- Crawford, M. E., and Kays, W. M. STANS - A Program for Numerical Computation of Two Dimensional Internal/External Boundary Flows, Stanford University, Dec. 1975.
- Department of Mechanical Engineering, Thermosciences Division, Report HMT-23, Control and Lift Enhancement on Airfoil Using Unsteady Excitations, ICAS Congress 18<sup>th</sup> Proceedings, Vol. 2, Beijing, China, Sept. 20-25, 1992.
- Cui, E. J., Yu, X. T., Fu, G. M., Xu, C., Zhang, S. Y., and Zhou, M. D., "Separation Detection Using Flush-mounted Hot-Film Gauges and Semiconductor Dynamic Pressure Transducers," AIAA Paper No. 82-0593, 1982.
- Daggenhart, J. R., and Stack, J. P., "Boundary Layer Transition Detection Using Flush-mounted Hot-Film Gauges and Semiconductor Dynamic Pressure Transducers," DISA Electronics. Instruction Manual DISA 55M System with 55M10 CTA Standard Bridge, DISA Information Department, Marina Del Rey, CA.
- Dwinnell, James H. *Principles of Aerodynamics*, 1st edition, McGraw-Hill Book Company, Inc., New York, 1949.
- Ewald, P. P., Pöschl, Th., and Prandtl, L. *The Physics of Solids and Fluids*. Blackie & Sons, Limited, 1936.

- Ferguson, J. L., "Liquid Crystals," *Scientific American*, Vol. 211, No. 2, 1964, pp. 76-85.
- Filtite, K. J. and Cover, E. E., "Unsteady Turbulent Skin-Friction Measurement in an Adverse Pressure Gradient," *AIAA Journal*, Vol. 30, No. 11, Nov. 1992, pp. 2647-2652.
- Frossling, N., "Evaporation, Heat Transfer, and Velocity in Two Dimensional and Rotationally Symmetric Laminar Boundary Layer Flow," *NACA TM 1432*, 1958.
- Gad-el-Hak, M., "Separation Control for Steady and Unsteady Flows," *Proc. Int. Symp. on Non-Steady Fluid Dynamics*, eds. J. A. Miller and D. P. Telionis, FED-Vol. 92, ASME, New York, 1990a, pp. 261-275.
- Gad-el-Hak, M. and Bushnell, D., "Status and Outlook of Flow Separation Control," AIAA-91-0037, 29<sup>th</sup> Aerospace Sciences Meeting, Reno, NV, Jan. 7-10, 1991.
- Gharib, M. and Williams-Stuber, K., "Experiments on the Forced Wake of an Airfoil," *J. Fluid Mechanics*, Vol. 208, 1989, pp. 225-255.
- Henczel, A., Krems, A. F., and Maurer, F., "Development and Application of Infrared and Other Flow Visualization Techniques in a Hypersonic Wind Tunnel of DLR Conference, Southampton, United Kingdom, Sept. 14-17, 1992.
- Hippeneister, S. A. and Russell, L. M., "High-Resolution Liquid Crystal Heat-Transfer Measurements on the End Wall of a Turbine Using a Composite of a Heater Element and Liquid Crystals," *NASA TM 100827*, 1988.
- Hippeneister, S. A., Russell, L. M., and Torres, F. J., "Local Heat-Transfer Measurements on a Large Scale-Model Turbine Blade Using a Composite of a Heater Element and Liquid Crystals," *NASA TM 86900*, 1985.
- Hippeneister, S. A., Russell, L. M., and Torres, F. J., "Use of a Liquid-Crystal Heater-Element Composite for Quantitative, High-Resolution Heat Transfer Coefficients on a Turbine Airfoil, Including Turbulence and Surface Roughness Effects," *NASA TM 87355*, May 1987.
- Ho, Chih-Ming, and Huang, Lem-Saiing, "Subharmonics and Vortex Mixing in Mixing Layers," *J. Fluid Mechanics*, Vol. 119, 1982, pp. 443-473.

- Houghton, E. L., and Carpenter, P. W., *Aerodynamics for Engineering Students*, 4<sup>th</sup> edition, Halsted Press, New York, 1993.
- Hsiao, Fei-Bin, Liu, Chin-Fung, and Shyu, Jongg-Yaw, "Control of Wall-Separated Flow by Internal Acoustic Excitation," *AIAA Journal*, Vol. 28, No. 8, 1989, pp. 1440-1446.
- Hsiao, Fei-Bin, Shyu, Rong-Nan, and Chang, R. C., "High Angle-of-Attack Airfoil Performance Improvement by Internal Acoustic Excitation," *AIAA Journal*, Vol. 32, No. 3, Mar. 1994.
- Huang, L. S., Bryant, T. D., and Maestrello, L., "The Effect of Acoustic Forcing on Trailing Edge Separation and Near Wake Development of an Airfoil," *AIAA Paper 88-3531*, Jul. 1988.
- Huang, L. S., Maestrello, L., and Bryant, T. D., "Separation Control over an Airfoil at High Angles of Attack by Sound Emission from the Surface," *AIAA Paper No. 87-1261*, 1987.
- Hussain, A. K. M. F., "Large-Scale Organized Motions in Jets and Shear Layers," *Recent Advances in Aerodynamics*, ed. Korthapalli Smith, Proceedings of an International Symposium held at Stanford University, Aug. 22-26, 1983, pp. 205-262.
- Incropera, F. P., and DeWitt, D. P., *Fundamentals of Heat & Mass Transfer*, 3<sup>rd</sup> edition, John Wiley & Sons, New York, 1990.
- Jelland, P. T., and Jones, T. V., "The Measurement of Local Heat Transfer Coefficients in Blade Cooling Geometries," *AGARD Heat Transfer and Cooling in Gas Turbines*, 8<sup>th</sup> Vol. 20, 1987.
- Jelland, P. T., and Jones, T. V., "Employing Encapsulated Thermochromic Liquid Crystals," *J. Phys. E: Sci. Instrm.*, 1988.
- Jones, T. V., and Hppensteile, S. A., "High-Resolution Heat-Transfer-Coefficient Maps Applicable to Compound-Curve Surfaces Using Liquid Crystals in a Transient Wind Tunnel," *NASA TM 89855*, Aug. 1988.
- Joslin, R. D., Niclaides, R. A., Erlebacher, G., Hussaini, M. Y., Gutzburger, M. D., "Active Control of Boundary-Layer Instabilities: Use of Sensors and Spectral Controller," *AIAA Journal*, Vol. 33, No. 8, 1995, pp. 1521-1522.

- Jorgenson, L., Swooba, M., and Nitsche, W., "Application of Piezo-Foil Sensors as a Means of Sensing Wall Pressure Fluctuations in Wind Tunnel Tests," *Wind Tunnels and Wind Tunnel Test Techniques; Proceedings of the Conference*, Southampton, United Kingdom, Sept. 14-17, 1992.
- Katz, Y., Nishhi, B., and Wygnanski, I., "The Delay of Turbulent Boundary Layer Separation by Oscillatory Active Control," *AIAA Paper 89-0975*, 1989.
- Kawai, H., "The Piezoelectricity of Polyvinylidene Fluoride," *Japan J. Applied Physics*, Vol. 8, 1968, pp. 975-976.
- Kim, J., Kline, S. J., and Johnson, J. P., "Investigation of a Reactaching Turbulent Shear Layer Over a Backward-Facing Step," *ASME J. Fluids Engineering*, Vol. 102, 1980, pp. 302-308.
- Kim, J., Kline, S. J., and Johnson, J. P., "Investigation of a Reactaching Turbulent Shear Layer," *Flow Over a Backward-Facing Step*, *ASME J. Fluids Engineering*, Vol. 102, 1980, pp. 302-308.
- Kim, K., *A New Hue-Capturing Technique for the Quantitative Interpretation of Liquid Crystall Images Used in Convective Heat Transfer Studies*, Ph.D. Thesis, The Pennsylvania State University, Department of Aerospace Engineering, 1991.
- Kline, S. J., and McClimonck, F. A., "Describing Uncertainties in Single Sample Experiments," *ASME Mechanical Engineering*, Vol. 75, 1953, pp. 3-8.
- Kobayakawa, M., Kondo, Y., and Suzuki, H., "Airfoil Flow Control at High Angle of Attack by Surface Oscillation," *IUTAM Symposium*, eds. R. Kawamura and Y. Aihara, Tokyo, Japan, 1992.
- Korakan, K. D., Griffiths, R. C., and Uellebenberg, S. A., "Verification of the SM701 Airfoil Aerodynamic Characteristics Utilizing Theoretical Techniques," *NAGI-1260-FDP*, Presented at the XXII OSTIV Congress, Uvalde, TX, Jul. 1991.
- Latoru, M., and Murphy, P. V., "Application of PVDF Transducers as Piezoelectric Vibrators for Marine Fouling Prevention," *Ferroelectrics*, Vol. 32, 1981, pp. 33-37.
- Liepmann, H. W., Brown, G. L., and Nosencubek, D. M., "Control of Laminar-Instability Waves Using a New Technique," *J. Fluid Mechanics*, Vol. 118, 1982, pp. 187-200.
- Limvill, J. G., "PVF<sub>2</sub> Models, Measurements and Devices," *Ferroelectrics*, Vol. 28, 1980, pp. 291-296.

- Lomas, C. G. *Fundamentals of Hot Wire Anemometry*. Cambridge University Press, New York, 1986.
- Malikel, E. and Mayle, R. E. "Transition in a Separation Bubble." *J. Turbomachinery*, Vol. 118, Oct. 1996, pp. 752-759.
- Martin, C. J. "The Non-Intrusive Measurement of Wall Shear Stress and Velocity Profiles in Vertical Annular Two Phase Flow." *AICHE Symposium Series Heat Transfer*, Niagara Falls, 1984.
- Mauldin, M. Determination of the Thermophysical Triple Product of Heat Transfer Models Coated with Chiral Nematic Liquid Crystals. Master's Thesis, The Pennsylvania State University, Department of Aerospace Engineering, 1996.
- McCrosskey, W. J. and Dubrin, E. J. "Flow Angle and Shear Stress Measurements Using Heated Films and Wires." *J. Basic Engineering*, Mar. 1972, pp. 46-52.
- Meer, D. J., Watson, T. W., Hartson, S. B., and Jones, T. V. "A Comparison of Liquid Sciences Meeting, Reno, NV, Jan. 7-10, 1991.
- Modest, Michael F. *Radiative Heat Transfer*. McGraw-Hill Series in Mechanical Engineering, New York, 1993, p. 773.
- Muirhead, V. U. and Saltzman, E. G. "Reduction of Aerodynamic Drag and Fuel Consumption for Tractor-Trailer Vehicles." *J. Energy* 3, 1979, pp. 279-284.
- Myer, Eric C. *An Investigation of the Sensitivity of a McCroskey Type Thin Film Shear Stress Gauge to Flow Direction Behavior*. Bachelor's Thesis, The Pennsylvania State University, Department of Aerospace Engineering, May 1988.
- Narayanan, M. A. Badri, Raghu, S., and Poddar, K. "Wall Shear Fluctuations in a Turbulent Boundary Layer." *AIAA Journal*, Vol. 22, No. 9, 1984, pp. 1336-1337.
- Neumann, R. D. and Hayes, J. R. "Introduction to Aerodynamic Heating Analysis of Supersonic Missiles." *AIAA Progress in Astronautics and Aeronautics*, *Tactical Missile Aerodynamics*, eds. M. J. Hemsch and J. N. Nielsen, Vol. 104, 1986.

- Nitsche, W., Mironow, P., Szoedruch, J., "Piezo-electric Foils as a Means of Sensing Unsteady Surface Forces," *Experiments in Fluids*, Vol. 7, No. 2, 1989, pp. 111-118.
- den Oudenh, C., and Hoogendoorn, C., J., "Local Convective-Heat-Transfer Coefficients for Jets Impinging on a Plate; Experiments Using a Liquid-Crystal Technique," *Proceedings of the Fifth International Heat Transfer Conference*, Vol. V, AIChE, New York, 1974, pp. 293-297.
- Parekh, D. E., Kibens, V., Gilezer, A., Witse, J. M., and Smith, D. M., "Innovative Jet Flow Control: Mixing Enhancement Experiments," AIAA-96-0308, 34<sup>th</sup> Aerospace Sciences Meeting, Reno, NV, Jan. 15-18, 1996.
- Parsley, Dr. M., "The Use of Thermochromic Liquid Crystals in Research Applications," *Symposium*, 1991, pp. 53-58.
- Patankar, S. V., and Spalding, D. B., *Heat and Mass Transfer in Boundary Layers*, 1<sup>st</sup> ed., Morgan-Grampian, London, 1967.
- Pearman, G. T., Hokanson, J. L., and Meeker, T. R., "Design and Evaluation of a Contactless Piezoelectric Keyboard Using Polyvinylidene Fluoride as the Active Element," *Ferroelectrics*, Vol. 28, 1980, pp. 311-314.
- NACA 0012 Airfoil in Flight and in the NASA Lewis Icing Research Tunnel," AIAA-90-0199, 28<sup>th</sup> Aerospace Sciences Meeting, Reno, NV, Jan. 8-11, 1990.
- Pomastre, P. E., and Van Fossen, G. J., "Convective Heat Transfer Measurements from a Heated Thin-Film Sensors," *J. Turbomachinery*, Vol. 109, Apr. 1987, pp. 303-309.
- Pucher, P., and Golhi, R., "Experimental Investigation of Boundary Layer Separation With Heated Thin-Film Sensors," *J. Turbomachinery*, Vol. 109, Apr. 1987, pp. 303-309.
- Rice, E. J., and Abbott, J. M., "Control of Flow Separation and Mixing by Aerodynamic Excitation," ICAS-90-5.3.3, *ICAS Proceedings*, 17<sup>th</sup>, Stockholm, Sweden, Sept. 9-14, 1990.
- Nicks, O., Steen, G., Hettmer, M., and Bauer, D., "Wide Tunnel Investigation and Analysis of the SMT01 Airfoil," NAG1-1260-FDP, Presented at the XXXI OSTIV Congress, Uvalde, TX, Jul. 1991.
- Nishioka, M., Asai, M., and Yoshida, S., "Control of Flow Separation by Acoustic Excitation," *AIAA Journal*, Vol. 28, No. 11, Nov. 1990, pp. 1909-1915.
- Pearman, G. T., Hokanson, J. L., and Meeker, T. R., "Design and Evaluation of a Contactless Piezoelectric Keyboard Using Polyvinylidene Fluoride as the Active Element," *Ferroelectrics*, Vol. 28, 1980, pp. 311-314.
- Patankar, S. V., and Spalding, D. B., *Heat and Mass Transfer in Boundary Layers*, 1<sup>st</sup> ed., Morgan-Grampian, London, 1967.
- Pearman, G. T., Hokanson, J. L., and Meeker, T. R., "Design and Evaluation of a Contactless Piezoelectric Keyboard Using Polyvinylidene Fluoride as the Active Element," *Ferroelectrics*, Vol. 28, 1980, pp. 311-314.
- Pomastre, P. E., and Van Fossen, G. J., "Convective Heat Transfer Measurements from a Heated Thin-Film Sensors," *J. Turbomachinery*, Vol. 109, Apr. 1987, pp. 303-309.
- Pucher, P., and Golhi, R., "Experimental Investigation of Boundary Layer Separation With Heated Thin-Film Sensors," *J. Turbomachinery*, Vol. 109, Apr. 1987, pp. 303-309.
- Press, W. H., Teukolsky, S. A., Vetterling, W. T., and Flannery, B. P., *Numerical Recipes* Press, New York, 1992.
- in FORTAN, *The Art of Scientific Computing*, 2<sup>nd</sup> edition, Cambridge University Press, W. H., Teukolsky, S. A., Vetterling, W. T., and Flannery, B. P., *Numerical Recipes* Press, New York, 1992.

- Rice, E. J., and Zaman, K. B. M. Q., "Control of Shear Flows by Artificial Excitation," NASA TM-100201 and AIAA-87-2722, 11<sup>th</sup> Aeracoustics Conference, Sunnyvale, CA, Oct. 19-21, 1987.
- Rivit, R. B., Johnston, J. P., and Eaton, J. K., "Heat Transfer on a Flat Surface Under a Region of Turbulent Separation," J. Turbomachinery, Vol. 116, Jan. 1994, pp. 57-62.
- Roshko, A., "On Drag and Sheddng Frequency of Two-Dimensional Bluff Bodies," NACA-TN-3169, 1954.
- Schlichting, H., *Boundary-Layer Theory*, 6<sup>th</sup> edition, translated by J. Kestin, McGraw-Hill Book Company, New York, 1968.
- Simonicich, J. C., and Moffat, R. J., "Liquid Crystal Visualization of Surface Heat Transfer and Power," Vol. 106, Jul. 1984, pp. 619-627.
- Somers, D. M., and Maughmer, M. D., "The SMT01 Airfoil: An Airfoil for World Class Sailplanes," Technical Sailing, Vol. XVI, No. 3, 1992, pp. 70-77.
- Toda, M., "Voltage-Induced Large Amplitude Bending Device - PVF<sub>2</sub> Bimorph - Its Properties and Applications," Ferroelectrics, Vol. 32, 1981, pp. 127-133.
- Uzol, Oguz, Personal Communication, Sept. 1997.
- Vennemann, D., and Bittesch, K. A., "The Application of Temperature-Sensitive Crystals to Aerodynamic Investigations," European Space Agency, ESR0-RR-77, translation of DLR-FB-73-121, 1973.
- Wetby, J. R., Wicks, C. E., and Wilson, R. E., *Fundamentals of Momentum, Heat, and Mass Transfer*, Wiley & Sons, New York, 1984.
- White, F. M., *Fluid Mechanics*, 2<sup>nd</sup> edition, McGraw Hill, Inc., New York, 1986.
- White, F. M., *Viscous Fluid Flow*, 2<sup>nd</sup> edition, McGraw Hill, Inc., New York, 1991.
- Whithead, L. A., Graham, D. J., Moore, F. A., Bollerman, B. J., Lake, R., and Dunwoody, A. B., "Investigation of Boundary Layer Flow Separation Control by Airfoil Surface Vibration," Canadian Aeronautics and Space Journal, Vol. 42, n. 4, Dec. 1996, pp. 213-219.

- Wiener, B., G. and Camci, C., "A Technique for the Determination of Local Heat Flux on Steady State Heat Transfer Surfaces with Arbitrarily Specified Boundaries," *J. Heat Transfer*, Vol. 118, No. 4, Nov. 1996, pp. 1-8.
- Wiener, B., G. and Camci, C., "Passage Flow Structure and Its Influence on Endwall Heat Transfer in a 90° Turning Duct," Ph.D. Thesis, The Pennsylvania State University, Department of Aerospace Engineering, Aug. 1994.
- Wiener, B., G., Passage Flow Structure and Its Influence on Endwall Heat Transfer in a 90° Turning Duct, Ph.D. Thesis, The Pennsylvania State University, Department of Aerospace Engineering, Aug. 1994.
- Wiedner, B., G., and Camci, C., "A Technique for the Determination of Local Heat Flux on Steady State Heat Transfer Surfaces with Arbitrarily Specified Boundaries," *J. Heat Transfer*, Vol. 118, No. 4, Nov. 1996, pp. 1-8.
- Wiedner, B., G., and Camci, C., "Passage Flow Structure and Its Influence on Endwall Heat Transfer," *J. Turbomachinery*, Vol. 119, No. 1, Jan. 1997, pp. 39-50.
- Wiman, C. D. and Brownand, F. K., "Vortex Pairing: The Mechanism of Turbulent Mixing-Layer Growth at Moderate Reynolds Number," *J. Fluid Mechanics*, Vol. 63, Part 2, 1974, pp. 237-255.
- Zaman, J. Y. and Bakik, S. J., "Redeveloping Turbulent Boundary Layer in the Backward Facing Step Flow," *ASME J. Fluids Engineering*, Vol. 114, Dec. 1992, pp. 522-529.
- Zaman, K. B. M. Q., Bar-Sever, A., and Mangalam, S. M., "Effect of Acoustic Excitation on the Flow over a Low-Reynolds Number Airfoil," *J. Fluid Mechanics*, Vol. 182, Sept. 1987, pp. 127-148.
- Zaman, K. B. M. Q., and McKinzie, D. J., "A Natural Low Frequency Oscillation in the Wake of an Airfoil Near Stalling Conditions," *NASA TM-100213* and *AIAA-88-*0131, 26<sup>th</sup> Aerospace Sciences Meeting, Reno, NV, Jan. 11-14, 1988.
- Zaman, K. B. M. Q., and McKinzie, D. J., "Control of Laminar Separation Over Airfoils by Acoustic Excitation," *NASA TM-101379* and *AIAA Paper 89-0565*, 27<sup>th</sup> Aerospace Sciences Meeting, Reno, NV, Jan. 9-12, 1989.
- Zhang, X., Stasiak, J., and Collins, M. W., "Novel Applications of Holographic Interferometry and Liquid Crystal Thermography in Low Speed Wind Tunnels," *Wind Tunnels and Wind Tunnel Test Techniques, Proceedings of the Conference*, Southampton, United Kingdom, Sept. 14-17, 1992.

